UNIVERSITÉ DE
SHERBROOKE

Faculté de génie

Département de génie civil

FIBRE OPTIC SENSORS FOR HEALTH MONITORING OF REINFORCED CONCRETE BEAMS STRENGTHENED WITH FRPs

CAPTEURS À FIBRE OPTIQUE POUR LE MONITORAGE DES POUTRES EN BÉTON ARMÉ RÉHABILITÉES AVEC DES MATÉRIAUX COMPOSITES

Thèse de doctorat

spécialité: génie civil

Cătălin GHEORGHIU

Sherbrooke (Québec), CANADA August 2003

ABSTRACT

Many countries around the world have tremendous needs to repair and strengthen their transportation infrastructure. Almost everywhere, traffic loads have reached levels largely exceeding design expectations. Northern countries also experience severe winter conditions that are combined with an extensive use of de-icing salts and accelerate structural deterioration. In Canada, the extent of deterioration has prompted many authorities, including the federal and provincial governments, to investigate the potential use of fibre-reinforced polymer (FRP) products to extend the life of their existing structures. The innovative FRP materials used to strengthened deficient structures can be instrumented with a variety of monitoring systems. The built-in sensors would provide information on the health of the structures, the decrease in performance or imminent failure, thereby optimizing lifetime without compromising safety. Fibre optic sensors (FOS) are serious candidates for the long-term monitoring of both existing and new structures throughout their working life. They are small in size, require low wiring, and are capable of measuring absolute values that are indispensable for long-term monitoring. In addition, they can be complemented by non-destructive evaluation techniques for the structural health monitoring of structures.

Research up to date demonstrated the potential of both FRP and FOS systems in the civil engineering field. The FRP systems used as an external reinforcement proved to be very efficient in increasing the strength of concrete structures. However, few studies focused on the long-term durability of these materials when used as external reinforcement of RC beams. As a result, there is a concern regarding the fatigue resistance of these materials when they are exposed to harsh environmental conditions. Previous studies showed that the FOS systems were successfully integrated in FRP products and tested in various loading conditions. A few studies touch upon the fatigue resistance of FOS, and no study has been reported on their durability when exposed to aggressive environments. It is important to understand the behaviour of FOS when they are submitted to these conditions before implementing them extensively in long-term health monitoring projects.

This extensive experimental project was undertaken in order to assess the durability of FOS systems installed on the FRP used as external reinforcement for reinforced concrete beams. Knowing that the FOS installed on a support structure was submitted to various loading and water exposure conditions, the durability of both the FOS and RC beams strengthened with carbon-fibre-reinforced polymers was assessed. The originality of this study consists in the fact that, to the author's knowledge, it is the only experimental program on the durability of FOS installed on a structural element submitted to various fatigue and post-fatigue loading conditions. In addition, it combines the effects of fatigue loading with water exposure conditions. The maximum strain values as well as the numbers of fatigue cycles to which the FOS were tested are larger than in any other previous study. Moreover, the RC beams strengthened with FRP tested in the same conditions with the FOS, were submitted to environmental fatigue, that is water exposures combined with fatigue loading. Finally, the impact resonance method (IRM), a non-destructive testing technique, was for the first time employed to monitor fatigue damage for this type of specimens.

RÉSUMÉ

Plusieurs pays ont un grand besoin de réparer et renforcer leur infrastructure routière. Presque partout, le traffic a beaucoup dépassé les charges de design initial. Les pays nordiques connaissent des conditions hivernales extrêmes qui sont combinées avec l'utilisation de sels de déglaçage et qui accélère la détérioration de structures. Au Canada, l'état de détérioration force les gouvernements, dont les gouvernements fédéral et provinciaux, à envisager l'utilisation des polymères renforcés de fibres (PRF) pour prolonger la durée de vie des structures existantes. Les matériaux innovateurs PRF utilisés pour la réhabilitation des structures déficientes peuvent être facilement instrumentés avec des systèmes de monitorage. Les détecteurs intégrés pourront fournir des informations à propos de l'état des structures, une baisse en performance ou une défaillance majeure, optimisant ainsi leur durée de vie sans en compromettre la sécurité. Les capteurs à fibre optique (CFO) sont des nouveaux candidats pour le monitorage à long-terme de structures existantes ou de nouvelles structures pendant leur durée de service. Ils sont peu encombrants, nécessitent moins de câblage et sont capables de mesurer des valeurs absolues, un attribut essentiel pour le monitorage à long terme. De plus, ils peuvent être associés à des méthodes d'évaluation non-destructive pour mieux connaître l'état de santé des structures.

La recherche actuelle a démontré le potentiel des PRF et des CFO dans le domaine de génie civil. L'utilisation des PRF comme renforcements externes est devenue une technique très efficace pour augmenter la résistance des structures en béton armé. Toutefois, peu d'études ont porté sur la durabilité à long terme des matériaux composites utilisés pour le renforcement externe des poutres en béton armé. Par conséquent, quelques incertitudes restent quant à leur résistance à la fatigue, combinée avec des conditions extrêmes comme le climat nordique. Les CFO ont été intégrés avec succès dans des PRF et testés sous des conditions de charge différentes. Peu d'études portent sur leur résistance à un chargement cyclique, et aucune étude n'a encore été publiée sur leur durabilité à l'exposition environnementale. Il est important de comprendre leur comportement dans ces conditions avant de les intégrés à large échelle dans des projets de monitorage.

Cette étude approfondie à été conçue pour évaluer la durabilité de CFO installés sur des PRF utilisés comme renforcement externe pour des poutres en béton armé. Étant donné que les CFO installés sur l'élément structural ont été soumis conjointement à une variété de conditions de chargement et d'expositions à l'eau, la durabilité de ces deux systèmes a été étudiée en parallèle. L'originalité de cette étude vient du fait que c'est le premier programme expérimental sur la durabilité de CFO installés sur un élément en béton soumis à des conditions de fatigue, suivie par des essais quasi-statiques. De plus, il combine les effets de la fatigue avec l'immersion dans l'eau. Les CFO ont été testés à une déformation et un nombre de cycle supérieurs à toutes les études précédentes. Des poutres en béton renforcées par PRF soumises aux mêmes conditions que les CFO ont été pour la première fois testées avec une combinaison fatigue-immersion dans l'eau. Finalement, la technique de résonance par impact a été utilisée pour la première fois pour le monitorage de telles poutres soumises a des chargements cycliques.

ACKNOWLEDGEMENTS

I would like to sincerely thank my research advisor Professor Pierre Labossière, for his experienced guidance, support, patience and continuous encouragement during the course of this study. I also thank Professor Jean Proulx, my co-advisor, for his insightful comments and discerning review, as well as for his advice, suggestions and help.

I thank Professor Kenneth W. Neale for his friendly support. I also thank Professor Jamal Rhazi for his availability and the willingness to share the equipment for the impact resonance tests.

I would also like to thank several researchers and technicians who helped me during my doctorate. A special thanks to Dr. Laurent Bizindavyi, a Ph.D. graduate from the Université de Sherbrooke, for his warm and friendly support and encouragement. Thanks to Dr. Pierre Rochette and Mr. Marc Demers for the fruitful discussions and friendliness. Thanks for the laboratory assistance of Mr. Marc Demers and Mr. Claude Aubé. Finally, thanks to all members of the ISIS-Sherbrooke group and Civil Engineering Department for their friendship, various help and support.

The financing of this project was provided by the Natural Sciences and Engineering Research Council of Canada (NSERC) and the Network of Centres of Excellence ISIS Canada, and is gratefully acknowledged. The financial support of the Université de Sherbrooke through an exemption of tuition fees for international students and an institutional scholarship is acknowledged.

Finally, I would like to express my eternal gratitude to my wife, parents and family for everything.

TABLE OF CONTENTS

LIST OF FIGURES

LIST OF TABLES

1 INTRODUCTION

1. INTRODUCTION

The overall deterioration of civil infrastructure due to ageing and increasing traffic loads, combined with the increasing cost of maintenance and repair, has resulted in the urgent need for improved techniques for repairing and monitoring existing structures. For new structures, a revolution is being prepared through the integrated development of intelligence and smartness. The smart structure concept advances hand in hand with the progress in material science, sensor/actuator technology, communication and information technology. Important steps were made in the integration of fibre optic sensors in the composite materials used to strengthen the existing infrastructure for continuous monitoring of their structural health and safety. The use of an integrated sensing system in conjunction with non-destructive evaluation could reveal the performance of various structural components during construction, in-service and under exceptional loading conditions, possibly leading to design optimization, improved quality control, and eventually mitigating disasters. There is a huge potential for the use of innovative materials and intelligent sensing for smart structure applications. However, their large-scale implementation is often impeded by the lack of data on the durability of sensors and composite materials submitted to harsh environments and loading conditions. These uncertainties force engineers to overdesign structures, in this way reducing or even eradicating the cost-efficiency of using these innovative materials. By continuous monitoring, the design of the structures could be optimized to make a more efficient use of the innovative materials.

1.1 Research issues

In many industrialized countries most of the transportation infrastructure was constructed in the middle of the twentieth century and is approaching the end of its expected life. In addition, there were significant increases in load requirements over that period. Consequently, there is an urgent need for monitoring and non-destructive evaluation techniques, and durable strengthening methods. A strengthening technique now gaining popularity is the bonding of fibre-reinforced polymer (FRP) sheets or laminates on structural elements such as reinforced concrete beams and columns. This reinforcement can take the shape of confinement for columns, and external plating for beams, and can easily integrate monitoring devices such as fibre optic sensors. Among the non-destructive evaluation techniques, vibration-based and impact resonance methods are most promising for civil infrastructures. The ultimate goal of evaluation and monitoring techniques is the development of intelligent or smart structures. Both existing and new structures would greatly benefit from *in situ* structural monitors that could detect a decrease in performance or imminent failure, thereby optimizing lifetime without compromising safety. Fibre optic sensors are a promising candidate in the field of long-term monitoring as they surpass in many ways the conventional monitoring instrumentation.

In order to get wide acceptance in the engineering field, the innovative materials and sensing systems should prove their durability when exposed to extreme environmental and loading conditions. Durability studies up to date showed that FRPs are either immune or can be protected against many aggressive factors such as ultra-violet radiation, water, snow, wind, and electromagnetic interference. Their mechanical resistance was also successfully tested for creep, fatigue and other loading conditions. However, very few studies combined the environmental conditions with the mechanical loading. In addition, the behaviour of these materials may be quite different when they are used as external reinforcement for concrete members. Moreover, the sensing system integrated with the FRP external reinforcement makes the evaluation task more complicated.

1.2 Objectives

The main objective of this thesis is to test the durability of a fibre optic system installed on FRP products used to strengthened reinforced concrete beams. On the one side, the fibre optic sensors that are to be used for the monitoring of civil structures must be capable of giving absolute reliable readings, should not be affected by aggressive environments and exposure conditions, and have a life as long as that of the structure. On the other side, the FRP systems used as external reinforcement for concrete structure must increase the static and fatigue resistance of the structure, and perform satisfactorily when exposed to water and other environmental conditions.

The selection of the systems to be tested was done in accordance with the criteria stated above and their availability on the Canadian market. The fibre optic sensor chosen for this investigation is the Fabry-Perot strain sensor purchased from Roctest. As for the FRP materials, they were the Replark system produced by Mitsubishi and the CarboDur system from Sika. Both systems are polymers reinforced with carbon fibres (CFRP).

The laboratory tests on Fabry-Perot sensors should:

- verify their working strain range under both fatigue and post-fatigue quasi-static loads;
- check their reliability when exposed to ordinary or saltwater immersions;
- validate the procedure used to install them on the two FRP systems.

The experiments on the CarboDur and Replark systems used as external reinforcement for concrete beams should:

- test the fatigue resistance with or without prior water exposures;
- evaluate the influence of the fatigue loading and water exposure conditions on their strength;
- study the interface between the CFRP-concrete.

1.3 Structure of the thesis

The thesis is divided in three parts. The first part, which includes chapter 2, consists of the literature review. The final goal of structural engineer is the so-called smart or intelligent structure. Section 2.1 gives a definition of the smart structure, its concept and its application to transportation infrastructure. The main components of a smart structure such as sensors, actuators and control processors are discussed in detail. The actively controlled skyscrapers are one of the first large-scale civil engineering applications of the smart structure concept. Important steps are being made towards the development of a smart infrastructure. They consist of continuous monitoring projects and non-destructive evaluation techniques applied to civil structures. Since monitoring is based on sensors, section 2.2 presents fibre optic sensor monitoring projects for both new and rehabilitated structures. Section 2.3 is dedicated to presenting the types of fibre optic sensors (FOS) used in civil structures. The emphasis was placed on the specific FOS used in this study and its application for structural health monitoring. Section 2.4 presents the structural behaviour of the support element used in this study for the FOS monitoring. Finally, two non-destructive evaluation techniques are presented in section 2.5: the vibration-based and impact resonance methods.

The second part of the thesis is a presentation of the extensive experimental program carried out during this doctorate. The research work performed to date on the monitoring of FRP-strengthened structures with FOS showed that there is a lack of data on the durability of the systems under cyclic loading and water exposure conditions. A combination of the exposure and loading conditions is investigated by testing two series of beams instrumented with both conventional and FOS gauges. In section 3.2, the water exposure conditions for the first series of beams are presented. The second series of beams is presented in section 3.3. With these beams, the project investigates the influence of loading history on the ultimate capacity of the specimens, as well as on the FOS system. Different loading ranges and numbers of cycles are selected for the fatigue loading applied to specimens prior to the failure test. In addition, the second series of beams was also investigated with the impact resonance method, a non-destructive vibration technique. This method was used to find the change in vibration characteristics of the beams due to cycling loading. Similar to the FOS monitoring, this technique gives important information on the structural health of a structure.

Finally, chapters 4, 5 and 6, which form the third part of the thesis, present the results obtained during this project. Chapter 4 presents the fatigue and post-fatigue behaviour of the strengthened beams. An emphasis was placed on the behaviour of the CFRP-concrete interface, as this has a crucial role in the load carrying mechanisms. Chapter 5 investigates the reliability of the FOS systems submitted to the same water exposure and loading conditions as for the strengthened beams. Since one FOS was installed before and another FOS after the water exposures, their durability under these conditions was assessed. The FOS system was further tried to an increasing number of cycles with different load amplitudes. Chapter 6 presents the impact resonance test results. This method gave information on natural frequencies and modal damping ratios of the specimens. The impact resonance technique in conjunction with the FOS monitoring were expected to characterize the state of structural health of the concrete beams. Results and recommendations are summarized in the concluding chapter of this thesis.

2 HEALTH MONITORING

2. HEALTH MONITORING AND NON-DESTRUCTIVE EVALUATION FOR SMART AND DURABLE RC STRUCTURES

In many industrialized countries, such as Canada and the USA, most of the transportation infrastructure was constructed in the middle of the twentieth century and is approaching the end of its expected life. In addition, there were significant increases in load requirements over that period. For the existing bridges, dams, tunnels and landmark structures, there is an urgent need for non-destructive evaluation techniques (NDE) and fast, efficient and durable strengthening methods. Among the available NDE techniques, vibration-based and impact resonance methods are most promising for civil infrastructures (Doebling et al. 1998; Sansalone, 1997). A strengthening technique now gaining popularity is the bonding of fibre-reinforced polymers (FRP) sheets or laminates on structural elements such as reinforced concrete beams and columns. This reinforcement can take the shape of confinement for columns, and external plating for beams (Bakis et al. 2002) and can easily integrate monitoring devices such as fibre optic sensors (Labossière et al. 2000). The ultimate goal of NDE and monitoring techniques is the development of intelligent or smart structures (Spillman et al. 1996). Both existing and new structures would greatly benefit from *in situ* structural monitors, which could detect a decrease in performance or imminent failure, thereby optimizing lifetime without compromising safety. An integrated sensing system could monitor the various structural components during construction, possibly leading to improved quality control. It could also provide valuable information on the serviceability of a structure (ISIS Canada, 2001a). Fibre optic sensors are a promising candidate in the field of long-term monitoring as they surpass in many ways the conventional monitoring instrumentation.

Section 2.1 proposes a definition of a smart structure, its concept and its application to civil infrastructure. The main components of a smart structure such as sensors, actuators and control processors are then presented. The first steps towards a smart infrastructure are being made. They consist of monitoring and NDE techniques of structures. Section 2.2 presents fibre optic sensor monitoring projects for both new and rehabilitated structures. Section 2.3 is dedicated to presenting the types of fibre optic sensors (FOS) used in civil structures. The emphasis was placed on the specific FOS used in this study and its application for structural

health monitoring. Section 2.4 presents the structural behaviour of the support element used in this study for the FOS monitoring. Finally, two NDE techniques are presented in section 2.5: the vibration-based and impact resonance methods. The latter was used in the present program as a complementary method for damage detection.

2.1 Smart structures

The overall deterioration of the civil infrastructure due to ageing and increasing traffic loads, combined with the increasing cost of maintenance and repair, has resulted in the need for improved techniques for monitoring existing structures. For new structures, a revolution is being prepared through the integrated development of intelligence or smartness. This concept advances hand in hand with advances in sensor/actuator technology, and communication and information technology. This section presents the progress in the smart structures field focusing on its possible application to transportation infrastructure. In 2.1.1 a formal definition of a smart structure is presented with details about each of its components. This concept is then presented in more detail in 2.1.2, together with its application to civil engineering.

2.1.1 Definitions

There has been a considerable discussion in the technical community on a number of questions concerned with smart materials and structures, such as what they are, whether smart materials can be considered a subset of smart structures, whether a smart structure and an intelligent structure are the same thing, and so on. This discussion is both fuelled and confused by the technical community due to the truly multidisciplinary nature of this new field.

Spillman et al. (1996) conducted a survey in order to ascertain whether a consensus is emerging on a number of questions related to the definition of smart materials and structures. Based on the results of their survey, the following formal definition for smart materials and structures is proposed.

"A smart structure is a non-biological physical structure having the following attributes:

(i) a definite purpose;

(ii) means and imperative to achieve that purpose;

(iii) a biological pattern of functioning."

The first attribute of the definition is fulfilled by all systems made by humans, because any system will have a specific design objective, or the so-called definite purpose. Smart materials and structures must have the means to fulfil their purpose, or the designer failed in meeting the design objectives. The last attribute of a smart structure is the biological pattern of functioning to provide the ability to adapt, which is essential for any material or structure in order to be considered a smart one. Spillman et al. (1996) included an imperative to achieve this purpose to reflect either an instinctual or conscious mental activity that supports achieving the purpose by whatever means are available.

Smart materials are considered to be smart structures at microscopic or mesoscopic scales. Thus they are assumed to be a subset of smart structures. These include materials such as shape memory alloys (SMA). At the macroscopic level, one finds structural members such as beams, columns and plates and eventually structural systems and they are of great interest for civil engineers.

Aktan et al. (1998) applied the above principle to infrastructure and suggested that an intelligent infrastructure is expected to: (a) sense its loading environment, as well as its own response and any ongoing deterioration and damage; (b) reason by assessing its condition, health, capacity and performance; (c) communicate through proper interfaces with other components and systems; learn from experience; (e) decide and take action for disaster mitigation; e.g., alerting officials, diverting users, structural control, self-repair, etc. Thus intelligent infrastructure consists of an integrated package that incorporates the physical infrastructure system, a monitoring system consisting of sensors, data acquisition, control and communication hardware and software to implement the above functions.

2.1.2 Concept of a smart structure

Several researchers advanced different approaches regarding the possible concept of a smart structure. Measures (1996) considers that smart structures are at the confluence of three disciplines: materials and structures, sensing systems, and actuator control systems. This

conceptual view of a smart structure is shared by subsequent studies, such as those presented by Udd (1995), and Galea (2001).

In terms of the three attributes of a smart structure, as mentioned in 2.1.1, the structural system will act in such a way as to mimic the functioning of biological or living material (Darwish and Darwish, 2002). Thus, smart structures would posses their own sensors, control processors, and actuators. Chong (1998) made an analogy with the human body and compared the sensor to the nervous system, the control processor with the brain, and the actuator with the human muscular system.

Figure 2.1 shows a schematic concept of a smart structure consisting of four basic components, represented by blocks, and flow of data between components by means of arrows. The structure is represented in the middle of the scheme by the cylindrical block. It can be seen that it is connected by an arrow to the sensor block presented in the left part of the figure. Structural data is measured by means of sensors attached to the structure and is transmitted to the control unit. The control unit, that is the computer processor, commands the functioning of the actuator that imposes a certain load, as necessary, to the structure. The actuator and sensor blocks are interconnected because in some cases these two may be incorporated in the same system, as explained below.

The conventional sensors include strain gauges, vibrating wires, accelerometers, and piezoelectric materials. A new promising sensor is the optical-fibre sensor recently introduced in monitoring mainly deformations in civil engineering structures (Tennyson et al. 2000). These fibre optic sensors are the subject of the present experimental program and are discussed in detail further in the chapter.

Some sensors can also act as actuators. They are referred to as piezoelectric ceramics and are based on the piezoelectricity phenomenon, which is the generation of an electric charge in a material when it is subjected to a mechanical stress (this is called the direct effect). Conversely, piezoelectric ceramics generate a mechanical strain in response to an applied electric field (this is called the reverse effect). Another actuator is the shape-memory alloy

(SMA). A SMA is a material that, when plastically deformed at low temperature, will regain its original shape when heated. There are many other well-established actuators such as electrostrictive and polyvinylidene fluoride ones. One of the challenges is to model the micro-scale behaviour of these materials to the macro-scale behaviour of structural systems such as civil structures (Chong, 1998). This is the reason why hydraulic actuator systems continue to be most popular in the field of civil engineering.

One of the existing applications that is closest to the smart structure concept is the seismic isolation and control of civil structures. The seismic isolation is a structural control method used to restrain the displacements and accelerations on a structure due to earthquake and wind excitations. It can be divided into active and passive control, depending on whether or not it requires external input energy to suppress or control the response of the structure. The active control of structures is performed usually by actuators that require an input of energy. For instance, in the case of piezoelectric actuators, the energy is provided in the form of electricity, whereas for the shape memory alloys, it is in the form of heat. The passive systems have no need of any energy input and they include: isolators, such as rubber and slide bearings, and hysteretic- or velocity-type dampers. The hysteretic-type dampers include steel, lead and friction dampers whereas the velocity-type comprise oil, tune liquid (TLD), tune mass (TMD) and viscous dampers (Kitagawa and Midorikawa, 1998). In Japan alone, by the end of 1996, a total number of 287 seismic isolated buildings are reported (Kitagawa and Midorikawa, 1998).

The only civil smart structures conforming to the specified conditions above can be found in the case of active-controlled skyscrapers. There are few such application, and they are especially located in the USA (Reinhorn et al. 1998; Kwok and Samali, 1995) and in Japan (Kitamura et al. 1995). The Citicorp Building in New York is a skyscraper that is actively controlled by a TMD. The main components of the smart structure in this case are as follows. The sensor is represented by accelerometers; the actuators used here are the hydraulic actuator and the TMD; and a computer represents the control system. The accelerometer is connected to the computer that gathers information about the ambient accelerations at the top of the structure. Once a given threshold is reached, the computer activates the actuators and the

TMD to counteract the wind or seismic action. This active control system resonates out of phase with the building in two orthogonal directions and can reduce the sway motion by up to 40% (Petersen, 1980). Another example of such an active control of structures is the Hancock Tower in Boston (Campbell, 1995).

If the practical application of the smart structure concept for transportation infrastructure is delayed by various practical, technology and economic constraints, the imagination has no barriers. Figure 2.2 shows the futuristic look of a smart road instrumentation, and a schematic view of a smart bridge is shown in Figure 2.3. It can be seen that sensors are either attached or embedded to internal as well as to external reinforcement for both the bridge deck and the piers. The actuators are also placed at key points along the deck and piers.

Although the practical application of the smart civil engineering structure concept has not been completely achieved, it should be mentioned that important steps are being made in the structural health monitoring of civil structures. The next section focuses on the use of FOS for monitoring new structures or existing structures strengthened with FRP.

2.2 Monitoring of rehabilitated and new structures

The existing transportation infrastructure is submitted to increasing traffic loads and corrosion that accelerate its degradation. In Canada, the extent of deterioration has prompted federal and provincial government agencies to investigate the use of FRP products to extend the life of their existing structures. The large-scale implementation of these products is often impaired by the lack of data on their durability when used as internal and external reinforcement for concrete structures. These strengthened structures would greatly benefit from *in situ* monitoring which could detect the distribution of loads as well as a decrease in performance, thus optimizing the design and lifetime without compromising safety. For new structures, a health monitoring system would help in maintaining the functional and structural reliabilities of a system at each of the utility, serviceability, safety and conditional limit-states. Although FOS have been mainly used in aerospace field, they are recently more and more employed in civil engineering. Fibre optic sensors are serious candidates for the monitoring of structures

throughout their working life. They could determine strain, pressure, displacement, rotation, load distribution, acceleration and temperature. In 2.2.1, some applications of FOS health monitoring of existing structures are presented. FOS monitoring of new structures are then presented in 2.2.2.

2.2.1 FOS monitoring of existing structures

With their small size, immunity to electromagnetic interference, non-corrosive, and no wiring problems, FOS are becoming popular in civil engineering monitoring applications. The present section presents some FOS monitoring applications for existing structures that were or were not strengthened with FRP. Most of the times the innovative FOS systems were used in parallel to conventional instruments.

Two of the first monitoring applications by FOS conducted by the research group ISIS-Sherbrooke were carried out in 1996 on two existing structures rehabilitated with FRP (Rochette et al. 2002). The first project was the rehabilitation of 9 columns of an overpass located on Highway 10 at St-Étienne-de-Bolton, Québec. The second project consisted of the FRP-strengthening of several beams and columns of the Webster parking garage in Sherbrooke. Both projects employed fibre Bragg grating (FBG) sensors and illustrated the difficulties encountered in the integration of fibre optic sensing systems in field conditions. The data acquired during several months, after the structure was brought into service, could not be exploited because of the high instability of the FBG strain indicator unit.

A third project was undertaken in 1998, when the four RC beams of Ste-Émélie-de-l'Énergie bridge were strengthened using FRP. The detailed rehabilitation project and its instrumentation with FOS are reported by Labossière et al. (2000). In order to evaluate the structural efficiency of the FRP strengthening, the bridge was instrumented with conventional devices and two types of FOS sensors: FBG and Fabry-Perot. Following the bridge strengthening, periodic readings with both FOS and conventional gauges are taken on a regular basis. Continuous monitoring was also carried out for periods of up to 14 days. Up to date the FOS and conventional gauges do not indicate any structural degradation since the rehabilitation.

The fourth case involving the ISIS-Sherbrooke group is the FOS monitoring of the Gentilly nuclear reactor secondary containment structure. Four types of FOS strain sensors are used in this rehabilitation project, and are currently being evaluated (Rochette et al. 2002). Other Canadian FOS monitoring projects for FRP-reinforced structures include the Salmon River Bridge in Nova Scotia (Mufti et al. 1998), Joffre Bridge in Québec (Benmokrane et al. 2001), and Taylor Bridge in Manitoba (Tennyson et al. 2001). Most of these projects employed FBG sensors, and sometimes remote monitoring and video camera were used to synchronize the recorded data, as in the case of the Taylor Bridge. The wireless possibility to interrogate and store data is also reported by Pines and Lovell (1998).

FBG were also used for monitoring the structural behaviour of the Mjosundet Bridge in Norway (McKinley et al. 2002). The FBG sensors were successfully used in assessing the performance of the structure under controlled load testing. Historical constructions also take advantage of the FOS monitoring. Inaudi et al. (2001) have applied deformation FOS for crack monitoring of a church vault in Switzerland. They have also used 60 such sensors for the monitoring of a pier in Genoa harbour, Italy.

2.2.2 New structures monitored by FOS

A two-span concrete highway bridge built in 1993 in Calgary is the first Canadian bridge to be instrumented with FOS (Measures et al. 1995). The Beddington Trail Bridge was monitored by means of FBG sensors either embedded in the concrete girders or installed on FRP prestressing tendons. Of the 18 FBG initially installed, 15 survived and in November 1999 they were still functioning correctly (Tennyson et al. 2001).

The Confederation Bridge, spanning 12.9 km from Prince Edward Island to the New Brunswick mainland, was completed in 1997. The bridge was instrumented with FGB sensors located along one span and on one main girder (Mufti et al. 1997). Fifteen FBG sensors are still currently in service (Tennyson et al. 2001).

Practical sea and flight trials of FBG sensors are presented by Read and Foote (2001). FBG strain sensors were embedded in the 35-m carbon fibre mast of a yacht, and also bonded on a turbo-prop driven aircraft. The FBG, exposed to hostile environment, proved robust and reliable during several sailing and flight trials. However, the sensors' sensitivity to temperature remained a subject of further development.

Huston et al. (1994) report several civil engineering monitoring projects in Vermont, USA. They have developed and employed a FOS system to measure vibrations. They first tested the FOS in the laboratory and then, starting with 1993, employed it to some large-scale field applications. These include: a three-story building; one hydroelectric dam; one highway, one railway and one pedestrian bridge. These field applications showed the possibility to use the FOS for ambient vibration monitoring of different structural types. In the case of the hydroelectric dam, the vibration signature recorded by the FOS showed a default of the main gear of the turbo generator. This fault decreased the efficiency of the generator by more than 10%. The gear was replaced and the unit's efficiency met the specified value. The FOS proved to be robust and reliable in this high-electromagnetic interference environment. Fuhr (1995) reported a laboratory study on the reliability of this sensor for vibration. They found a good correlation between the FOS and the conventional accelerometer measurements.

All the field applications of FOS monitoring shown above have demonstrated the potential of the FOS sensors in civil engineering. Some of the very first studies were conducted in the early 1990s and thus provide information on the reliability of these sensors for about a 10-year period. Knowing that the life of some civil structures can reach more than 100 years, there is a concern about the FOS long-term durability under adverse loading and exposure conditions. The next section presents the progress on the durability of fibre optic strain sensors with an emphasis on the Fabry-Perot sensors.

2.3 FOS for strain monitoring

The field applications presented in section 2.2 confirmed the interest that civil engineers have in FOS systems for strain monitoring of structures. The main advantages of strain FOS over conventional electrical strain gauge (ESG) are:

- their small diameter, from 125 to 250 μm, which makes them easily embeddable in different materials;
- their life presumably longer than that of the ESG;
- the absolute measurements that they provide and which are indispensable for long-term monitoring;
- their immunity to electromagnetic interference;
- their low wiring requirements;
- the multiplexing possibility, that is the ability to provide measurements at different points along the same fibre.

A classification of FOS for strain sensing is presented in 2.3.1. A detailed description of the Fabry-Perot strain sensor used in this study follows in 2.3.2. Finally, laboratory and field studies employing Fabry-Perot strain sensors are presented in 2.3.3.

2.3.1 Classification of FOS

There are mainly three ways to classify FOS. First, the fibre optic sensors are classified as intrinsic if the effect of the measurement on light being transmitted takes place in the fibre. The sensor is considered to be extrinsic if the fibre carries the light from the source to the detector, but the modulation occurs outside the fibre.

The second classification divides the FOS into distributed and localized or point sensors. The distributed sensor measures strain on a predetermined distance, sometimes of the order of meters. Two types of such sensors were developed in Canada. One is based on a conventional fibre optic lead and has a gauge length from 0.02 to 100 m (Tennyson et al. 2000). The other type, which also utilizes a conventional fibre optic lead, is based on Brillouin diffusion. This is actually a quasi-distributed sensor since it measures several localized strains on a specified length of the fibre optic lead (DeMerchant et al. 2000). The localized sensor detects strain variation only on a very short distance, that is why they are also called point sensors. Fabry-Perot and Bragg gratings belong to the localized FOS category.

Finally, FOS may be divided into two broad categories, intensiometric and interferometric. The intensiometric sensor is based on the amount of light detected through the fibre. In this category one may find the optical time domain reflectometry and statistical mode sensors (Merzbacher et al. 1996). The most common interferometric sensor is the Mach-Zender two-arm FOS. With this type of device strain can be monitored directly by attaching the signal arm to the structure, while the reference arm of equal length is isolated from the environment (Merzbacher et al. 1996).

2.3.2 Fabry-Perot FOS for strain monitoring

The FOS strain sensor used in this study is an extrinsic Fabry-Perot interferometer produced by Roctest. Figure 2.4 illustrates schematically the Fabry-Perot strain sensor. It can be seen that it consists of two semi-reflective closely-spaced mirrors perpendicular to the fibre axis. These mirrors are placed on the tips of two optical fibres spot-fused into a capillary. The space separating the mirrors is called the Fabry-Perot cavity length, and the distance between the fuse spots is called the gauge length. These two parameters dictate the gauge operating range and sensitivity (Choquet et al. 2000). This interferometer system measures the lag between the light reflected by the first mirror, which is also the reference mirror, and the light reflected by second the mirror. Thus a change in the cavity length produces a different lag, which is related to the actual strain experienced by the material onto which the sensor is bonded.

The main advantages of Fabry-Perot sensor are (Rochette, 2001):

- accuracy;
- ideal for integration into composites;
- compactness;
- multiplexing possibility;
- no sensitivity to transverse deformation.

Their main disadvantages are:

- poor mechanical resistance: fusing spots are weak points;
- high costs: due to difficult implementation in mass-production.

Although many applications of Bragg gratings are reported in the literature, previous studies have indicated what kind of problems are encountered with their implementation in monitoring projects. One of the main problems is that FBG are sensitive to transverse deformations (Rochette, 2001). Another difficulty encountered with this FO system is the high instability of the reading unit (Rochette et al. 2002). As opposed to FBG, Fabry-Perot sensors can be interrogated with a reliable reading unit produced by Roctest, readily available in Canada. The experimental project reported here proposed to study the durability of Fabry-Perot strain sensors under both fatigue load and water exposure conditions.

2.3.3 Applications of Fabry-Perot strain sensors

The progress in the research activities on strain monitoring by means of Fabry-Perot sensors is presented. Some laboratory studies are described first and are followed by field applications of these systems.

Choquet et al. (2000) subjected FOS strain sensors to thermal gradients and showed their insensitivity to thermal variations. Three FOS were placed in an temperature-controlled oven and tested at temperatures ranging from 20 to 80°C. For this range of temperatures, they found the strain sensors to be almost insensitive to temperature variations. Another study reports results on FOS installed on a titanium bar submitted to temperature of 350 and 500°F (Richards et al. 2001). They tested statically the sensor bonded on the specimen up to strains of about 1100 με. For the two temperature levels the FOS revealed a 1% and 4% reduction in accuracy at 350°F and 500°F, respectively.

Static tests of Fabry-Perot sensors installed on steel rebars used as reinforcement for a concrete specimen are reported by de Vries et al. (1995). They show that the sensors measured precisely strains of up to 2000 με. The static experimental results on a FOS embedded into a composite patch are presented by Richards et al. (2001). They show that the sensors provide reliable strain data up to 10 000 με under static loading conditions. Rochette (2001) reports another static test on a FOS installed on a steel beam clamped at one end and loaded in bending. For static strains of about ±1000 με, the FOS readings are 10% larger than those measured by the conventional gauge.

Akhavan et al. (1998) report a laboratory study of FOS bonded on carbon FRP (CFRP) plates. The transient low-velocity impact strains measured by FOS are compared to those obtained by conventional strain gauges and piezoelectric sensors. They conclude that the FOS give reliable results, but the precision of the measurements depend on the orientation and the gauge length of the FOS.

These sensors, as could be seen above, were tested as units (Choquet et al. 2000), or bonded on different materials (Richards et al. 2001; Rochette, 2001). Efforts were also made to integrate the Fabry-Perot sensors into different materials. Kalamkarov et al. (2000) report a case where the FOS were successfully embedded in a FRP bar during the pultrusion process. The embedded FOS showed very good agreement with the conventional gauges when submitted to static strains of up to 3500 με and to temperature extremes of –40 and +60°C. The short- and long-term creep behaviour of the FOS embedded in the so-called smart rod was excellent. The authors also performed fatigue tests on the FOS instrumented rods. They showed that the FOS measured strain precisely for 140 000 cycles with maximum strains of about 1400 με.

Very few laboratory studies report on the fatigue behaviour of Fabry-Perot strain sensors for monitoring concrete structures. De Vries et al. (1995) employed Fabry-Perot sensors attached to steel rebars to monitor local strain in a concrete specimen. Their study showed that Fabry-Perot FOS can be cycled for 100 000 cycles and still provide reliable strain measurements. Richards et al. (2001) tested sensor attachments techniques in fatigue. They embedded the FOS into a composite coupon and tested it cyclically in tension-tension fatigue. The Fabry-Perot sensor survived up to one million cycles at strains levels below 2800 με. At strain levels above these values, degradation of the fibre optic sensor was observed at the early stages of fatigue loading.

Among the first field monitoring applications by means of Fabry-Perot strain sensors is the pedestrian bridge constructed in 1997 in Sherbrooke (Quirion and Ballivy, 2000). The FOS were successfully embedded in reactive-powder-concrete for the long term monitoring of the

60-m-span bridge. Two other applications of Fabry-Perot sensors are reported by Benmokrane et al. (2001) and Tennyson et al. (2001). In these cases, the strain sensors were embedded in the NEFMAC prefabricated FRP grid used for the reinforcement of the side barriers of the bridges. The two bridges are the Joffre Bridge in Sherbrooke and the Crowchild Trail Bridge in Calgary, and their construction ended in 1997. One rehabilitation project is reported by Labossière et al. (2000). Eight Fabry-Perot sensors were placed on steel rebars and on the FRP systems used for the strengthening the Ste-Émélie-de-l'Énergie bridge. A more recent rehabilitation project where several Fabry-Perot strain sensors were placed on the ring beam of a nuclear reactor containment structure is reported by Rochette et al. (2002).

From the studies presented here, it can be seen that very few experimental projects touch upon the fatigue life of the Fabry-Perot strain sensors. Only one study investigates the fatigue behaviour of the sensor when embedded in a structural element (de Vries et al. 1995). In addition, the durability of Fabry-Perot sensors was not tested in aggressive environments such as water exposures. These facts illustrate the lack of data on the FOS durability under accelerated ageing and cyclic loading conditions. As the FOS would be used for monitoring the entire life of a structure, the system durability is a key factor. The present experimental program was conceived to investigate the fatigue and exposure resistance of Fabry-Perot strain sensor bonded to CFRP used as external reinforcement for RC beams.

2.4 Structural support element: RC beams with external CFRP reinforcement

In laboratory studies Fabry-Perot FOS is generally embedded in or bonded on composite patches (Akhavan et al. 1998), or integrated in FRP bars (Kalamkarov et al. 2000). In field applications, Fabry-Perot was embedded in concrete (Quirion and Ballivy, 2000) or installed on steel rebars and FRP external reinforcement (Labossière et al. 2000). However, few laboratory studies are reported on FOS installed on a structural member such as a strengthened RC beam. In the present experimental program, Fabry-Perot sensors are installed on external FRP reinforcement for RC beams. In order to interpret FOS results, it is important to understand the static and fatigue behaviour of the support element, that is the RC beam strengthened with FRP in bending.

This section presents a review of the studies performed on the strength and durability of RC beams strengthened with FRP. In 2.4.1, investigations on the quasi-static behaviour of these beams are presented. The fatigue behaviour is discussed in 2.4.2, and is followed by a presentation of the durability studies, through accelerated laboratory tests, in 2.4.3.

2.4.1 Quasi-static behaviour

Among the first FRP-strengthened beam studies are those reported by Meier et al. (1992), Saadatmanesh and Ehsani (1991) and Triantafillou and Plevris (1992). They all have investigated the quasi-static behaviour of RC beams externally strengthened with glass FRP (GFRP) or carbon FRP (CFRP). Their common conclusion was that FRP bonded on the tension face of the beams significantly increase the ultimate capacity of the beams. However, they pointed out that the FRP-concrete bond plays a vital role in the efficiency of the strengthening scheme.

Some other researchers confirmed the efficiency of this strengthening technique for increasing the flexural capacity of reinforced concrete beams (Heffernan and Erki, 1996; Shahawy and Beitleman, 1999, Labossière et al. 2000). A review by Bonacci and Maalej (2001) gathers information from 23 separate studies comprising RC beams externally strengthened in flexure with aramid, glass and carbon FRP, having spans between 0.95 m and 7.5 m. One third of the strengthened specimens showed strength increases of 50% or more in combination with a considerable increase in deflection capacity. They have also found that failure by debonding of FRP was prevalent among the 127 specimens. To avoid this, anchorage of the FRP was applied in some studies.

From all these studies, it appears that the behaviour of the FRP-concrete interface governs the quasi-static strength of many RC beams externally strengthened with FRP. The FRP bond length and its strength has been studied by Bizindavyi and Neale (1999) for both carbon and glass FRP. Based on experimental results, they have proposed empirical equations to evaluate the FRP anchorage length and for the bond strength between the FRP and concrete.

2.4.2 Fatigue behaviour

The fatigue life of RC beams strengthened with FRP was always a concern among design engineers. Pioneering studies in this field were reported by Meier et al. (1992); research intensified in recent years with experimental programs comprising both large-scale and small-scale specimens.

An extensive experimental program on the fatigue of RC beams strengthened with CFRP is reported by Heffernan (1997). Beams with spans of 3 m and 5 m have been cycled with load amplitudes from 20% to 60, 70 and 80% of the yielding moment. For the beams with 3-m spans, the fatigue tests were conducted at a frequency of 3 Hz. For the 5-m-long beams, the frequency was decreased to 1.5 Hz, due to the limitations of the equipment. The maximum fatigue life observed of 6 440 000 cycles was obtained for a 3-m-long beam loaded with cycles of amplitudes of 20 to 60% of yielding moment. The fracture of the steel rebar governed the beam failure in fatigue.

Two 6-m-long RC beams strengthened with CFRP were tested in fatigue at EMPA in order to investigate the use of two CFRP adhesives (EMPA, 1999). They loaded the beams for five-million cycles at 4.4 Hz, and then tested them statically to failure. They found the fatigue behaviour of the beams to be very good. The post-fatigue static test showed once more a failure mode by debonding of the CFRP plate, as in 2.4.1. It is worth mentioning that several studies presented here reported also results from post-fatigue quasi-static tests to failure.

Barnes and Mays (1999) reported on the fatigue performance of concrete beams strengthened with CFRP. Five 2.3-m-long specimens were tested in fatigue with load amplitudes of up 48% of the ultimate capacity. All strengthened specimens failed by steel fracture before reaching 2-million cycle, except for one. The specimen cycled with a maximum load of 26% of the ultimate capacity, reached about 12-million cycles and did not fail.

The study by Shahawy and Beitleman (1999), conducted on 5.8-m-long beams, investigated the influence of parameters such as concrete compressive strength, the number of CFRP

layers, and the strengthening scheme, on the fatigue behaviour of the specimens. All specimens were tested at a frequency of 1 Hz with cycles of load ranging 25 to 50% of the ultimate capacity. A specimen wrapped with three layers of CFRP was loaded for 3-million cycles and did not fail. Their results indicate that the fatigue life of RC beams can be extended significantly with an external CFRP reinforcement.

The only study reporting the fatigue behaviour of GFRP-strengthed beams is by Papakonstantinou et al. (2001). Their 1.3-m-long specimens were cycled at 2.3 Hz with load amplitudes from 36 to 85% of the ultimate capacity. They observed that the RC beam extended its fatigue life due to GFRP external reinforcement. The fatigue failure mode is by fracture of the internal steel reinforcement.

A more recent study by Brena et al. (2002) reports fatigue tests conducted on 8 beams either 2.9 or 3.2-m-long. They used two strengthening schemes with different CFRP systems. The repeated load, corresponding to service and overload conditions, was applied for a maximum of one million cycles at a maximum frequency of 2 Hz. The behaviour of the specimens submitted to service load conditions, that is cycles with amplitudes from 33 to 50% of the yielding moment, was very good. In the case of overload conditions, with load amplitudes up to 110% of the yielding moment, failure modes observed as early as 9000 cycles were CFRP debonding and fatigue fracture of the steel reinforcement.

From all these studies on the FRP-strengthened beams, the following conclusions can be drawn. The predominant fatigue failure mode is by fracture of the internal steel reinforcement. This failure mode seems to be independent of the rate of loading since it was reported for beams tested at frequencies ranging from 1 Hz (Barnes and Mays, 1999), to 4.4 Hz (EMPA, 1999). According to Heffernan (1997), the fatigue life of the rebars depends on the surface of the steel reinforcement. He found that ribbed rebars had shorter fatigue lives than smooth-machined bars. It is recommended that the same maximum allowable steel stress used for reinforced concrete beam design, be used in the design of FRP-strengthened beams (Papakonstantinou et al. 2001).

It can be noticed that none of the reported studies focused on the FRP-concrete interface throughout the fatigue tests, but were rather oriented towards understanding the fatigue life and the maximum cyclic load limits. A recent study reports results on the FRP-concrete bond strength during fatigue tests (Bizindavyi and Neale, 2003). However, there is scarce data on this subject which, in many cases, is crucial for the efficient use of FRP-strengthening for extending the service life of structures.

2.4.3 Environmental exposure conditions

Another aspect of concern on the durability of FRP systems for civil structures is the environmental exposure conditions. These systems were applied in a number of field projects starting in the mid-1990s. They provided useful data on the in-service behaviour of FRP-strengthening systems, but only for a fraction of the service life of the structure. In order to simulate the environmental exposure for the whole life of the structure, accelerated ageing tests such as wet-dry and freeze-thaw cycles are conducted in laboratory conditions.

Beaudoin et al. (1998) present a study where 1.2-m-long beams are subjected to wet-dry cycles. Two configurations were used to strengthened the beams in flexure. They consisted of bonding CFRP plates or sheets on the tension face of the beam. For one configuration, external GFRP stirrups were used to anchor the CFRP sheets. Quasi-static test results on the RC beams strengthened with two CFRP systems indicate that the beam strength is not affected by the 26 wet-dry cycles. A continuation of this study is presented by Raîche et al. (1999). In this paper, the ageing program was extended to include also the continuous immersion condition in both ordinary and saltwater. They concluded that the strength of the beams submitted to environmental ageing is influenced by the strength of the GFRP anchorage.

The freeze-thaw effect on the static strength of beams has been investigated by several researchers. Xie et al. (1995) report tests on 30-cm-long concrete prismatic samples with CFRP reinforcement. They concluded that the freeze-thaw cycles reduced the strength of the specimens. Chajes et al. (1994) report static tests on 33-cm-long beams submitted to up to 100 freeze-thaw cycles. Specimens were externally-reinforced with three FRP systems: glass,

carbon and aramid. Their results showed a decrease in strength as a result of freeze-thaw cycles.

Lopez et al. (1999) submitted several 1-m-long beams to up to 300 freeze-thaw cycles. They observed that the moment capacity and ultimate displacement decrease with increasing number of freeze-thaw cycles. Green et al. (2000) also performed quasi-static tests on 1.2-m-long beams exposed to up to 300 freeze-thaw cycles. Their results indicate that freeze-thaw cycling does not reduce the load carrying capacity of the joint between concrete and CFRP plates. Nevertheless, the adhesive may be affected slightly by freeze-thaw exposure, resulting in changes in failure modes.

The only study that presents the effects of environmental exposures combined with fatigue loading was by Lopez et al. (2001). They have tested two beams in fatigue at a temperature of –29°C. The tests were conducted at 3 Hz with cycles of amplitude of 20 to 80% of the failure load and for a maximum number of fatigue cycles up to 155 500. They concluded that the low temperature exposure did not affect the fatigue behaviour of the CFRP-strengthened beam. However, there is a lack of data on the combined effects of fatigue loading with other environmental exposures, such as water immersion, on the strength of strengthened beams. This topic is one objective of the experimental program presented in chapter 3.

2.5 Non-destructive testing

The monitoring systems introduced in section 2.2 could give valuable information about the service-load conditions of the structures. In the case of a highway structure, it could detect the excess load, and even the weight and speed of vehicles. The sensing system can be complemented with a non-destructive testing to fully define the health of the structure. These testing techniques are used for damage detection and evaluation. Among these methods are: vibration-based, impact resonance, liquid penetrant, magnetic field, acoustic, sonic and ultrasonic, eddy current, radiography, infrared, microwave, and holography. Two techniques are discussed in the following: the vibration-based damage detection and the impact resonance method. Both of them detect damage through changes in the vibration characteristics of the structure at the global and/or local scale.

2.5.1 Vibration-based damage detection

The current state of ageing infrastructure and the economics associated with its repair are motivating factors for the development and application of vibration-based damage identification methods in the civil engineering field. Following an introduction to this technique, damage detection based on global modal parameters applied to large structures in field, as well as to scaled structural members in laboratories, are presented.

Damage in a structure alters its vibration response. As a result, changes are measured in the modal parameters, that is frequencies, mode shapes, and modal damping. These changes are related to changes that occur in some of the physical properties of the structure; namely, mass, damping and stiffness (Pandey and Biswas, 1994; Doebling et al. 1998).

The presence of a crack or localized damage in a structure reduces the stiffness and increases the damping in the structure. From vibration theory, reduction in the stiffness is associated with a decrease in the natural frequencies and a modification of the modes of vibration of the structure. Many researchers have used these characteristics to detect and locate cracks (Pandey and Biswas, 1994).

From a historical viewpoint the effects of cracks upon dynamic properties of a structural element were first analysed in 1943 (Laura et al. 1998). According to this pioneering study the damping ratio is in the range of 0.3% to 0.6% for concrete free from cracks, and for concrete with cracks this value is of the order of 1.3-2.1%. The mean values of logarithmic decrement would be of the order of 3% for sound concrete and 10% for cracked concrete.

Regarding the change in the natural frequencies of the structure as a result of damage or deterioration, Salawu (1997) stated that: "It would be necessary for a natural frequency to change by about 5% for damage to be detected with confidence. However, significant frequency changes alone do not automatically imply the existence of damage since frequency shifts (exceeding 5%) due to changes in ambient conditions have been measured for both concrete and steel bridges within a single day".

Indeed, the above statement was confirmed by a study on temperature variability of modal properties conducted by Cornwell et al. (1999). The field tests performed on a highway RC-deck-steel-girders bridge showed that the modal frequencies vary by up to 6% over a 24-hour period. They also found that an increase in deck-temperature translates into an increase in natural frequencies. Peeters et al. (2001) reconfirmed the effect of temperature on measured modal frequencies. In addition, they proposed a methodology to distinguish the temperature effects from the real damage events.

Efforts to isolate the environmental variability of modal properties were made both through field applications and laboratory tests. Paultre and Proulx (1995) propose a dynamic testing procedure for highway bridges using traffic loads. They validate these experimental procedures in conjunction with finite element analyses for three different bridges in the province of Quebec. An extension of these procedures is presented in Paultre and Proulx (1997) for large structures. A suspension bridge, a gravity dam and the inclined tower of the Montreal Olympic Stadium were tested under ambient and forced vibrations. They further used the dynamic response to calibrate finite element models. They have found that ambient vibration data yielded better results for flexible structures such as the suspended bridge, and forced vibration were more appropriate for the evaluation of certain calibration parameters in finite-element models, such as dam-reservoir-foundation interaction and structural damping (Proulx and Paultre, 1997). Ambient vibrations are also used to investigate long-span suspension bridges by Fujino and Abe (2001).

In situ vibration tests on a highway bridge have been reported by Farrar and Doebling (1999). They applied different levels of damage and performed vibration tests in order to identify and locate damage in the RC-deck-steel-girder bridge. They propose a structural health monitoring scheme based on an improved damage detection strategy. Another dynamic field testing was conducted by Halling et al. (2001) for the condition assessment of bridge bents. They performed vibration tests on an isolated single span of a freeway overpass structure in connection with a series of states of controlled damage and repair. Finite element models were created and calibrated with experimental results. They proposed and optimized several

structural parameters to identify the location and intensity of the damage or CFRP retrofit. Forced vibration methods have also been used for field validation and monitoring of CFRP strengthened concrete bridge deck (Kharbari and Sikorsky, 2002).

Laboratory tests were also performed in order to improve the vibration-based evaluation techniques. Escobar (2001) simulated damage in one or more structural elements of a three-storey RC building. Test results are used to develop a mathematical model for damage detection in structural members expressed as the loss of stiffness. Paultre et al. (2001) evaluated the dynamic behaviour of a two-storey reinforced high-performance concrete structure submitted to increasing seismic loads applied by pseudo-dynamic tests. In order to monitor the damage, a series of forced-vibration tests are carried out after each load-step and are used to track changes in the key dynamic parameters. Fritzen and Bohle (2001) presented the application of model-based damage identification to a seismically loaded two-storey steel structure. Their mathematical model successfully identified crack locations. They concluded that errors in the measured data can cause a false indication of damage.

Farrar and Doebling (1999) used vibration-based tests and statistical pattern recognition for damage detection in a concrete bridge pier. Feng and Bahng (1999) applied the same technique for damage assessment of RC columns retrofitted with FRP jackets. They compare test results obtained before and after a moderate or severe damage is induced. Neural network technique was effective in estimating change in stiffness based in the measured vibration characteristics.

A deteriorated prestressed concrete beam was removed from a bridge and tested to failure. Modal tests identified the damage area of the beam (Allbright et al. 1994). Ambrosini et al. (2000) present results from vibration tests on another prestressed concrete beam. To simulate damage due to corrosion they progressively cut the tendons until 50% of them. A correlation between changes in dynamic parameters and damages was obtained. Razak and Choi (2001) studied also the influence of corrosion on the frequencies and damping of RC beams.

Ndambi et al. (2000) compare different experimental techniques for obtaining modal parameters of a large scale RC beam. Two types of excitation methods were used; the impact hammer and the shaker. They concluded that the natural frequencies given by the two methods are similar. However, the damping ratio is severely affected by the excitation technique, data acquisition parameters and processing method.

Although research intensified in this field lately, there are few problems that remain to be addressed. The main problem is to isolate the environmental effects on the dynamic properties of structures. Water, temperature, and ice are just a few factors that have an important contribution to the response of a structure. A second problem in implementing these techniques in practice is the fact that the damage scenarios used in the laboratory are artificial ones, whereas real-damage scenarios are very different. This difference introduces a difficulty in correlating laboratory results to field data. A third problem is the excitation source for these tests. Shaker excitation is not feasible for continuous monitoring, instead ambient excitation, that is also cheaper, can be used (Peeters, 2001). However, ambient excitation requires a large computational effort in order to "clean" the recorded data.

2.5.2 Impact resonance method

The impact resonance method (IRM) is a technique used to measure the fundamental transverse, longitudinal, and torsional resonant frequencies of concrete prisms and cylinders (ASTM C215-97, 98). This test method is intended primarily for detecting significant changes in the dynamic properties of laboratory or field test specimens that are undergoing exposure to weathering or other types of potential deteriorating influences. Recently, the method was modified and used to detect different flaws in materials such as voids and cracks. In the present study, this technique is employed to detect damage caused by cracking throughout the fatigue and static tests.

The method consists of hitting a supported specimen with an impactor and recording the response by means of an accelerometer. The fundamental frequency of vibration is then determined from the recorded waveform, by using digital signal processing methods. To illustrate this, the test set-up showing the location of the impact and the accelerometer for the

determining the transverse fundamental frequency is presented in Figure 2.5. The configuration shown in the figure is that used for the beam specimens used in this study. For the transverse mode, the nodal points are located at 0.244 of the length of the specimen from each end, in this case is 272 mm. The impactor strikes perpendicular to the surface at midspan and at 0.5 of the height, that is 75 mm. The maximum response occurs at the ends of the beam and there the accelerometer is placed. The accelerometer, sampling rate and the record length in this study were as specified by the ASTM standard.

A similar technique in which the accelerometer is placed a few centimetres away from the impactor was developed. This technique is called the impact-echo method and was first applied in civil engineering in the USA in 1983 (Sansalone, 1997). The impact-echo technique originated from the pulse-echo technique, a method used in automotive and aerospace industries, in which transducers are used to generate stress waves (Popovics et al. 2000).

Among the first applications of the impact-echo technique was the detection of delamination in concrete slabs with asphalt overlays (Sansalone and Carino, 1989). Subsequently, the technique was used to determine flaws in beams and columns (Lin and Sansalone, 1992), concrete pipes, mine shafts and tunnel liners (Lin and Sansalone, 1993). Cheng and Sansalone (1995) successfully determined the minimum width of cracks that can be detected with transient stress waves. Finally, the impact-echo method was applied for flaw detection in reinforced concrete I-girders (Lin and Lin, 1997).

Few studies have been reported in the literature on the application of the impact resonance method to concrete structures. Withmoyer and Kim (1994) determined the concrete asphalt properties by the impact resonance technique. The tests conducted on cylinder specimens showed that the dynamic elastic and shear moduli could be precisely obtained. They showed that this technique could be used to monitor structural changes of asphalt concrete submitted to heating conditions. The IRM was applied to determine the dynamic moduli for early-age concrete (Jin and Li, 2001). They tested cylinder specimens and used the first two natural frequencies for moduli calculations. The measured dynamic response showed very good

consistency and reproducibility. They found a good correlation between the resonance frequencies and the age of the concrete.

Although started in the early 1980s, the large-scale implementation of the impact-echo and impact resonance methods in civil engineering did not happen. On the one hand, most of the studies are performed in the laboratory rather than in the field. As a result, there are difficulties in correlating the laboratory results obtained on specimens with artificial flaws and the field data collected on structural members with real damage. On the other hand, interpretation and processing of the data obtained from these tests required experienced engineers and a large amount of computational effort.

All the studies presented above show the need for new experimental programmes to expand the existing database with results on both durability and non-destructive testing of these innovative FRP and FOS systems. The programme that is presented in the following chapter was especially conceived to address the above-mentioned problems.

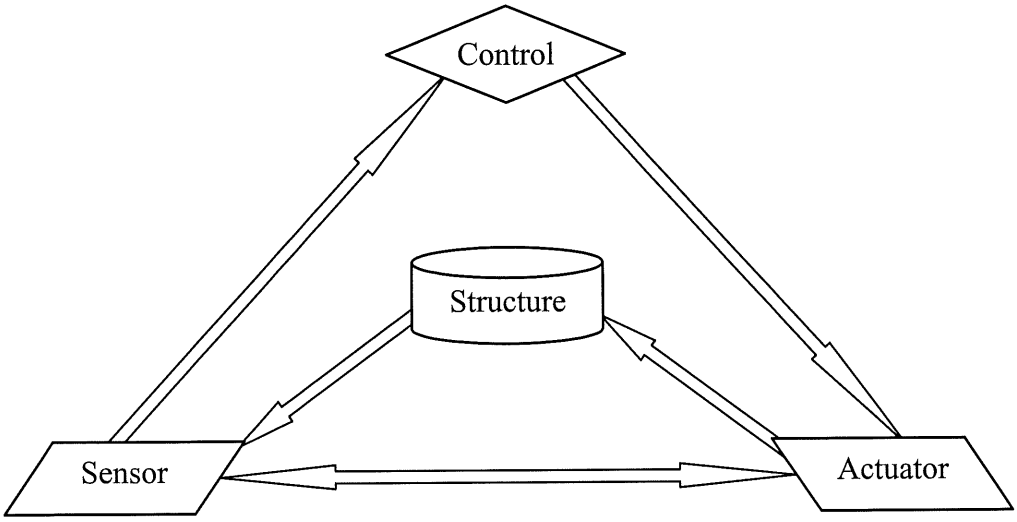

Figure 2.1 Schematic concept of a smart structure

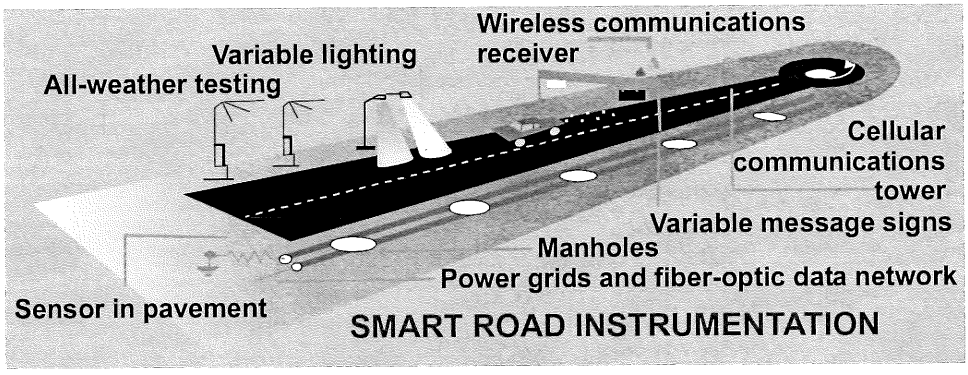

Figure 2.2 Smart road instrumentation (after Darwish and Darwish, 2002)

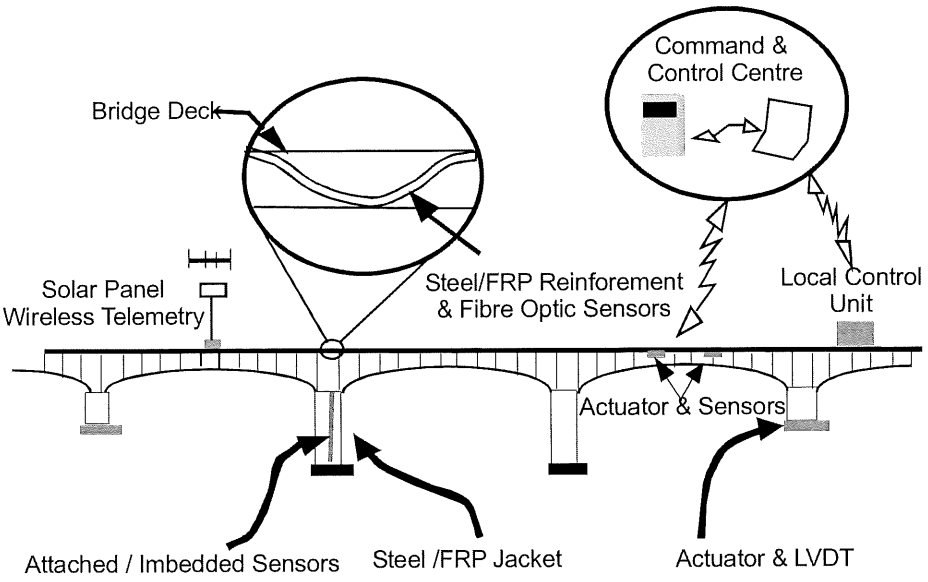

Figure 2.2 Smart bridge (after Darwish and Darwish, 2002)

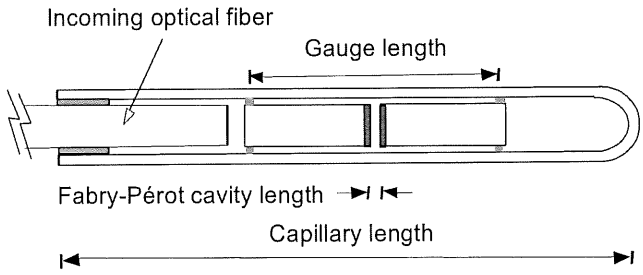

Figure 2.4 Scheme of the Fabry-Perot strain sensor (after FISO Technologies Inc.)

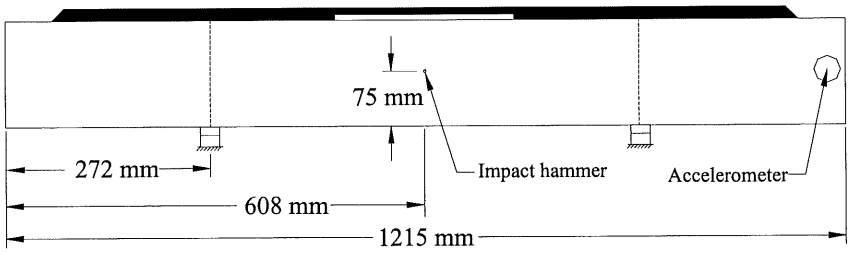

Figure 2.5 Impact resonance method; configuration for transverse mode

3 EXPERIMENTAL STUDY

3. DESCRIPTION OF THE EXPERIMENTAL STUDY

A summary of the research work performed to date on the monitoring of FRP-strengthened structures with FOS showed that there are basically no published data on the durability of the latter under cyclic loading as well as water exposure conditions. In order to have reliable measurements taken by such FOS systems, one must test their capabilities to resist for the entire fatigue life of the structures in a variety of climatic conditions. In addition, there is a lack of data on the environmental durability, that is combined fatigue loading and water immersion conditions, of FRP systems used for external strengthening and repair. When FOS are installed on FRP used to strengthen existing structures, the durability of both FOS monitoring and FRP repairing systems can be assessed at the same time. The extensive program presented here was drawn in order to fill the gap in the existing data on durability of both FRP and FOS systems applied to repair and monitor civil engineering structures.

3.1 Introduction

The experimental program presented here comprises fatigue tests performed on two series of small-scale beams strengthened with two CFRP products. Their response to cycling loading and the influence of different water exposure conditions both on FRP and FOS systems has been addressed. In addition, impact resonance method (IRM) tests have been conducted in order to monitor the change in dynamic characteristics of the strengthened beams throughout the fatigue loading. This technique has also been used to study the influence of FRP system on the vibration frequencies of a concrete beam. This chapter provides the details of the fabrication of the specimens, an overview of the ageing condition using water immersion and fatigue loading, and a description of the data acquisition procedure.

Figure 3.1 schematically presents the experimental program comprising 29 specimens in two series. For each series different parameters were investigated. Series I is composed of 13 beams that were immersed in water prior to the fatigue test. In Series II 16 specimens were tested in fatigue with various loading conditions and numbers of cycles. These beams were also investigated by IRM before the final quasi-static test to failure.

The influence of wet-dry cycles versus continuous immersion is investigated in Series I of the project that is described in section 3.2. The combined effects of ordinary water versus saltwater exposures and fatigue loading are studied. This section also includes the main characteristics of the Series I specimens, the environmental exposure conditions and the apparatus and instrumentation used in the test set-up.

The second series of beams is presented in section 3.3. With the beams of series II the project investigates the influence of loading history on the ultimate capacity of the specimens, as well as on the FOS system. Two loading ranges and three different numbers of cycles are selected for the fatigue loading applied to specimens prior to the failure test. An insight on the reliability of the FOS system and residual capacity of the specimens throughout this testing sequence is obtained. For the same Series II, the impact resonance method, a non-destructive vibration technique, was used to find the change in resonant frequencies of vibration for all the beams. Baseline frequencies are obtained first on undamaged specimens and they are compared with frequencies obtained after the fatigue tests. To support these observations, the impact resonance method was used to monitor the stiffness changes at regular intervals of the cyclic loading for one of the beams.

3.2 Environmental and low-level fatigue loading, Series I

In this section, the first series of tests on 13 beams is presented. Two types of CFRP systems are used to strengthen the RC beams. The beams are then immersed in water, cyclically loaded and finally tested to failure. Section shows the main characteristics of the tested specimens and the properties of their constituent materials, as well as the environmental exposure conditions. A description of the loading apparatus, the instrumentation and the data acquisition systems end this section.

3.2.1 Specimens and constituent materials

The typical geometry and internal reinforcement of the tested beams are shown in Figure 3.2(a). Thirteen specimens 1100-mm-long between the supports, with a 100 x 150 mm section, were fabricated. Since it was not possible to cast all beams at the same time, three batches of normal-strength ready-mixed concrete with a maximum aggregate size of 10 mm

were used. The concrete strength was determined from tests on 100 x 200 mm cylinders and is given in Table 3.1. At least three cylinders were tested for each concrete batch. The average value for the three batches is 49.3 MPa. The internal reinforcement is made of smooth and undeformed bars 6.35 mm in diameter and provides the minimum steel quantity required by the Canadian Standard CSA-A23.3 (1994) for reinforced concrete structures. The tested steel bars exhibit a yield strength of 600 MPa and a Young's modulus of 200 GPa.

Twelve beams were externally reinforced with CFRP: six beams with a Sika CarboDur unidirectional plate, as shown in Figure 3.2(b), and six beams with Mitsubishi Replark sheets, as illustrated in Figure 3.2(c). To improve the bond between the concrete and FRP, surface preparation by sandblasting was the only procedure necessary for all the FRP-strengthened beams. The main properties of the fibre-reinforced polymers used in the study are indicated in Table 3.2. They represent the values given by the manufacturer. The 50-mm-wide CarboDur strips were bonded to the tension face of the beams with the proprietary mortar of the system on a 400 mm length at both ends thus leaving 260 mm unbonded in the central portion. This configuration was selected to avoid concrete crushing and to trigger failure by delamination of the CFRP near the centre. For the Replark-reinforced specimens, the two layers, 50 mm in width, were impregnated with epoxy resin, and bonded on the full length of the beams. In addition, external glass-fibre-reinforced polymer (GFRP) U-shaped stirrups were bonded at both ends to provide sufficient anchorage to the CFRP reinforcement. The remaining beam was not strengthened externally and was used as a reference specimen.

3.2.2 Exposure conditions

After strengthening, the beams were submitted to accelerated ageing conditions. The first type of ageing process was a series of wet-dry cycles consisting of immersion in water at 21°C for five days, followed by two days of drying at 27°C under constant airflow. This seven-day cycle was repeated for a total of 13 weeks. The second type of ageing condition consisted of keeping the beam immersed in water at 21°C for 160 days. For the two procedures, there was an equal number of specimens immersed in ordinary water and in saltwater. In the latter case, saltwater was obtained with a concentration of 4% by weight of sodium chloride (NaCl). The thirteen specimens and their exposure conditions are summarized in Table 3.3. The table lists

the reference specimen S0, six beams strengthened with CarboDur plates in the C-series, and six specimens in the R-series, consisting of Replark-reinforced beams. For each series, the two specimens kept at ambient laboratory conditions are numbered 1 and 2. The letters W or I identify the specimens that underwent the wet-dry cycles or the continuous immersion, respectively. When the procedure took place in saltwater, the letter S is added to the beam identification.

3.2.3 Instrumentation

Prior to immersion, all specimens were instrumented with conventional strain gauges and fibre optic sensors. Two strain gauges were placed on the concrete surface and two on the rebars, as shown in Figure 3.2(a), to monitor the behaviour of the reference beam. Two strain gauges were placed on the rebars also for six of the CFRP-strengthened specimens. Prior to the fatigue test, four additional gauges were installed on the CFRP, in order to measure the onset of delamination along the CFRP-concrete interface. Their location depended on the type of CFRP reinforcement, as shown in Figures 3.2(b) and (c). All the conventional gauges were purchased from *Micro-Measurements*. The type N2A-06-20CBW-120 was used for concrete and the type CEA-06-250UW-120 for steel and CFRP. The load cell was a part of the actuator, and two LVDTs measured the midspan deflection of the beams.

In addition to this conventional instrumentation, extrinsic Fabry-Perot FOS were installed on the CFRP reinforcement. All the FOS employed in this study were purchased from Roctest Ltd. and were of the same type. The strain range for this type of sensor is from -1000 με to $+10\,000$ με as stated by the manufacturer. The exposed beams are instrumented with one FOS installed before exposure and another FOS installed after. The FOS are identified as follows: the aged one is denoted as FOS-A, and the one installed after the exposure was identified as FOS-B. Between the two FOS, one electrical gauge was placed to provide a reference strain signal, positioned as indicated in Figure 3.2(d).

The FOS installation was performed using the M-BOND AE-10 adhesive for the CarboDur composite plate and, for the Replark strips, the epoxy impregnation resin provided by the Mitsubishi manufacturer was used. The installation procedure is similar to the one described

in the Roctest Manual (2000). After the bonding, the water exposed FOS were environmentally protected against water and moisture using the MCoat FT Teflon film and M-Coat FB butyl rubber sealant. The protection procedure is schematically represented in Figure 3.3. First, the piece of Teflon film, large enough to fully cover the sensor, was applied. Then, the patch of butyl rubber sealant was placed. The other FOS sensors were protected with a layer of an epoxy resin. It is worth mentioning that the procedure used to protect these sensors is in accordance with the specification of the manufacturer and is very similar to that proposed by ISIS Canada (2001c).

3.2.4 Testing procedure

After completion of the environmental exposure, the beams were submitted to flexural cyclic loading, followed by a quasi-static test under four-point bending. For the entire testing sequence two identical loads were applied on the beams as shown in Figure 3.2(a). The fatigue test consisted of 401 000 cycles at a frequency of 2 Hz. The load level oscillated between 15 and 35% of the calculated yielding moment. These minimum and maximum loads, estimated according to methods described in the CSA-A23.3 standard and in the ISIS Canada (2001b) design manual, are given in Table 3.4. This load range corresponds to service load conditions that can be expected in actual bridges.

The fatigue load was applied using a MTS hydraulic actuator of 100 kN capacity controlled by the TestStar-II software, the same software used for data acquisition. The specimens were first loaded statically up to the minimum value of the cyclic load identified in Table 3.4, then the fatigue load oscillated from this level to the maximum value. Between these extreme loads, the CFRP plate always remained in tension. The sinusoidal loading was force-controlled using the TestWare-SX process module. Readings at minimum and maximum loads were taken at every 2000^{th} cycle for the entire duration of the test. Full cycle readings during the test were taken according to the following sequence: at the first cycle, at every 200^{th} cycle to 1001, and at every $20\,000^{th}$ cycle up to 401 000. At these preset times, the loading frequency was reduced to 0.05 Hz in order to obtain more data points on a typical cycle. Considering the time necessary to prepare the specimens, the frequency of the loading, and other laboratory constraints, a minimum of four working days was necessary to test each beam.

After completion of the fatigue loading, the beams were loaded quasi-statically up to failure under the same four-point bending arrangement. The quasi-static load was applied using a Baldwin press of 267 kN capacity at a loading rate of approximately 0.1 kN/s. Data were recorded on a DORIC system at every 0.1 kN load increment. For these tests, steel plates were used at the supports and at the loading points in order to avoid concentration of stresses and potential premature failure due to concrete crushing.

For all these tests, the FOS were conditioned with the reading unit UMI 8. The reading unit and the sensors were acquired from Roctest Ltd. The UMI 8 is a fibre optic signal conditioner for eight different sensors, and at the same time performs data acquisition for up to 50 000 samples. Data can be interrogated in digital and analog formats. In this study, the analog output was stored in the same computer used for the acquisition of the other data. Photographs of the test set-up, specimens, water exposure conditions and instrumentation can be found elsewhere (Raîche 2000).

3.3 Low-level versus high-level fatigue loading, Series II

This section introduces the 16 beams tested in the Series II of the program. All beams were fabricated with the same geometry and from similar materials as the beams in Series I. However, the only external reinforcement used this time is the CarboDur plate. The first series of tests focused on the effect of various types of water immersion on the fatigue behaviour of the instrumented beams. This second series was intended to isolate the effect of two other parameters: the number of fatigue cycles and the load amplitude. The influence of these two parameters on the stiffness degradation of the beams are eventually correlated to the results of the impact resonance method which is a non-destructive technique.

3.3.1 Specimens, instrumentation, testing procedure

The beams in this series were fabricated by following the procedure described in subsection 3.2.1. The beams were poured from one batch of ready-mixed concrete. Its strength was measured at three different times along the testing program and is indicated in Table 3.5. Similar conventional and FOS instrumentation was used and is described in subsection 3.2.3.

Since the beams of this series were not exposed to water, only one extrinsic Fabry-Perot sensor was sufficient for each beam. The FOS sensor had a strain range of –1000 με to +5000 με as stated by the manufacturer. This operating range is different from the one used in Series I, for the following reason. All sensors acquired for the first series of tests were not capable of measuring strains up to the maximum limit of +10 000 με. A possible cause for this is addressed later on in chapter 5. Following a discussion with a specialist of Roctest, it was made clear that there were some steps in the manufacturing process that limited the stated operating range. Thus, the second batch of sensors came with a range that was almost attained and their results are presented in chapter 5.

Of the 16 specimens in this series, one was used specifically for the IRM test, and is discussed in subsection 3.3.2. The other 15 beams were submitted to two loading ranges referred to as "low-level" and "high-level" of fatigue loading. The former case is when the load level oscillates between 15 and 35% of the calculated yielding moment and for the latter the load extremes are from 35 to 75% of the yielding moment. The fatigue loads used for this series of beams and are presented in Table 3.6. In addition, the beams were tested with three different number of cycles: 400 000, 800 000 and 2 000 000. In order to measure their residual capacity, all beams were tested quasi-statically to failure.

Due to the extent of the program and the long duration of the fatigue tests, and having in mind the successful tests at 2 Hz for the beams in Series I, it was thought that a frequency of 3 Hz would be appropriate for this second series of beams. Thus, fatigue cycles were applied at a frequency of 3 Hz for three beams. Preliminary results from these first tests showed that the longitudinal steel reinforcement yielded. This was not expected. Therefore, the frequency was lowered to 2 Hz for the rest of the program to avoid this unexpected rebar yielding.

The same testing equipment as for the first series of beams was used for both the fatigue and static tests. Most of the parameters were kept constant, but the sequence of readings was modified to include more initial cycles. Thus, full cycle readings were taken at the 1st and every 10th cycle to 200, at every 200th cycle to 1001, and at every 20 000th cycle up to 801 000. Then, the distance between two consecutive cycle readings was increased to 100 000

cycles up to the 2 001 000th cycle. Until cycle 801 000 readings at minimum and maximum loads were taken at every 2000th cycle; readings were then spaced at every 10 000th cycle to the end of the 2 001 000 cycles. Preparation and testing for 801 000 cycles of a beam at 2Hz took seven working days. In the case of 2 001 000 cycles, it took 13 working days to test only one beam. Following the fatigue loading the beams were tested to failure in a similar manner as presented in subsection 3.2.3. The only difference for the present tests is that no steel plates were used at the supports and load points.

The 16 specimens and their loading conditions are summarized in Table 3.7. The table lists the specimens NA and replica NB that were not cyclically loaded, eight beams loaded with a low level cycling in the L-series, and seven more specimens in the H-series, consisting of high load-level cycled beams. For each series, specimens that were tested for 400 000, 800 000 and 2 000 000 cycles are identified by 400, 800 and 2000, respectively. Letters A to C are added to the identification to indicate replica specimens submitted to the same case of loading. The remaining beam of the 16 specimens in this series, denoted LIRM in Table 3.7, was fatigue tested for 2 000 000 cycles only for the purpose of impact resonance investigation.

A main difference from the previous series of tests is that, for 15 beams in the current series, the impact resonance technique was employed in order to compare vibration characteristics before and after the fatigue tests. The 16th beam in this series was tested for the specific purpose of monitoring changes in the dynamic properties throughout the fatigue testing. The next subsection is dedicated to these specific impact resonance tests.

3.3.2 Impact resonance method

Fifteen beams out of 16, that were tested as described above, underwent a final test, the impact resonance test. Reference frequencies of vibration for three modes were measured on two specimens before any fatigue testing. At the end of the fatigue loading, the beams were tested by the impact resonance method to measure changes in the three natural frequencies.

The last of the 16 beams in this series, LIRM, was tested for two million cycles under low-level fatigue, especially for the purpose of monitoring the change in stiffness along the whole

fatigue test. The impact resonance tests were conducted initially, when no loading was applied, and then following a certain sequence. The natural frequencies were thus measured after the first cycle and after the tenth, 50^{th}, 100^{th}, 200^{th}, 1000^{th}, 9000^{th}, $50\ 000^{th}$, and $100\ 000^{th}$. From the $280\ 000^{th}$ cycle onward measures were taken at approximately each $250\ 000^{th}$ cycle until the end of the two million cycles.

For each of these IRM tests, the fatigue load was removed and the beam was placed on a table. For each vibration mode, the specimen, the accelerometer as well as the impactor are located in a specific configuration. In the case of the transverse mode, Figure 3.4(a), the beam is turned upside down and placed on two supports located at almost a quarter of the span from each end of the beam. The impact hammer strikes perpendicular to the surface at midspan at the mid-height of the beam. The amplitude of the response is largest at the ends of the beam, where the accelerometer is located. The test set-up showing the location of the impact and the accelerometer for the other fundamental frequencies, corresponding to the longitudinal and torsional modes, is presented in Figures 3.4 (b) and (c).

For accurately determining each resonant frequency, the specimen must be supported so that it may freely vibrate in that specific vibration mode. Thus, for the present investigation the specimens were supported on small wooden pieces on top of which was placed a thin rubber pad. The accelerometer was attached to the specimen with a plastic material using a hot-glue gun, and the low-amplitude impact was applied with an ordinary hammer. A lightweight accelerometer was used in this study. The measured acceleration signal is recorded and processed with a waveform analyzer produced by Andec Manufacturing Ltd. The sampling rate was set to 20 kHz and the record length to 1024 points, as specified by ASTM C215-97. The frequency response spectra produced by the waveform analyzer had an about 19 Hz resolution with a low-pass filter of 100 Hz. Three frequency responses to the hammer impact were recorded for the three vibration modes of each test of every beam.

The response acceleration is first amplified and then recorded by the Andec system. The frequency response function is calculated and displayed on the screen in real time. This frequency response function is of interest and is saved on the hard disk of the system. For each

IRM test, three natural frequencies are sought: the longitudinal, transverse and torsional. For each of the three modes of vibration, three responses are saved in order to avoid any measuring error. Thus, for one impact resonance test, nine responses are actually recorded. In addition to these tests, visual observations are made and the crack pattern is drawn.

3.4 Summary

This chapter presents the two series of beams tested in this program. A summary of the 29 beams as well as the damaging conditions are given in Table 3.8. In the first series, the influence of both water exposure and fatigue loading on the residual strength of the beams is investigated. The beams in the second series are damaged only through fatigue loading before measuring the ultimate capacity. The following parameters are included in the test program: continuous water immersion, wet-dry cycles, service fatigue and severe fatigue loading. The water exposures were made in either ordinary or saltwater. The fatigue loading was applied with three different numbers of cycle

s. In addition, impact resonance tests were performed to quantify the change in resonant frequency as a result of fatigue cycling for the beams of the second series. One beam was tested by the same technique at preset instants throughout the fatigue loading in order to monitor changes in the natural frequency. The next chapter will provide the various results obtained on the two series of beams showing their fatigue and post-fatigue quasi-static behaviour to failure.

Table 3.1 Properties of the concrete, Series I

Batch	f_c' 28 days (MPa)
1	48.3
2	52.4
3	47.3

Table 3.2 Properties of FRP systems

System	E_{frp} (GPa)	ε_{frp} (%)	f_{frp} (GPa)	t (mm)
Sika CarboDur	155	1.6	2.4	1.20
Mitsubishi Replark	230	1.5	3.4	0.11
Fibrwrap Tyfo	28	2.0	0.6	1.30

Table 3.3 Specimens and water exposure conditions, Series I

Exposure Condition		No reinforcement	CarboDur reinforcement	Replark reinforcement
Ambient	No ageing	S0	C1, C2	R1, R2
Normal water	160 day immersion	-	CI	RI
	13 wet-dry cycles	-	CW	RW
Salted water	160 day immersion	-	CI-S	RI-S
	13 wet-dry cycles	-	CW-S	RW-S
Total specimens			13	

Table 3.4 Loads applied in fatigue tests, Series I

Specimen	P_{min} (kN)	P_{max} (kN)
S0	3.4	8.0
C series	6.8	15.9
R series	4.4	10.2

Table 3.5 Properties of the concrete, Series II

Day	f_c' (MPa)
190	48.1
220	50.2
280	51.6

Table 3.6 Loads applied in fatigue tests, Series II

Specimen	P_y (%)	P_{min} (kN)	P_{max} (kN)
L-series	15-35	6.8	15.9
H-series	35-75	15.9	34.1

Table 3.7 Specimens and loading conditions, Series II

Loading Condition		Specimen
% of P_y	Cycles	
0	0	NA, NB
15-35	400 000	L400A, L400B
	800 000	L800A, L800B, L800C
	2 000 000	L2000A, L2000B, LIRM
35-75	400 000	H400A, H400B
	800 000	H800A, H800B
	2 000 000	H2000A, H2000B
Total specimens		16

Table 3.8 Summary of damaging conditions for 29 beams to be tested

Beam	Water exposure				Load						
	Normal		Salt		Fatigue						Quasi-static
	Wet-dry	Immer.	Wet-dry	Immer.	15-35% M_y			35-75% M_y			
					400k	800k	2000k	400k	800k	2000k	
Series I, 13 beams											
S0, C1, C2, R1, R2					+						+
CW RW	+				+						+
CI RI		+			+						+
CW-S			+		+						+
CW-I CI-S RI-S				+	+						+
Series II, 16 beams											
NA, NB											+
L400A, L400B					+						+
L800A, L800B, L800C						+					+
L2000A, L2000B, LIRM							+				+
H400A, H400B								+			+
H800A, H800B									+		+
H2000A, H2000B										+	+
Total beams	29										

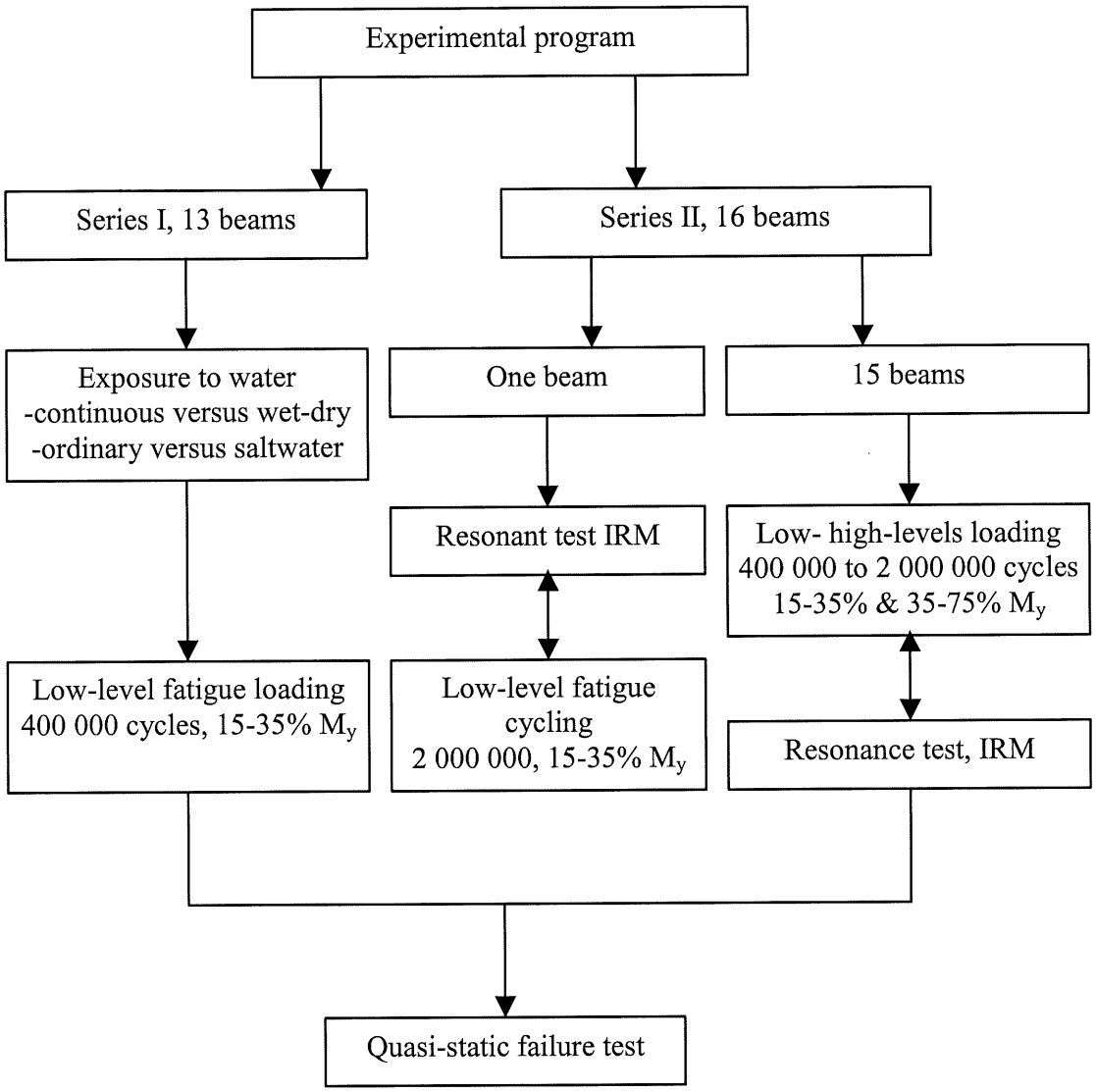

Figure 3.1 Experimental program

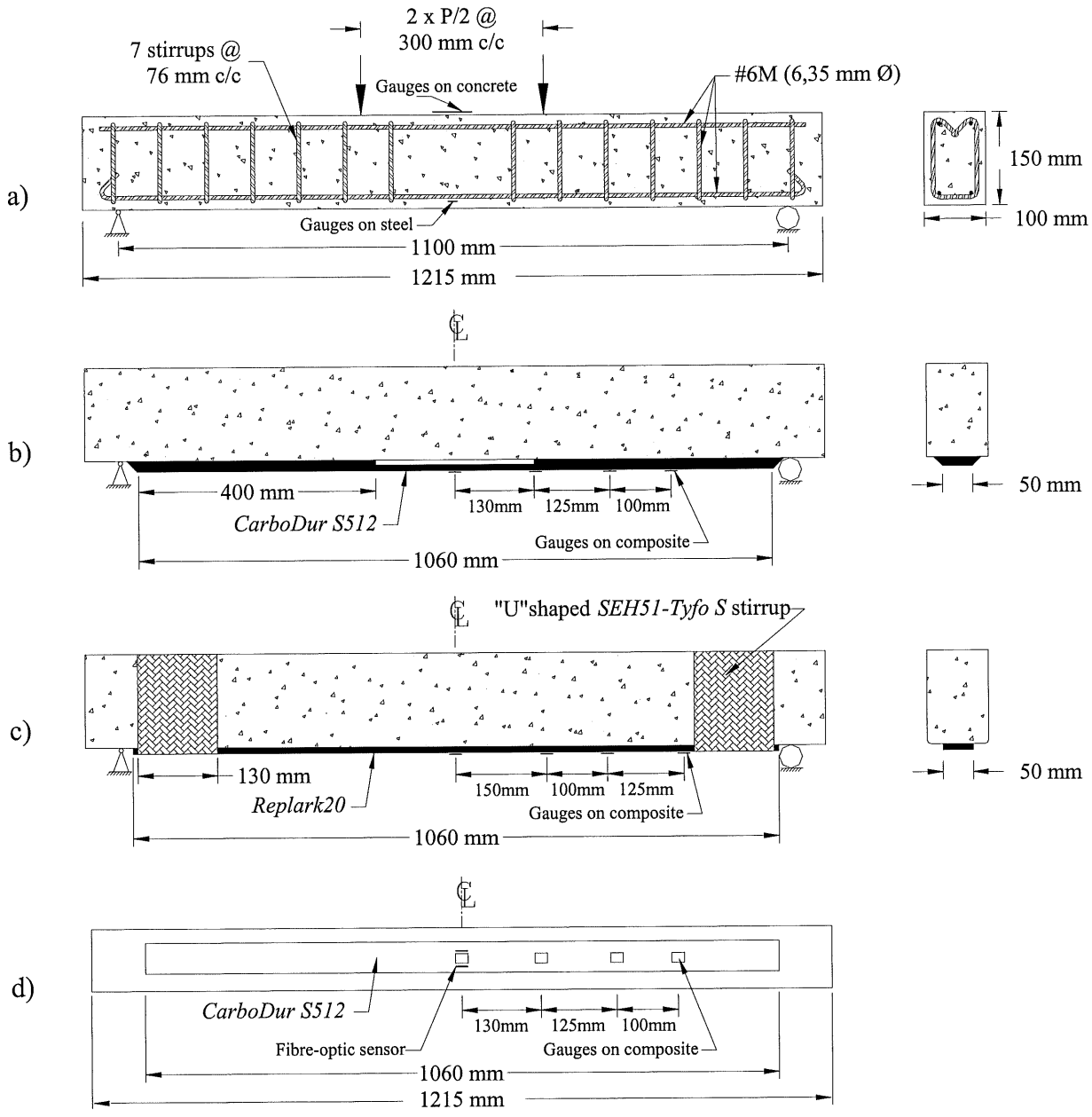

Figure 3.2 Beam geometry, reinforcement and instrumentation

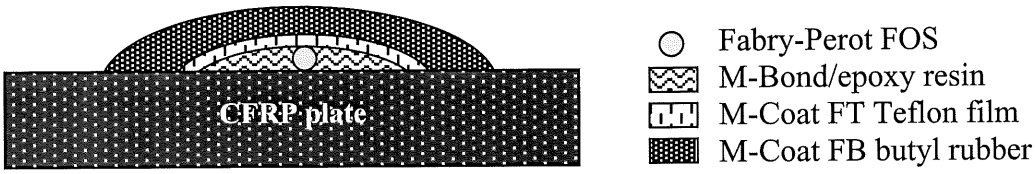

Figure 3.3 Protection of the Fabry-Perot fibre-optic sensor

a) Transverse mode

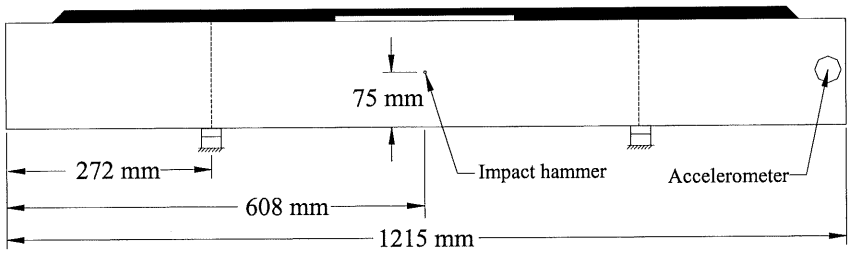

b) Longitudinal mode

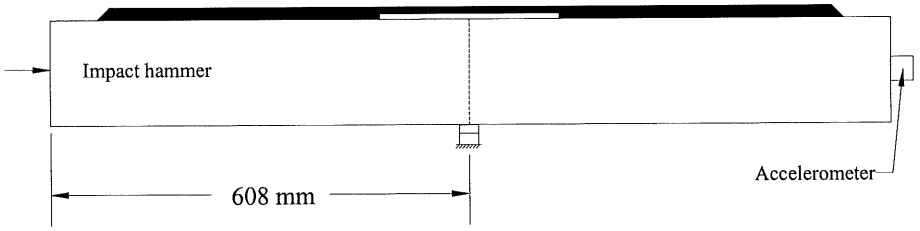

c) Torsional mode

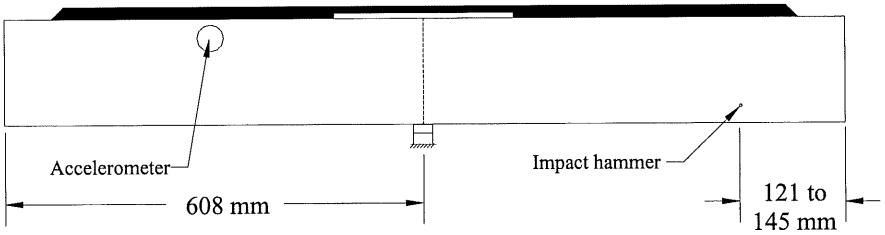

Figure 3.4 Set-up for impact resonance tests

4 RC BEAMS WITH CFRP

4. BEHAVIOUR OF THE RC BEAMS STRENGTHENED WITH CFRP

This chapter presents results from the fatigue and static tests performed on the beams described in the previous chapter. It provides an analysis of the response of the specimens by means of visual observations and measurements taken with conventional equipment. These include measurements obtained by means of displacement transducers, load cells, and electrical gauges. The discussion that follows focuses on the behaviour of the CFRP-concrete interface throughout the tests and is based on results measured by the strain gauges and by the load cells. The results presented in this chapter consist mainly of the strain response of the beams. Sections 4.1 and 4.2 are dedicated to presenting the results of the first series of tests. The reference beams are first discussed in section 4.1; the behaviour of the beams submitted to water exposures is presented in section 4.2. The following sections introduce the results from the specimens tested in Series II of the program. The results for low-level fatigued specimens are followed by the results for beams submitted to high-level fatigue and are both presented in section 4.3. A summary of the results presented concludes this chapter.

4.1 Reference beams, Series I

Valuable experimental data were obtained from fatigue tests as well as failure tests through both measurements and observations. For each specimen, a set of curves was produced. From these curves the discussion that will follow will be based on strain versus number of cycle curves and mean shear stress versus relative load curves. In addition, most significant test results are presented in tabular format. Data presented both graphically and tabular are discussed in the following.

A typical graph used throughout this chapter and the following ones is introduced here. It represents the change in minimum and maximum strains as a function of number of cycles. For all the tests, the fatigue load starts with a quasi-static ramp to the minimum cycling load. This is represented schematically in Figure 4.1(a), where the strain measured by a strain gauge is plotted against testing time. Then, the cycling begins with load increasing to the maximum value, and decreasing to the minimum value. This load increasing and decreasing forms the first cycle of the fatigue loading. From all the strains measured by the gauges two are of

particular interest. They correspond to the two extreme loads and are represented by the solid square for the maximum value, and the clear square for the minimum value. Figure 4.1 (b) shows schematically these extreme strains plotted this time against the number of cycles.

From the 13 beams in the first series, which all underwent cyclic loading at low-level, the five reference specimens remained at the ambient temperature of the structure laboratory, while the others underwent the ageing procedure described in the previous chapter. The reference specimens included the single beam S0 with no external CFRP reinforcement, and two control beams for each type of CFRP reinforcement.

For the S0 beam, measurements were obtained from the two strain gauges on the concrete surface and from two other gauges on the steel rebars. Readings from each two gauges were averaged and presented graphically in Figure 4.2. The measured maximum strain in the steel rebars increased gradually throughout the cyclic loading and reached a maximum of 911 με at the end of the fatigue test. This value is the average of the readings from two gauges placed on the parallel rebars. The maximum compressive strain in the concrete remained mostly constant throughout the 401 000 cycles. A slight decrease was observed towards the end of the test. The strain value in the concrete is also the average of two gauges placed on the compression fibre. The maximum compressive strain -102 με was obtained at the last cycle of the fatigue test.

Table 4.1 compiles the most significant fatigue test results for S0 and the other beams of the Series I. The beam designation is given in the first column of the table. The second and the third columns give the concrete strength $f'_{c\text{-}28}$ at 28 days and f'_c at the testing time, that were obtained from 100 x 200 mm cylinders. The results in the next two columns are the maximum strains measured at midspan, $\varepsilon_{s,fat}$ in the steel reinforcement, and $\varepsilon_{frp,\,fat}$ in the CFRP at the end of the last cycle. Apart from these data, static test results are indicated in the next columns of Table 4.1 and will be discussed in the sections dedicated to these tests. Because only some of the beams carried instrumentation on the rebars, only the corresponding cells in the table show values.

The behaviour of CFRP-strengthened beams will naturally be more complex than that of the S0 specimen. Of the four reference beams of that type, the following discussion will be based on the results obtained from beams C1 and R2 that carried more instrumentation and gave representative results.

4.1.1 Fatigue behaviour

The evolution of the strain extremes in the CFRP-strengthened section through the fatigue loading are presented in Figure 4.3 for one CarboDur-reinforced beam C1 and one Replark-reinforced beam R2. For the beam C1 submitted to the cyclic loads from 15 to 35% of M_y, the strain history in the steel rebars and at four different locations along the CFRP reinforcement is recorded in Figure 4.3(a). For clarity purposes, a limited number of recorded points are shown in the figure. Results from each gauge are represented by two curves corresponding to the minimum and maximum cyclic loads. There are therefore five sets of such extreme strain curves.

The central gauge on the CFRP is considered first. The curve with clear rectangles shows the minimum strains, and the one with solid rectangles indicates the maximum strains through the 401 000 cycles. During the first cycle, the extreme strain values were 1602 με and 2112 με. At the same time, Figure 4.3(a) shows that the strains in the rebars ranged from 814 με to 1364 με. These values are consistent with theoretical strain estimates based on a recent design manual (ISIS Canada, 2001b). As the number of cycles increased, the extreme strains were found to change gradually. For the CFRP, they increased to values comprised between 1698 με and 2306 με, while on the steel rebars, they decreased to values between 768 με and 1278 με. These variations indicate a gradual change in beam stiffness, and implicitly in the position of the neutral axis, as the number of cycles increases. Indeed, two cracks appeared at the initiation of the loading, propagated continuously during the test. Gauges located along the beams provide additional information of interest. For instance, it can be observed that, at 125 mm from the beginning of the joint, or 255 mm from midspan, the triangle curves in Figure 4.3(a), there is a continuous increase between the initial and final strains. Thus, at the first cycle the maximum strain is about 500 με, and this value tripled until the last cycle to reach almost 1500 με. In addition to that, the difference between the extreme strain values

increases significantly; that is, from the initial value of 200 με to 500 με at the end of the test. These effects support the initial assumption that the vicinity of the CFRP joint would be the most strained section of the beam. Moreover, the occurrence of a crack close to this location confirms the rapid changes in local stiffness.

Of all the data presented in Figure 4.3(a) and discussed above, the maximum strain values at midspan, $\varepsilon_{s,fat}$ in the steel and $\varepsilon_{frp,\ fat}$ in the CFRP, are listed in Table 4.1. The data for the identical reference beam C2 are also given in the table. As they indicate, the C2 specimen generally behaved in the same manner as C1. However, the strain $\varepsilon_{s,fat}$ shown in Table 4.1 for beam C2 is significantly lower than that for the beam C1. This unexpected result is hard to explain but the long delay between the testing of the two beams, and the necessity to reinstall the test set-up, may explain part of the difference. For instance, the concrete and mortar curing may have enhanced the CFRP contribution in the fatigue load carrying mechanisms.

The strain extremes for the Replark-strengthened beam R2 are presented in Figure 4.3(b). For the entire cyclic loading it can be observed that a very low level of strain was measured at most locations. The first surprising result concerns the steel rebars: according to the initial calculation, their measured strains should have been close to the ones obtained for beam C1. Obviously the applied loads did not produce the expected strain as the comparison between Figures 4.3(a) and (b) reveals.

The other unexpected result is the location of the maximum strain in the CFRP reinforcement. Instead of occurring at midspan it is actually located under the concentrated load. Apparently, the two CFRP reinforcement schemes behave in a very different manner at low levels of loading. In the case of the wet lay-up application, such as the Replark product reported here, the distribution of strain along the CFRP reinforcement seems to be very sensitive to cracking. For instance, vertical cracks showed up in the beam R2, at the two central stirrups, soon after the initiation of the fatigue loading. The highest recorded strain at low levels of loading remained in the area of those cracks. No other cracks appeared on the beam until the completion of the fatigue loading, and the highest measured strain remained at the same location. This effect may be more noticeable because of the small scale of the specimen.

Strain values measured in the last cycle of the test are listed in Table 4.1 for both the R1 and R2 specimens. These values indicate a similar response of the two beams. Overall, strain evolutions for R1 are similar for to those presented in Figure 4.3(b) for beam R2. In addition to the results presented above, some other graphical results are presented in Appendix A. These represents typical load-deflection curves obtained during the 400 000-cycle test.

4.1.2 Post-fatigue behaviour of beams under static loads

Following the fatigue test, the beams were loaded quasi-statically to failure. Results from these tests, given in Table 4.1, include the ultimate load $P_{u,exp}$ and corresponding deflection Δ_u at midspan, and the strains $\varepsilon_{frp,u}$ in the CFRP and $\varepsilon_{s,u}$ in the steel rebars at that section. The design load P_{des} for the CFRP-strengthened beam, calculated according to the ISIS Canada design manual (2001b) and assuming concrete crushing failure or breakage of the CFRP lamina, is also given. This estimate uses the equivalent concrete block stress theory and resistance factors but does not take into account the softening effect caused by the fatigue loading. For the control beam S0, the predicted and measured values of the ultimate load are identical.

For the CarboDur strengthened beams C1 and C2, failure occurred at a load $P_{u,exp}$ about 10% lower than predicted. In both cases the failure of the beam was initiated by CFRP plate debonding, rather than concrete crushing as assumed for predicting P_{des}. However, even though the damaging effect of fatigue appears significant, it should be emphasized that C1 and C2 still reached an ultimate load 150% higher than S0. On the other hand, the ultimate deflection of both beams was 30 to 40% lower than that of S0. These data confirm the loss of deformability of CFRP-strengthened beams over conventional RC beams.

The failure mode reported above being delamination, it is important to evaluate the shear stresses at the CFRP-concrete interface. For instance, the strain measurements from the gauges located along the CFRP may be used for that purpose. A method to calculate the average shear stress for each region between two consecutive strain gauges was developed by Bizindavyi and Neale (1999). The method allows us to visualize the evolution of the shear

stress distribution along the joint as the load increases. For the beam C1, the average shear stress for two intervals is plotted against the relative load in Figure 4.4(a). For the interval comprised between 0 and 125 mm from the beginning of the joint, the shear stress increases almost proportionately with the load, then decreases suddenly. The shear stress in the interval comprised between 125 and 225 mm remains almost constant throughout the test. This shows that the largest amount of the shear stresses is carried in the first portion of the joint, where it reaches 1.5 MPa. Overall, the C2 behaviour at CFRP-concrete interface is similar to that of the C1 beam. However, in this case the second portion of the joint contributes in load carrying mechanisms. The maximum calculated mean shear stress reached 2.1 MPa for specimen C2.

Static test results for the Replark-strengthened beams R1 and R2 can also be found in Table 4.1. The observed failure mode for R1 was debonding of the lamina and the breakage of the external FRP stirrup. For the beam R2 the failure mode was triggered by the breakage of the lamina, as predicted by the models. For the two beams the ultimate load and ultimate deflection were significantly higher than for the unreinforced specimen S0. The high deformability of the Replark-strengthened beams may be related to the flexibility of the reinforcement and the nature of its application, layer by layer.

Figure 4.4(b) shows the shear distribution at the CFRP-concrete interface for the beam R2. The average shear is calculated for three intervals along this joint. From the beginning of the loading to about half the ultimate load P_u, most of the shear stress was carried between the centre of the beam and a point located about 250 mm away. Then a crack was initiated at the interface and the load was suddenly transferred to the third interval where the shear stress reached a maximum of 3.7 MPa. The beam failure was initiated by the breakage of the CFRP, as predicted by the model. At the end of the test, five vertical cracks and one shear-flexural crack were observed.

4.2 Beams submitted to environmental exposure, Series I

The eight specimens exposed to accelerated ageing conditions, listed in the first column of Table 4.1, consist of four CarboDur-strengthened and four Replark-strengthened beams. In each case two beams were submitted to wet-dry cycles and the other two were immersed in

water. The ageing of the CarboDur-strengthened beams CW, submitted to wet-dry cycles, and CI, submitted to continuous immersion, took place in ordinary water. The only difference between these beams and CW-S, CI-S was the exposure condition, in saltwater for the latter. A similar combination of exposure conditions was selected for the Replark-strengthened beams: the RW and RI were exposed in ordinary water and RW-S and RI-S, in saltwater. After ageing the eight beams were tested under cyclic and quasi-static loads following the same procedure as for the five control beams.

The effect of long-term immersion in water is a significant shrinkage of the concrete specimens. The effects of this shrinkage are different, depending on the type of external CFRP reinforcement. For instance, in the case of the Replark-strengthened beams, the full-length bonding of the CFRP sheets ensures strain compatibility between the two materials at their interface. However, in the case of a CarboDur plate, unbonded in the central portion of the beam, a significant buckling of the CFRP was observed, to such an extent that it could be seen with the naked eye. Once the beam was loaded for the cyclic test, that buckling of the CFRP plate disappeared. In fact the minimum fatigue load applied was sufficient to keep the plate in tension and unbuckled. For that reason, the difference in initial deformation observed in the aged specimens was not expected to alter the beam performance after initiation of the cyclic loaded.

The following discussion will focus first on the fatigue behaviour of the beams and will be followed by the analysis of their post fatigue response under static loading.

4.2.1 Fatigue behaviour

The effect of the long-term immersion of the beams will first be discussed. Figure 4.5 presents results for the CI and RI beams that underwent 160-day continuous immersion in ordinary water. These results represent strain histories at four locations on the CFRP and in the rebars, at the same location as for the reference beams discussed previously. Each water-immersed beam strengthened with two CFRP systems, CarboDur plates and Replark sheets, is compared to the corresponding reference beam. First, the CFRP plate system response is analysed by

comparing results obtained for CI and C1, and then follows a discussion about the CFRP layered system.

A comparison between Figures 4.5(a) and 4.3(a) reveals that, under identical cyclic load amplitudes, the difference between maximum and minimum deformation at a given location for the CarboDur-strengthened beams was the same. In the central section of the beams it reached approximately 500 με, whether or not the beams had been submitted to immersion.

A major difference between Figures 4.5(a) and 4.3(a) lies in the position of the two strain curves of the CFRP plate at midspan in relation to the two strain curves of the steel reinforcement. It can be observed that the measurements taken on the CFRP plate are much lower for the beam submitted to immersion than for the reference beam. One explanation for this peculiar situation is the fact that the strain gauge on the CFRP plate was installed after the completion of the 160-day immersion. The CFRP plate was already buckled towards the outside of the beam at that moment. This buckling produced tension on the exterior face of the plate before any loading took place, thus affecting the readings of the strain gauges located on the CFRP. As the loading ramp started, relaxation of the buckled plate was measured by the midspan gauges as a compressive strain. The maximum negative strain was reached when the plate was no longer buckled, and started to carry tensile loads. Obviously, the extent of buckling depended on the duration of the immersion. It can therefore be hypothesized that the duration of the immersion is the main parameter that explains the shift in the position of the curves in Figure 4.5(a). The only way to counteract this behaviour is to have the CFRP plate bonded on its entire length rather than at its ends forming two joints.

This explains the difference in the strain measurements on the CFRP plate at midspan. Other locations of interest for comparing the strain curves are along the CFRP-concrete joint. At the beginning of the joint, identified with the circles in Figures 4.3(a) and 4.5(a), the measured strains are apparently larger than those at midspan. This unexpected situation can be explained by the altered measurement corresponding to the buckled state of the plate in the unbonded portion at the initiation of the test. At 125 mm from the joint, measured strains in the beam CI are much smaller than the corresponding strains in the reference beam C1. In addition, they

remained almost constant throughout the fatigue test. This indicates that there was no significant degradation of stiffness in that part of the immersed beam.

A similar set of comparisons can be undertaken between Figures 4.5(b) and 4.3(b), for the Replark-strengthened specimens. It appears that the strain measurements on the CFRP were almost negligible before completion of the first 1000 cycles. This probably indicates that the CFRP does not contribute any stiffening to the beam until that moment. When the softening effect due to the fatigue cycles became sufficient, there was a sudden increase in strains. For instance, since there was no major cracking, Figure 4.5(b) does not exhibit the same localized effect as Figure 4.3(b). In the case of the exposed specimen RI the maximum strains were actually measured at midspan. An additional comparison between the specimens CI and RI, both of them immersed for 160 days, confirms that the CarboDur plate reinforcement contributes to the load carrying capacity of the beam as soon as it is loaded. On the other hand, it appears that a minimum level of cracking is necessary before the activation of the tensile capacity of the wet lay-up system.

There were two additional parameters of interest in this series of tests: the cyclic nature of the immersion versus the continuous immersion, and the use of saltwater instead of ordinary water. In Figure 4.6, the results for two specimens exposed to 13 wet-dry cycles in saltwater are presented. The data for the CarboDur-strengthened specimen CW-S and for the Replark-strengthened specimen RW-S are given in Figures 4.6(a) and (b), respectively. In the case of the CarboDur beams the fatigue behaviour is not altered by the variations in exposure conditions, as a comparison between Figures 4.6(a) and 4.5(a) indicates. In fact, these two beams exhibit almost identical results in fatigue. Results for beams CI-S and CW are presented in Appendix B and show similar behaviour with CW-S.

As opposed to the CarboDur series of beams, there is a large variability between the fatigue curves for the four Replark-strengthened specimens exposed to different immersion conditions. For example, Figure 4.6(b) showing the behaviour of the beam RW-S can be compared to Figure 4.5(b), presenting the response of the RI specimen. For instance, the maximum strain is not at the same location for the two beams. In addition, the rate of increase

in strain differs from one beam to the other. These two observations support our previous hypothesis that the wet lay-up system was not active at the initial stage of the test, especially with the low level of cyclic loading. Results presented in Appendix B for the other ordinary and saltwater immersed beams from series R, also confirm the above-mentioned hypothesis.

For all the beams discussed above, the maximum strains measured in the CFRP at midspan, $\varepsilon_{frp,\,fat}$, at the last cycle of the test are presented in Table 4.1. For the CarboDur-strengthened specimens, there is very little variation between the measured strains, except for one beam. In this case, it has already been pointed out that the beam exhibited a large crack near one of the point-loads at an early stage of cycling. In contrast to this generally consistent behaviour, Table 4.1 indicates that there is a wide distribution of maximum strains for the case of Replark-strengthened beams under identical loading conditions. This variability can be explained by a softening effect that depends on the distribution of cracks and their sequence of occurrence. In turn, observed crack patterns vary a lot from one beam to another. At a low level of loading, this softening effect is obviously more significant for the wet lay-up system than for the plate reinforcement.

4.2.2 Post-fatigue behaviour of beams under static loads

All the results from the static tests on the beams subjected to the combination of environmental exposures and fatigue loading are listed in Table 4.1. They are discussed in detail in the following and additional graphic results can be found in Appendix C. For CarboDur-strengthened specimens CW, CW-S, CI and CI-S, the measured ultimate load, $P_{u,exp}$ is about 10% lower than the predicted value, P_{des}. The fact that the average capacity of the specimens exposed to water was higher than that of the control specimens is probably due to improved curing conditions. The relationship between the ultimate load and deflection suggest that all beams had a similar stiffness at failure. Overall, there was no noticeable degradation caused by the exposure conditions to the CarboDur-strengthened specimens.

In addition to the above data at failure, Figure 4.7 provides information on the shear stress at the CFRP-concrete interface for the CI and CW-S beams throughout the static test. For both cases it can be observed that the first 125 mm portion of the joint exhibits higher shear stresses

than the next 100 mm-long portion, until approximately 30% of the ultimate load. As the load increases beyond that value, the shear stress in the second portion of the joint reaches higher values than the shear stress in the first portion. Because the shear stress in the second portion of the joint for beam CW-S decreases before the corresponding curve for beam CI, there is a strong indication that the wet-dry cycling produces more damage at the CFRP-concrete interface. However, these variations in the sequence of damage at the CFRP-concrete interface did not lead to significant differences in the ultimate capacity of the beams. The remaining parameter under consideration was the use of saltwater instead of ordinary water. The shear stress history along the CFRP-concrete interface was identical for beams CI and CI-S, as well as for CW and CW-S. This means that the saltwater or ordinary water produced the same results.

For the Replark-strengthened beams, the results of the static load test subsequent to the combined immersion and fatigue load are listed in Table 4.1, and the behaviour of the CFRP-concrete interface for two of them can be found in Figure 4.8. It can be observed that the beams were able to sustain an ultimate load $P_{u,exp}$ that was higher than the predicted value P_{des}. The high load at failure is associated with large deflections and large strains in the CFRP reinforcement. The ultimate load and corresponding deflection values reported in the table clearly indicate that the external reinforcement with a wet lay-up system leads to almost no increase in stiffness. These observations outline the contrast in behaviour with CFRP plate reinforcement discussed before. However, Figure 4.8 indicates that as for the CarboDur-strengthened beams, the 13 wet-dry cycles produced more damage at the CFRP-concrete interface than the 160-day immersion.

4.3 Effect of loading range: low-level versus high-level fatigue, Series II

The 15 specimens of the second series of tests are listed in Tables 4.2 and 4.3. They consist of two control beams, NA and NB, which underwent only the static tests to failure and seven beams in the L series listed in Table 4.2. The 16^{th} beam in this series was only IRM tested and carries no other instrumentation such as conventional gauges: it is consequently omitted from the table. Results for six more beams in the H series are given in Table 4.3. The beams in the L series were submitted to low-level fatigue loading, that is between 15 and 35% of M_y, and

the H series to high-level amplitude cycling with a load that oscillates from 35 to 75% of the yielding moment. All beams underwent a number of cycles from 400 000 to 2 000 000.

The next discussion will compare results obtained in these tests with the Series I tests following the same sequence of presentation as in section 4.1.

4.3.1 Low-level cycling

Seven beams from this series were submitted to a low-level of fatigue loading with three different numbers of cycles. Two of them were tested for 400 000 cycles, three for 800 000 and the remaining two for 2 000 000 cycles. Graphical results are presented in the following for a specimen tested for each different number of cycles. For the 400 000-cycle test beam L400B that shows typical results is presented. Typical results for tests with 800 000 and two million cycles are also presented for L800C and L2000B. For the case of 800 000-cycle tests, beam L800C was specifically selected because it was tested at 2 Hz. For the other load cases, results are similar for the replica beams and are presented in Appendix D.

One could recall that beam C1 of subsection 4.1.1 underwent the same cyclic loading as L400B, that is 400 000 cycles with the extreme loads from 15 to 35% of the yield moment. Thus it is natural to compare their behaviour first. This can be done by comparing Figures 4.9(a) and 4.3(a). The overall behaviour of L400B is very similar to that of C1. The gauge at midspan, represented by the curves with clear and solid rectangles, measured the maximum strain, consistently smaller values are observed for the case of L400B than for C1. However, the difference between the maximum and minimum strain in the central section of the beam remained approximately the same, that is 500 με.

Further on, the behaviour of L800C and L2000B compares very well with that of L400B, as Figure 4.9 illustrates. One difference in their behaviour can be observed at the gauge located at joint + 225 mm. The gauge readings at this location, represented graphically by the solid lines in Figure 4.9(c) for L2000B, shows that there is a slight increase in deformations by the end of the test. For the same beam L2000B, the strains at the beginning of the joint represented by the curves with circles are larger than in the case of L400 and L800, as of

Figures 4.9(a) and (b). One possible explanation for this difference is that the gauge was not probably installed exactly at the beginning of the joint but slightly towards the midspan. Consequently the readings are larger than expected and closer to the ones given by the gauge at central section.

For all the beams discussed above, the maximum strains measured in the steel, concrete and CFRP at midspan, $\varepsilon_{s,\,fat}$, $\varepsilon_{c,\,fat}$, $\varepsilon_{frp,\,fat}$, for the last cycle of the test are presented in Table 4.2 in a similar manner to Table 4.1. For all specimens there is very little variation between the strains measured at the same location. Specimens L800A and B tested at a frequency of 3 Hz, as stated above, exhibited premature yielding of the steel reinforcement. Thus, the strain values measured on the steel rebar in column three of Table 4.2 are marked to show that they are recorded just before yielding rather than at the end of the test. The concrete strains were almost constant throughout the fatigue tests for all the beams and reached the maximum value of –229 με for L800C.

4.3.2 High-level cycling

The six beams of the H series were cycled with a load oscillating from 35 to 75% of the yield moment, for different numbers of cycles, in order to understand the influence of load magnitude on their fatigue behaviour. The results from these tests are compared with those obtained for low-level fatigue loading in the previous subsection.

The increase in maximum load magnitude from 35 to 75% of M_y resulted in a significant increase in strains measured on the CFRP as well as in the steel and concrete in compression. Generally, the strain values for this load case have been doubled as compared to the low-level load case. Figure 4.9 shows these maximum strains measured at midspan to be around 1600 με for CFRP and 900 με in rebars for cycles up to 35% of M_y. These values are increasing to 3300 με and 1700 με for high-level fatigue, that is 75% of M_y, as indicated in Figure 4.10. These maximum strain values are also indicated in Table 4.3 in a similar manner to the results in Table 4.2.

A main difference between the two series of tests is that, for the H beams the CFRP plate is enhanced on its full instrumented-length. Figure 4.10(a) shows that at location joint + 225 mm strains are higher than 1100 με, that is ten times larger than in the case of L400B presented in Figure 4.9(a). This can be explained by the extensive cracking that could be observed for beams in the H series, from the early stages of loading. Approximately 8 cracks per beam were observed, mainly concentrated along the joint and in some cases they propagate through the joint leading to the degradation of the CFRP-concrete interface. Moreover, this degradation was so severe in some cases that three beams actually failed before reaching the intended end of the test. The beams that failed during the fatigue tests are marked in Table 4.3.

A comparison of strain evolutions for beams H400A, H800A and H2000B, Figure 4.10, reveals that a constant difference between maximum and minimum deformation at a given location was the same. This value is approximately 1000 με on the CFRP at midspan throughout the fatigue test, independent of the number of cycles. Steel deformation decreases with the number of cycles for H800A and H2000B whereas for H400A is constant. For the same two beams the strains at location joint + 225 mm is gradually increasing with an increasing number of cycles.

Of the six beams listed in Table 4.3, only three resisted severe cycling to the end of the testing: H400A, H800A and H2000B. Their measured results are very similar as the strains in the last cycle indicate. For H2000B, minimum and maximum concrete strains for the first cycle were –214 με and -455 με and they increased gradually to reach by the end of cycling -310 με and -553 με, as revealed in Table 4.3.

For the case of beams H400B, H800B and H2000A strains are measured at the last cycle before their premature failure at 243 000, 203 000 and 710 000 cycles. Even though strain values are recorded for these beams before reaching the proposed number of cycles they compare very well to the other values. This is due to the fact that the response of the beams stabilizes after a relatively short number of cycles and, in general, there is little variation in these strains.

4.3.3 Post-fatigue behaviour of beams under static loads

To complete the sequence of testing of the beams, they were loaded quasi-statically to failure. Results from these tests are presented in Tables 4.2 and 4.3, in a similar manner as in Table 4.1.

In general, failure occurred at a load $P_{u,exp}$ about 15% smaller than the calculated one. For the two control beams that were tested only statically, NA and NB, the values for both ultimate loads and the corresponding deflections are very close to each other. Beams in the L series exhibited similar residual capacity to the control ones but the beams in the H series show a 10% increase in ultimate capacity. This can be explained by the way the stress is distributed in the joint as a result of fatigue cycling. For high-level fatigue loaded beams, cracks were observed at the concrete-CFRP interface. Probably, this cracking enhanced the carrying capacity of the joint and thus the load resistance of the beam. As opposed to this increase in residual strength, there is a 20% decrease in deformability for the beams in the H series, as Table 4.2 confirms.

The failure mode of all the beams was by delamination, hence it would be useful to investigate the behaviour of the CFRP-concrete interface. Similar to subsection 4.1.2, the average shear stress is calculated and plotted against relative load. Figure 4.11 shows these curves obtained for the two control beams NA and NB. They show that the shear stress at the interface is mainly carried by the first interval for the initial loading phase. Then, at about one third of the ultimate load, shear stress is transferred to the second interval and reaches a maximum of about 3.4 MPa at 50% of the ultimate load for NA. This shear transfer mechanism from the first interval to the second is also observed in the case of NB.

Comparing the shear stress distribution along the joint for the control specimens NA, Figure 4.11(a), and L400B of Figure 4.12(a), one can observe that the fatigue cycling produced some damage at the CFRP-concrete interface. Though the presence of damage is probable at the first 125 mm portion of the joint, the second interval reached a relatively high maximum stress of 2.7 MPa. For the case of beam H400A, where the cycling amplitude was increased to 75% of M_y, there is a severe deterioration of the first portion of the joint that could carry only a

small fraction of the total shear stress. The curve representing the shear carried by the second portion of the joint increases almost linearly with the increasing load at a constant slope. This behaviour is new and has not been observed for the previous specimens. The same type of shear stress variation is observed in Figure 4.13(b) and 14(b), with the only difference that in these cases the same increase trend is noticed for the two joint intervals. This suggests that the concrete-CFRP interface degrades more severely in the case of the H series of beams than for the L series.

If the beams subjected to higher cyclic loads exhibited a radical change in the shear transfer mechanism at the CFRP-concrete interface, the increasing number of cycles do not appear to substantially influence it. Moreover, the maximum shear stresses seem to be inversely proportional to the amplitude of applied cyclic load. This may be due to the same reason stated above: the larger the joint degradation the smaller the shear stress at the interface. Overall, smaller shear stresses are calculated for beams in the H series than for those in the L series. However, these variations in the extent of damage and damage mechanism at the interface did not translate into a significant difference in the ultimate capacity of the beams.

4.4 Summary

For the low-level cycling of the beams in Series I the damage observed in the CFRP-strengthened beams during fatigue loading was minimal. However, the fatigue response of the CFRP layered-strengthened beam was very different from that of the plate-strengthened system. The degradation of local stiffness is faster in Replark-strengthened beams than for the plate reinforcement, apparently because of the premature cracking of the concrete. In fact, for the CarboDur strengthened beams, an even distribution of strains was observed, whereas significant local strain concentrations were measured in the case of the wet lay-up system. Because of the way cracks are generated in the two types of beams, it is understandable that the strains and stresses are easier to predict for the CarboDur reinforcement system.

For both systems, the load-carrying mechanism was equally important for the static loading as for the fatigue tests. Replark-strengthened beams exhibit a higher deformability than the CarboDur specimens. However, the failure of the Replark beams was rather sudden and brittle

due to the FRP failure in tension. The ultimate strain in the Replark reinforcement almost reached its specified ultimate elongation whereas CarboDur attained only a fraction of it. The mean shear stresses for the Replark beams seem to shift more suddenly when cracks propagate at the CFRP-concrete interface than for the stiffer CarboDur system.

As for the reference beams, the response of the water-exposed beams was dependent on the CFRP systems used for strengthening. In the case of the CarboDur plate, the shrinkage due to exposures conditions modified the shape of the external reinforcement, and a significant buckling of the unbonded portion of the CFRP plate was observed before any loading took place. That was not the case for Replark-strengthened beams where the full-length bonding of the CFRP sheets to the concrete ensured the strain compatibility at the interface between the two materials.

For low-level fatigue loading, strains and loads are immediately transferred to the CarboDur reinforcement and this ensures a consistent response of the beams, independently of the prior exposure conditions. In contrast, Replark-strengthened beams show a large variability in their fatigue response. This can be explained mostly by the conditions of application of the CFRP layers in the wet lay-up system. A comparison between results obtained for continuous immersion and the wet-dry cycles did not reveal major differences in the behaviour of the specimens.

However, the CFRP-concrete interface seems to be affected by the type of exposure when the quasi-static load is applied after the combined effects of fatigue and water exposure. This can be justified by the evolution of the shear stress at this interface. Despite the fact that there is a variety of shear transfer mechanisms at the interface, all the specimens were able to sustain the same loads at failure. Moreover, there is no evidence of stiffness degradation due to exposure for the two CFRP systems discussed. As expected, the CarboDur specimens were much stiffer than the Replark beams. Finally, the exposure to saltwater or ordinary water was not found to be a significant parameter for this first series of tests.

The Series II of the project had as parameters the amplitude of the load applied during tests and the number of fatigue cycles. In addition, the influence of fatigue loading on the residual strength of the beams could be investigated by comparing results obtained on beams that were submitted to fatigue load prior to static testing, and the reference beams that were only statically tested.

The overall stiffness decreased with an increasing number of cycles, mainly due to shear-flexural cracking and microcracking. For the low-level loading, it reached an almost constant plateau at about 100 000 cycles. The length of visible cracks from this point forward remained almost constant. Hence, it is suspected that the slight changes in stiffness continuing after this point are caused mostly by microcracking that are not visible by the naked eye.

For the high-level loading the stiffness deteriorates rapidly at the initial stages when the crack pattern is almost completely defined. It then continues to degrade as the number of cycles increases. This may be due to the fact that the cracks initiated at the CFRP-concrete interface continuously propagate to the end of the test. Actually, in three cases, cracks propagated rapidly and one beam failed as early as 203 000 cycles due to delamination of the CFRP plate. One can conclude that the bonding between the CFRP and the host structure has a crucial role in load carrying mechanisms. This is especially important when the structure is submitted to high-amplitude loading.

Though the maximum fatigue load applied for two million cycles to a strengthened beam is about 40% larger than the ultimate strength of a similar unstrengthened RC beam, the CFRP system succeeds in maintaining the integrity of the specimen. Moreover, the external reinforcement kept the strains in the steel rebars below the yielding point throughout the whole sequence of testing, thus reconfirming the benefits of CFRP for strengthening concrete beams.

Table 4.1 Water-exposed beams submitted to fatigue cycles from 15-35 % of M_y

Specimen	f'_{c-28} (MPa)	f'_c (MPa)	$\varepsilon_{s,fat}$ (με)	$\varepsilon_{frp,fat}$ (με)	P_{des} (kN)	$P_{u,exp}$ (kN)	Δ_u (mm)	$\varepsilon_{s,u}$ (με)	$\varepsilon_{frp,u}$ (με)
Unreinforced									
S0	47.3	57.9	911	-	25.7	25.7	8.8	2281	-
CaboDur-strengthened									
C1	47.3	57.9	1278	2306	71.2	64.2	6.3	4029	3492
C2	47.3	57.9	-	1130	71.2	60.1	7.3	-	4224
CW	52.4	70.1	-	1467	76.0	63.2	5.7	-	3968
CW-S	52.4	67.6	731	1410	75.1	69.2	6.6	2516	4030
CI	48.3	57.0	981	1483	70.9	67.4	6.2	2751	4034
CI-S	48.3	58.0	-	1585	71.3	67.4	6.4	-	4456
Replark-strengthened									
R1	47.3	57.9	-	159	37.0	37.5	13.1	-	9685
R2	47.3	57.9	608	194	37.0	55.7	17.5	1838	12542
RW	52.4	70.1	-	121	37.5	59.9	16.6	4948	12882
RW-S	52.4	67.6	-	827	37.4	53.1	20.9	-	8540
RI	48.3	57.0	-	892	37.0	55.7	15.4	-	12976
RI-S	48.3	58.0	928	472	37.0	55.0	15.4	3072	10369

Table 4.2 CarboDur beams fatigued from 400 000 to 2 000 000 cycles at 15-35 % of M_y

Beam	f'_c (MPa)	$\varepsilon_{s,fat}$ (με)	$\varepsilon_{c,fat}$ (με)	$\varepsilon_{frp,fat}$ (με)	P_{des} (kN)	$P_{u,exp}$ (kN)	Δ_u (mm)	$\varepsilon_{s,u}$ (με)	$\varepsilon_{c,u}$ (με)	$\varepsilon_{frp,u}$ (με)
Reference, quasi-static test only										
NA	50	-	-	-	67.5	55.6	8.00	2932	-906	4700
NB	50	-	-	-	67.5	56.7	7.54	2992	-914	5124
15-35% of M_y										
L400A	50	802	-	1401	67.5	56.6	7.74	2552	-	4018
L400B†	50	1019	-208	1678	67.5	54.7	6.74	2888	-1024	4216
L800A†	50	851*	-	1492	67.5	56.5	6.92	-	-	4306
L800B†	50	1081**	-	1504	67.5	55.0	7.42	-	-1084	3894
L800C	50	911	-229	1639	67.5	57.2	6.78	2680	-916	4040
L2000A	50	879	-	1669	67.5	58.7	6.80	2610	-	4214
L2000B	50	926	-214	1596	67.5	59.4	7.43	2602	-1042	4202

† Beams tested at 3 Hz
* Steel yielded at 461 000 and **261 000 cycles

Table 4.3 CarboDur beams fatigued from 400 000 to 2 000 000 cycles at 35-75 % of M_y

Beam	f'_c (MPa)	$\varepsilon_{s,fat}$ (με)	$\varepsilon_{c,fat}$ (με)	$\varepsilon_{frp,fat}$ (με)	P_{des} (kN)	$P_{u,exp}$ (kN)	Δ_u (mm)	$\varepsilon_{s,u}$ (με)	$\varepsilon_{c,u}$ (με)	$\varepsilon_{frp,u}$ (με)
H400A	50	1751	-677	3346	67.5	62.2	6.68	2888	-1194	4102
H400B	50	1637*	-	3034	67.5	-	-	-	-	-
H800A	50	1589	-582	3258	67.5	59.4	6.22	2594	-959	3588
H800B	50	1624**	-677	3149	67.5	-	-	-	-	-
H2000A	50	1636***	-	3260	67.5	-	-	-	-	-
H2000B	50	1724	-553	3294	67.5	62.1	7.05	3064	-990	4220
Failed at *203 000, **709 000 and ***243 000 cycles										

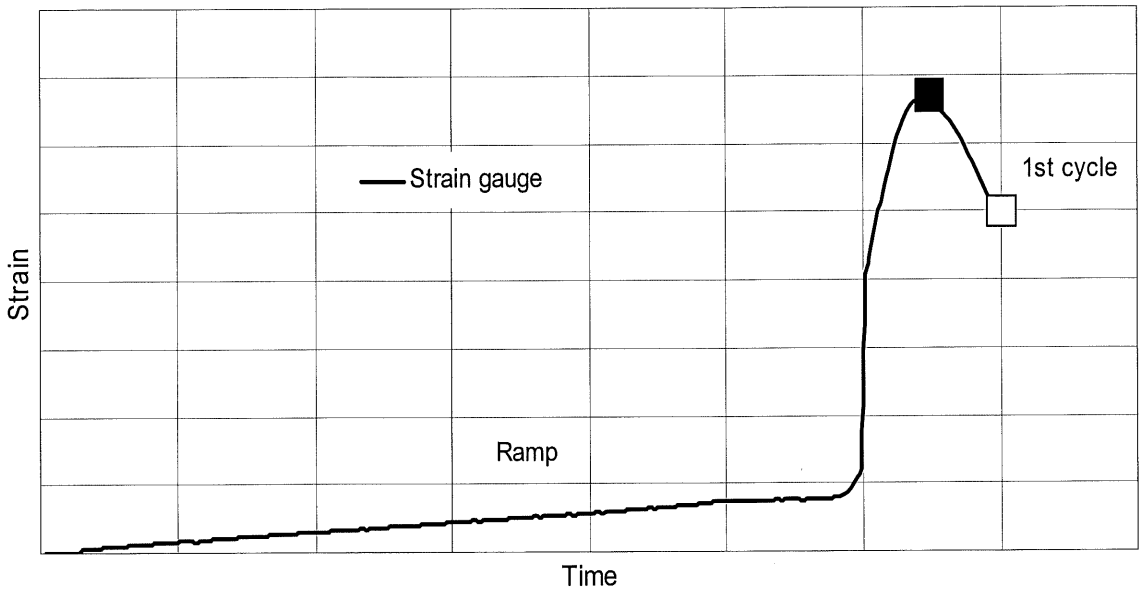

(a)

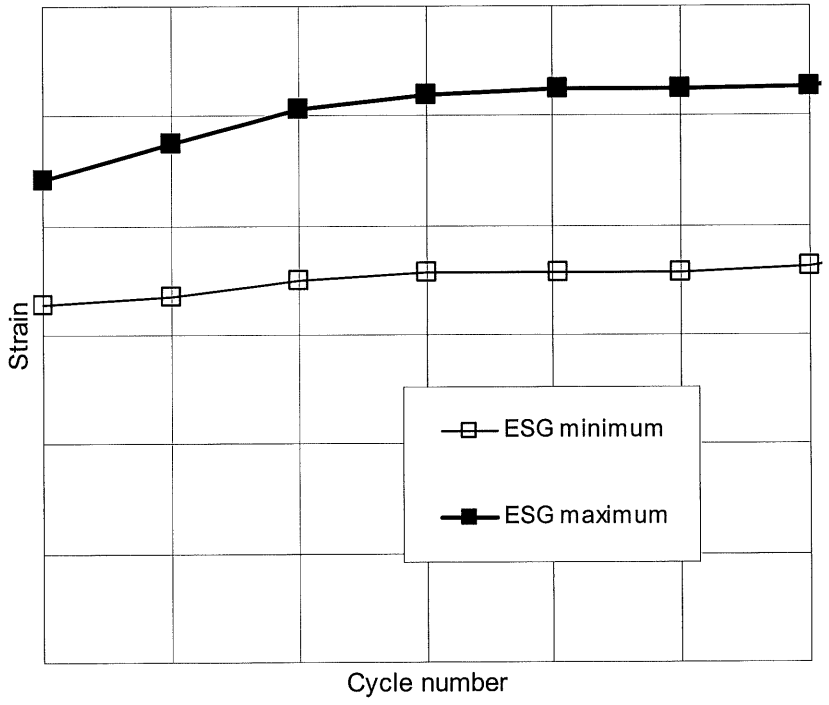

(b)

Figure 4.1 Typical strain versus cycle graph; ramp and first cycle (a), and strain extremes (b)

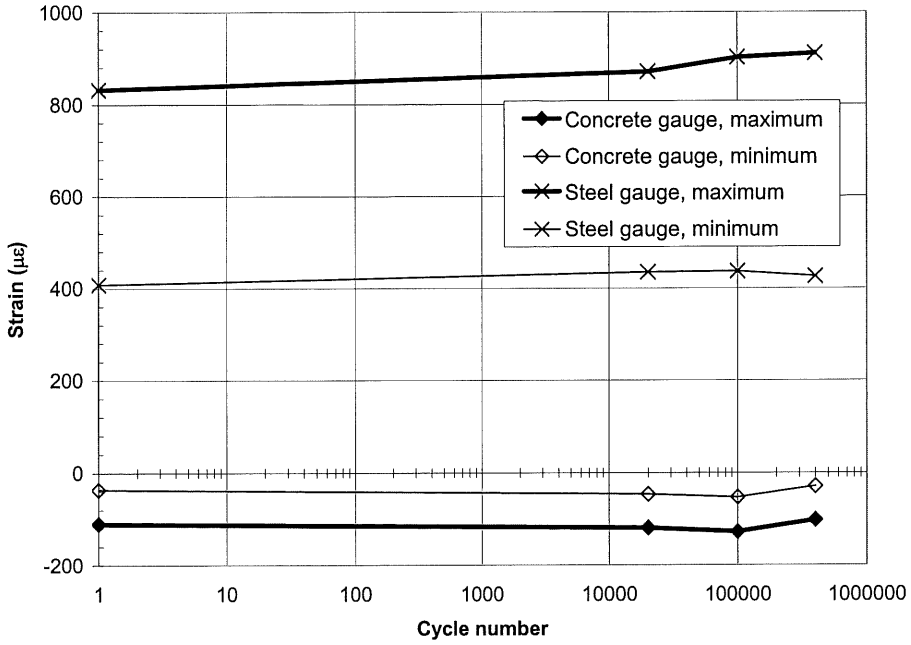

Figure 4.2 Strain extremes for reference beam S0

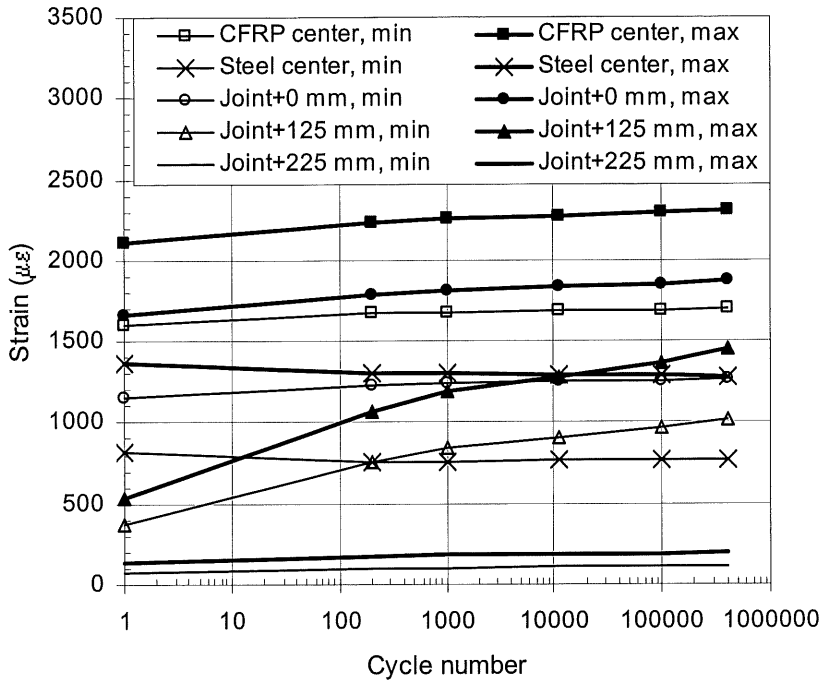

(a)

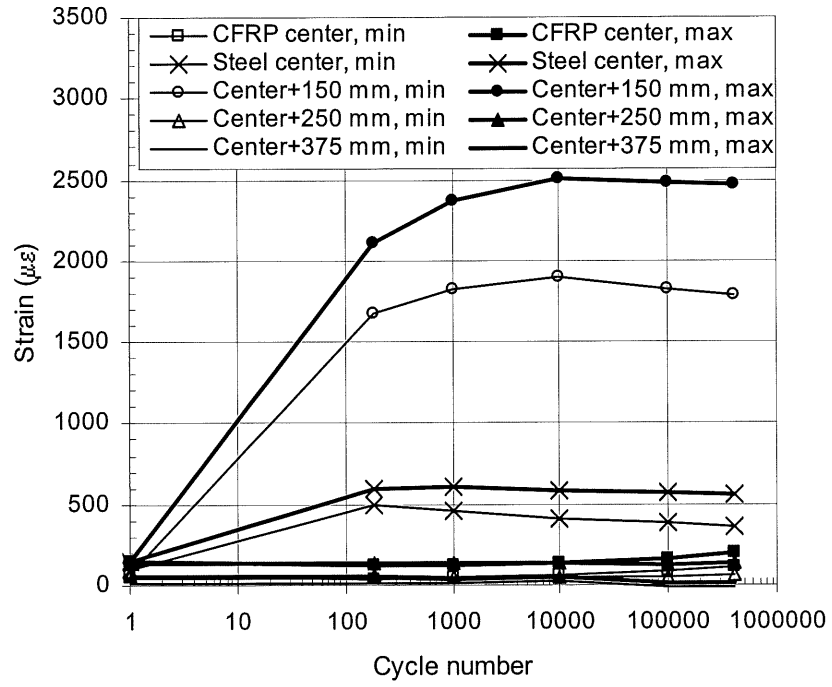

(b)

Figure 4.3 Strain extremes in steel and CFRP during fatigue test for beam C1 (a) and R2 (b)

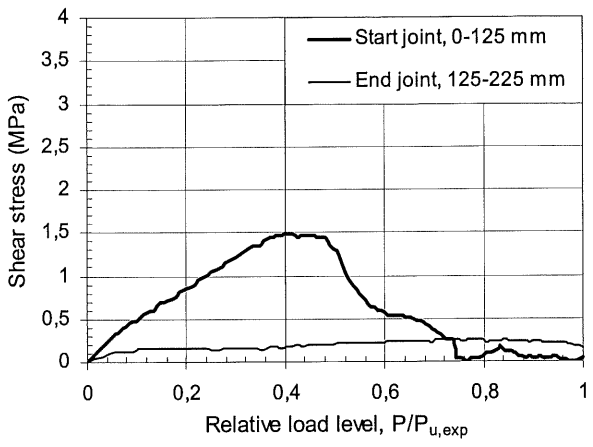

(a)

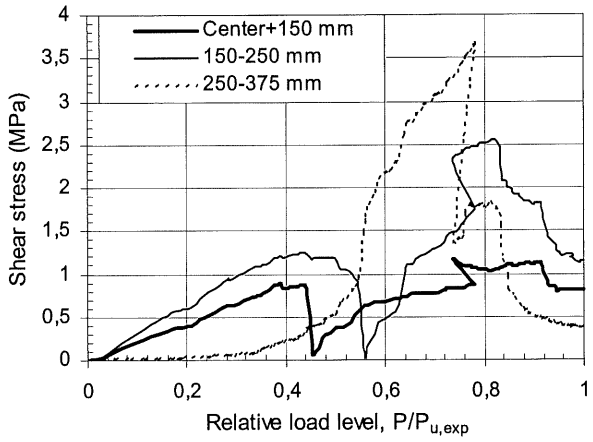

(b)

Figure 4.4 Shear stress as a function of relative load during static test for beam C1 (a) and R2 (b)

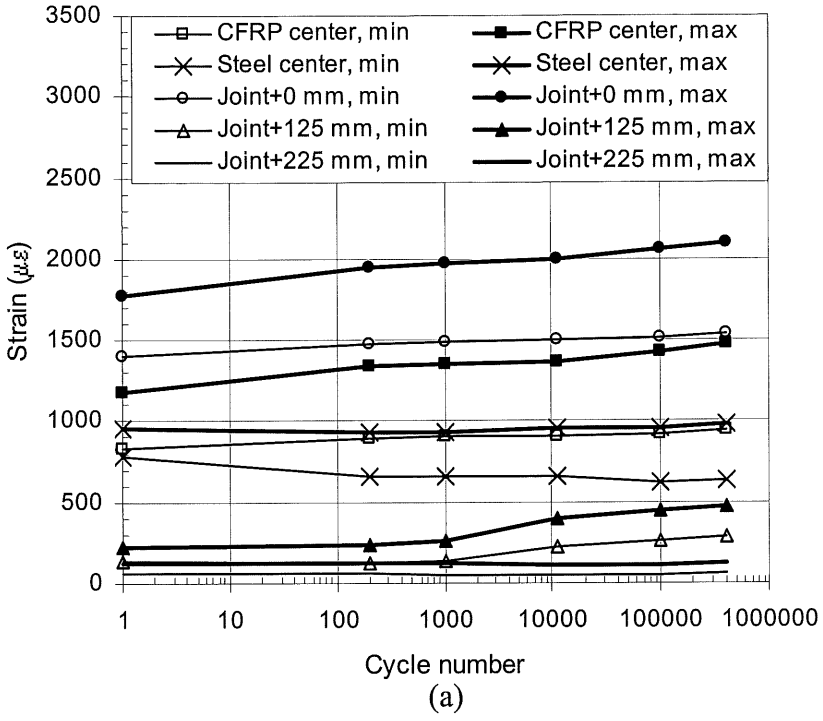

(a)

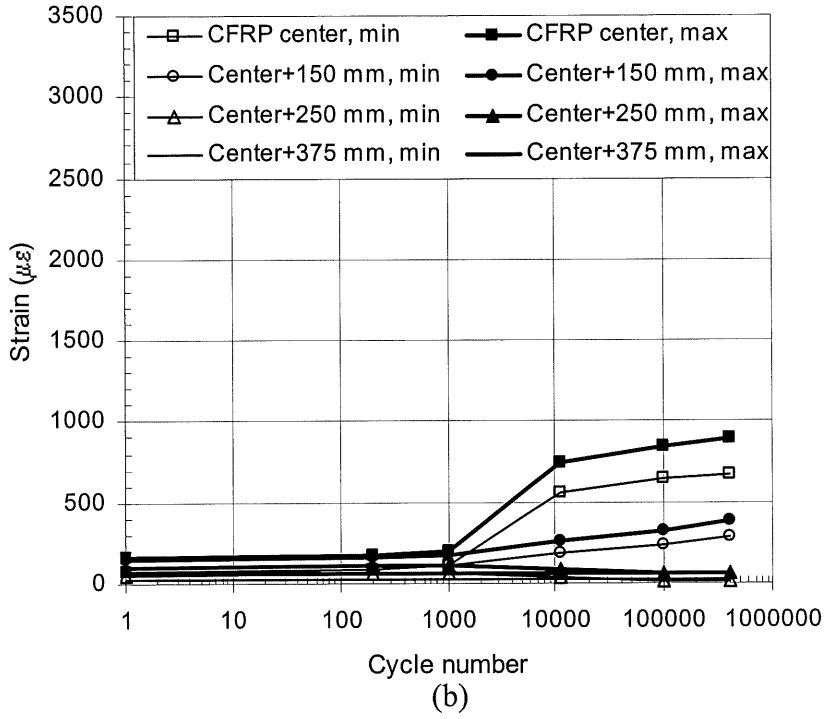

(b)

Figure 4.5 Strain extremes in steel and CFRP during fatigue test for beam CI (a) and RI (b)

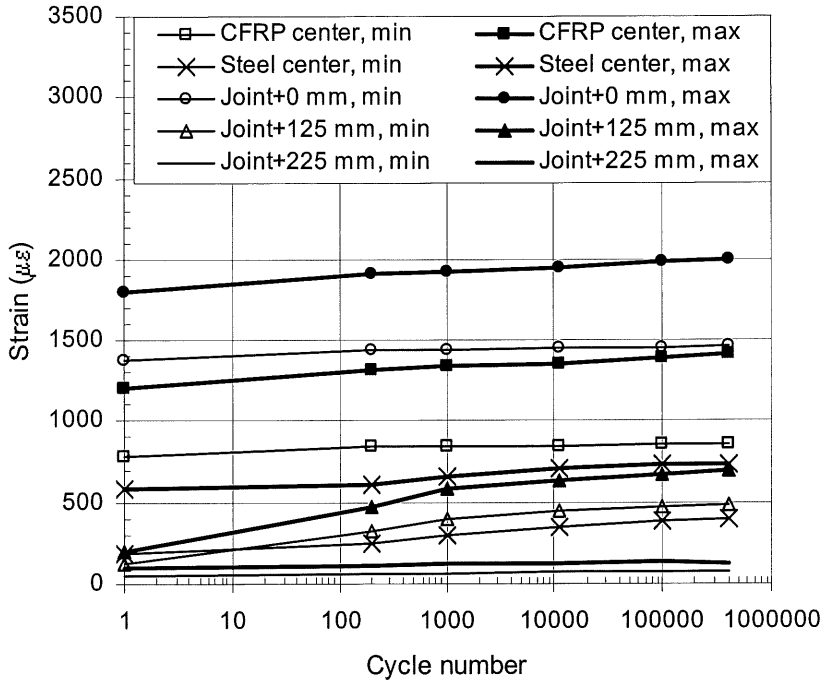

(a)

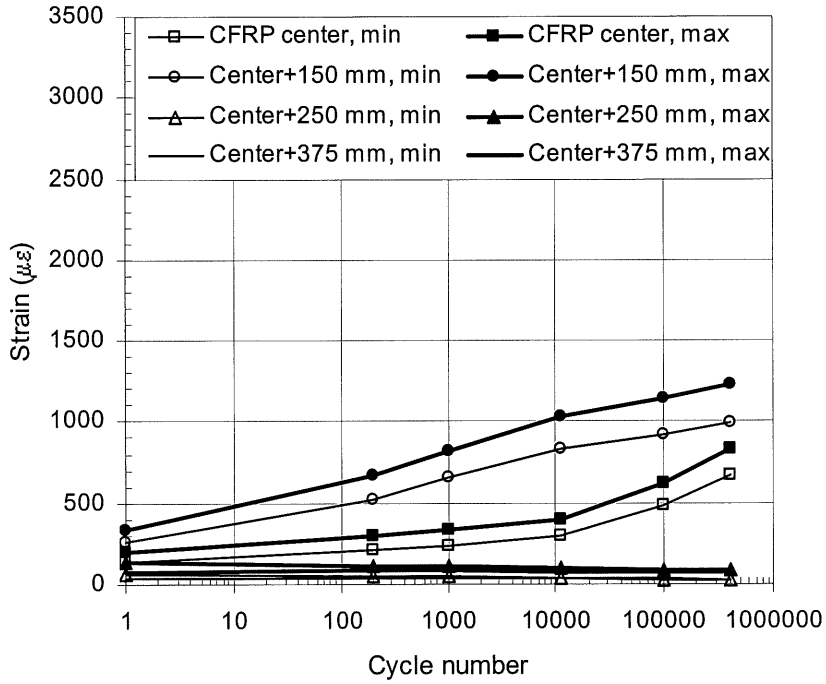

(b)

Figure 4.6 Strain extremes in steel and CFRP during fatigue test for beam CW-S (a) and RW-S (b)

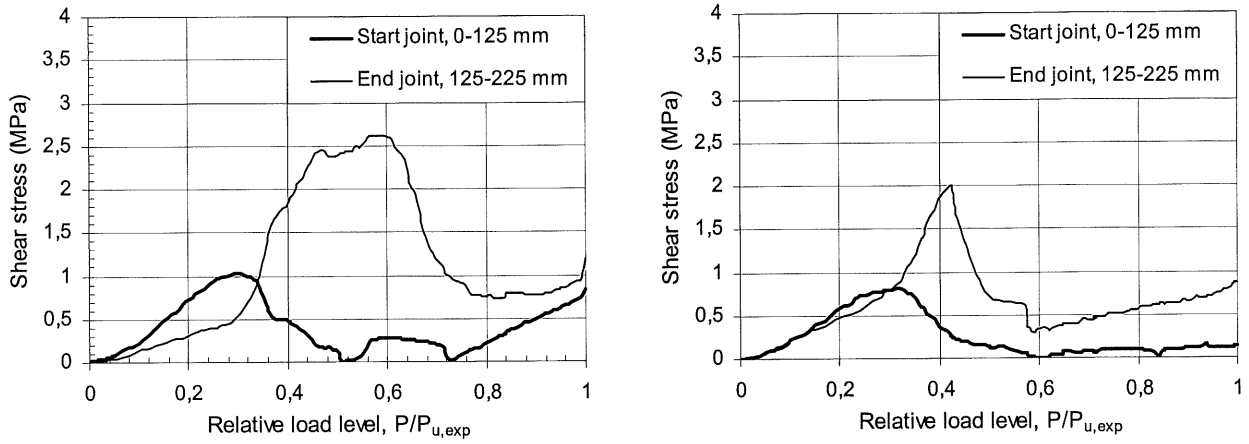

Figure 4.7 Shear stress as a function of relative load during static test for beams CI (a) and CW-S (b)

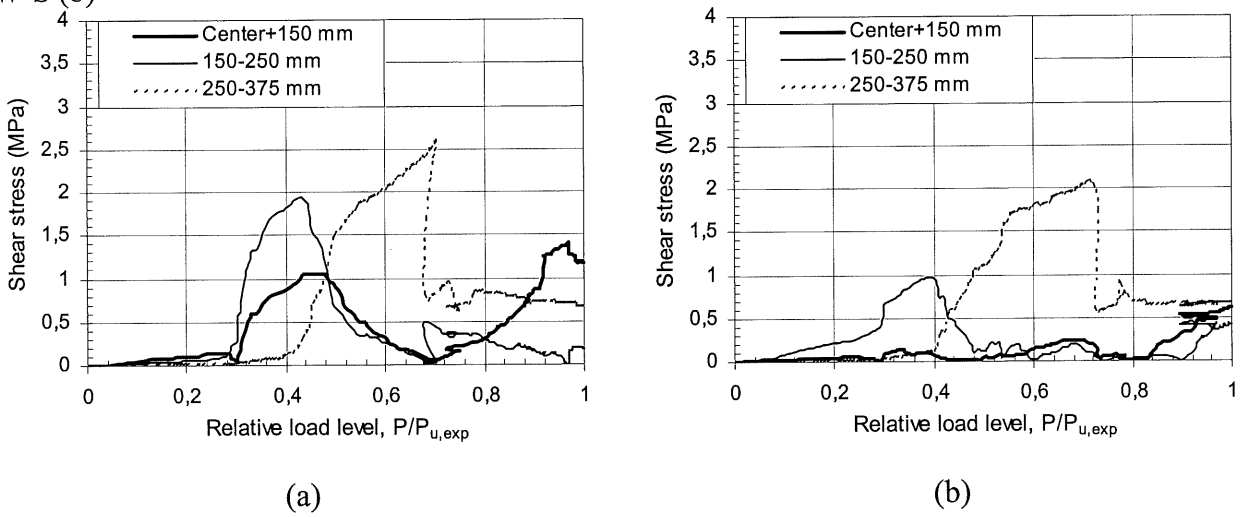

Figure 4.8 Shear stress as a function of relative load during static test for beams RI (a) and RW-S (b)

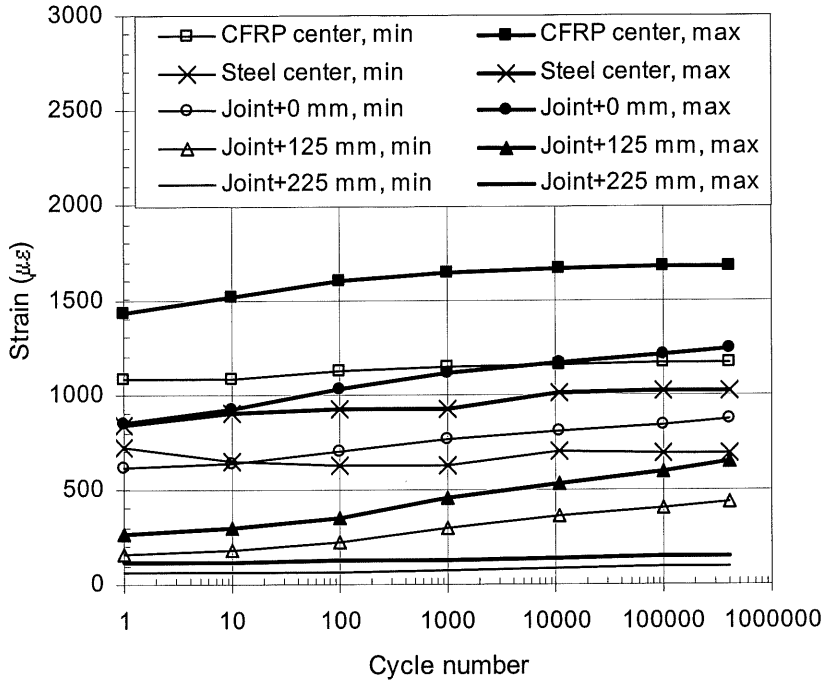

(a)

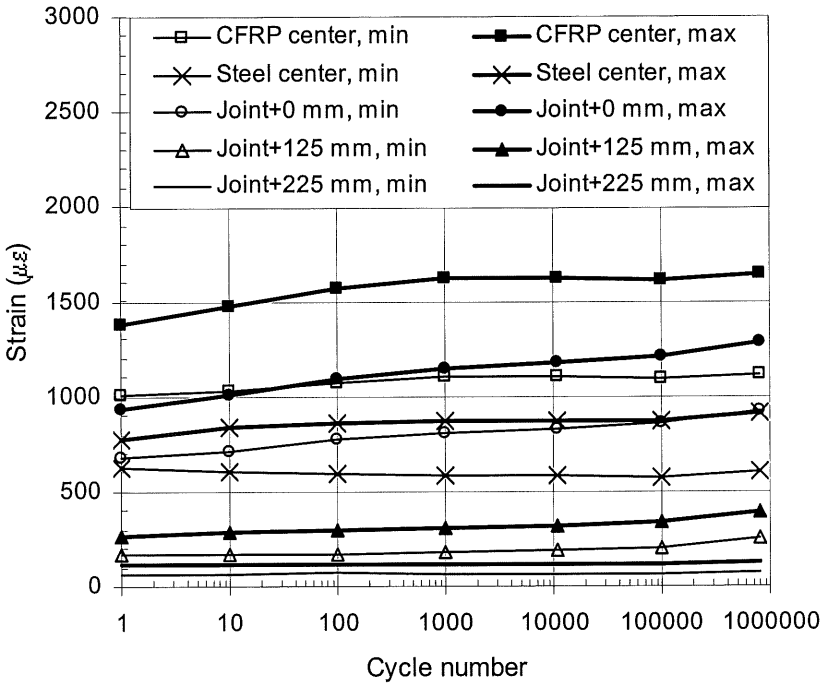

(b)

Figure 4.9 Strain extremes in steel and CFRP during fatigue test for beam L400B (a) and L800C (b)

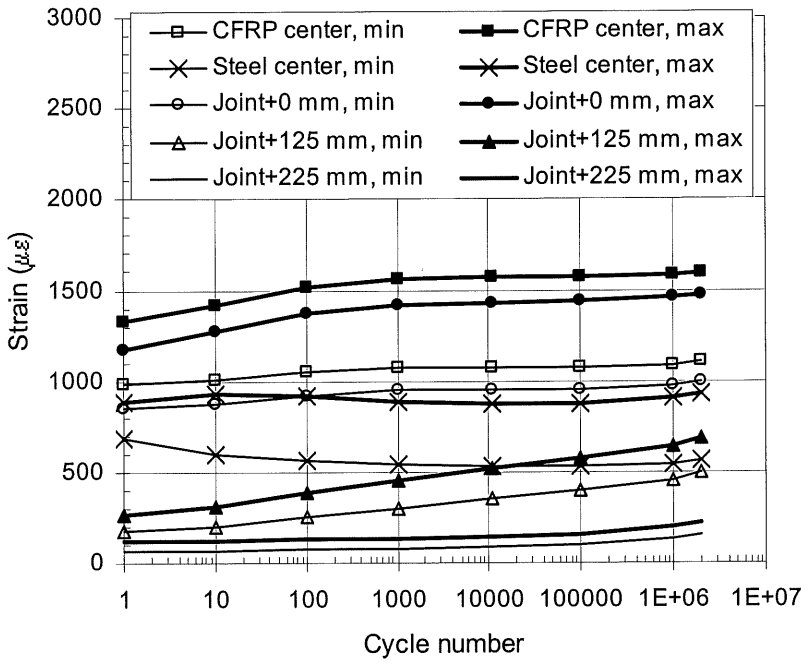

(c)

Figure 4.9 Strain extremes in steel and CFRP during fatigue test for beam L2000B (c)

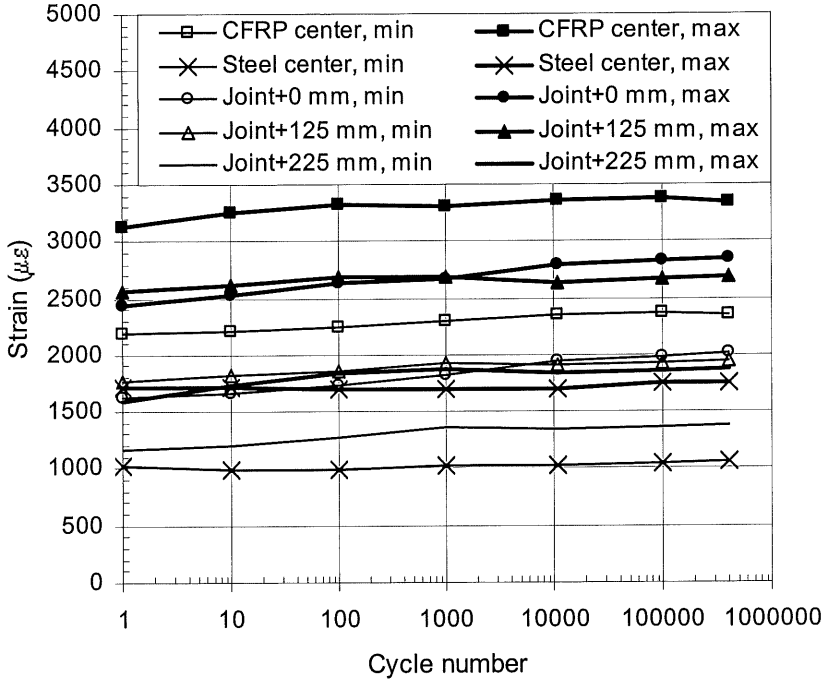

(a)

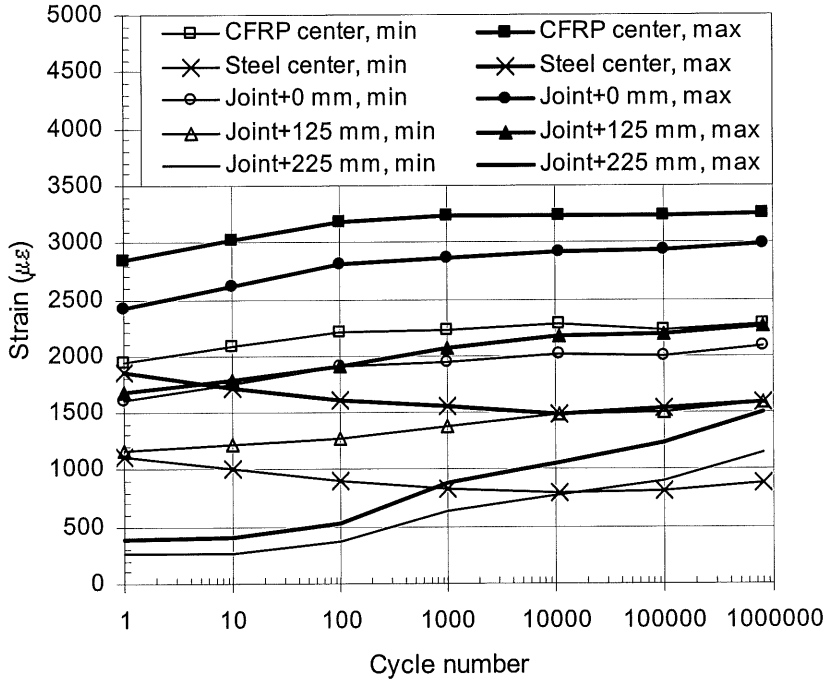

(b)

Figure 4.10 Strain extremes in steel and CFRP during fatigue test for beam H400A (a) and H800A (b)

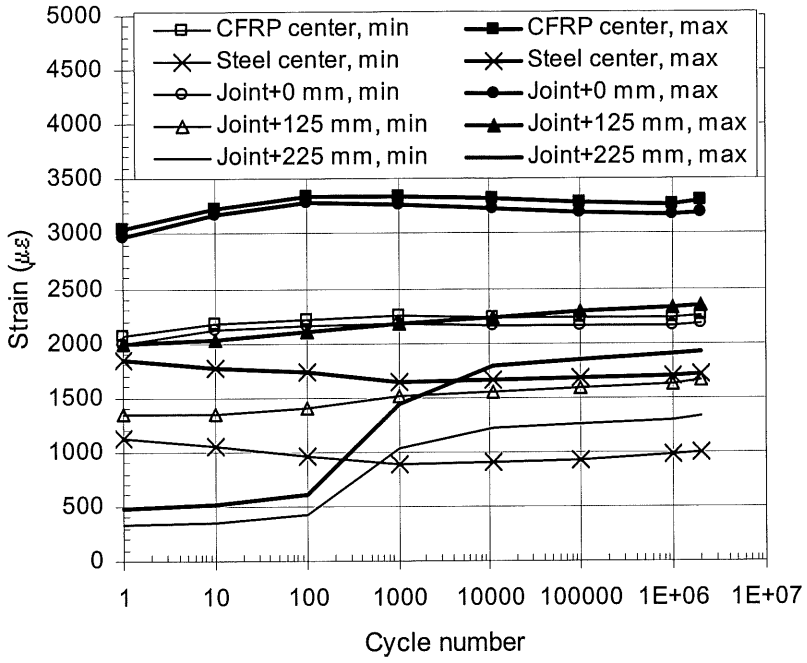

(c)

Figure 4.10 Strain extremes in steel and CFRP during fatigue test for beam H2000B (c)

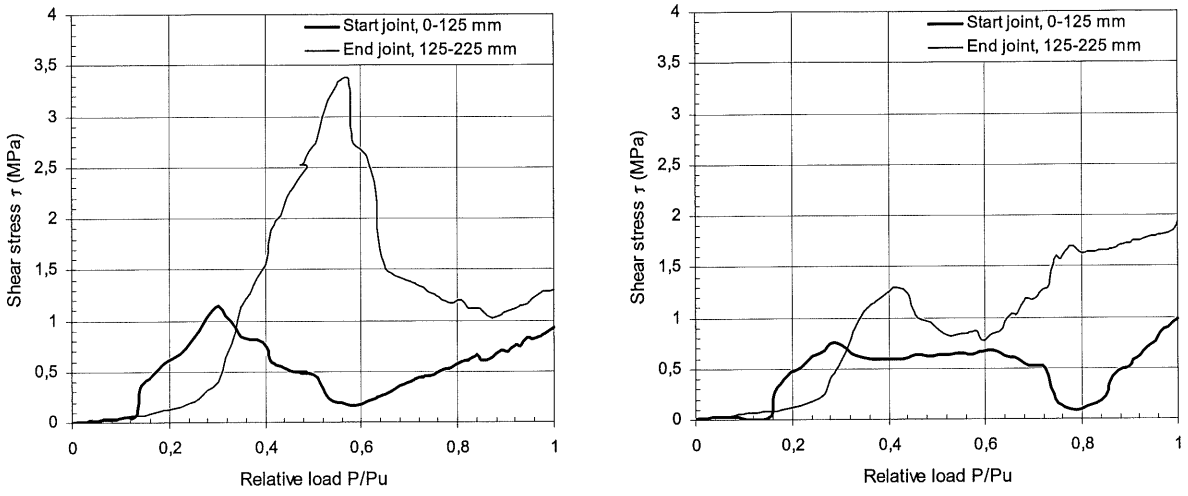

Figure 4.11 Shear stress as a function of relative load during static test for beams NA (a) and NB (b)

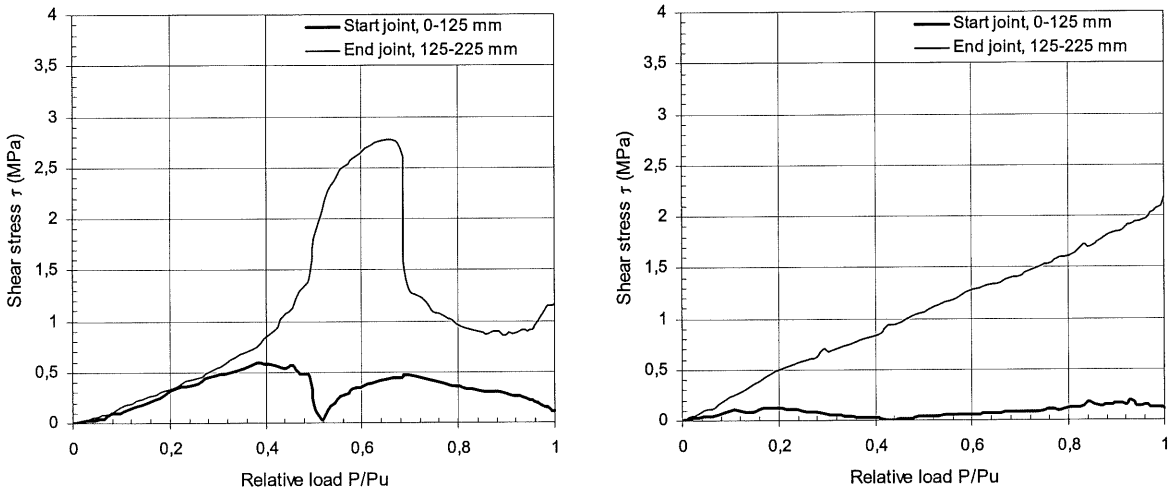

Figure 4.12 Shear stress as a function of relative load during static test for beams L400B (a) and H400A (b)

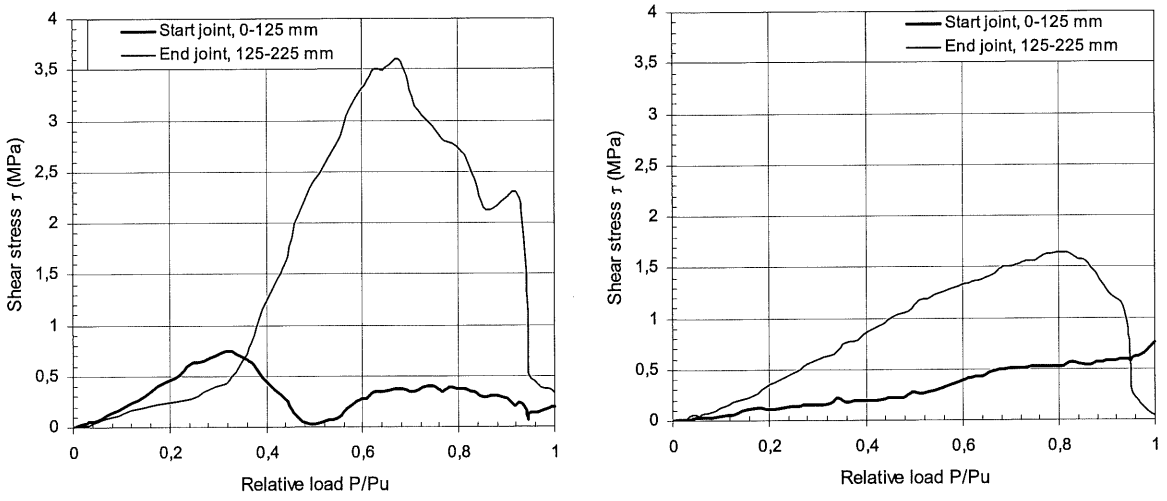

Figure 4.13 Shear stress as a function of relative load during static test for beams L800C (a) and H800A (b)

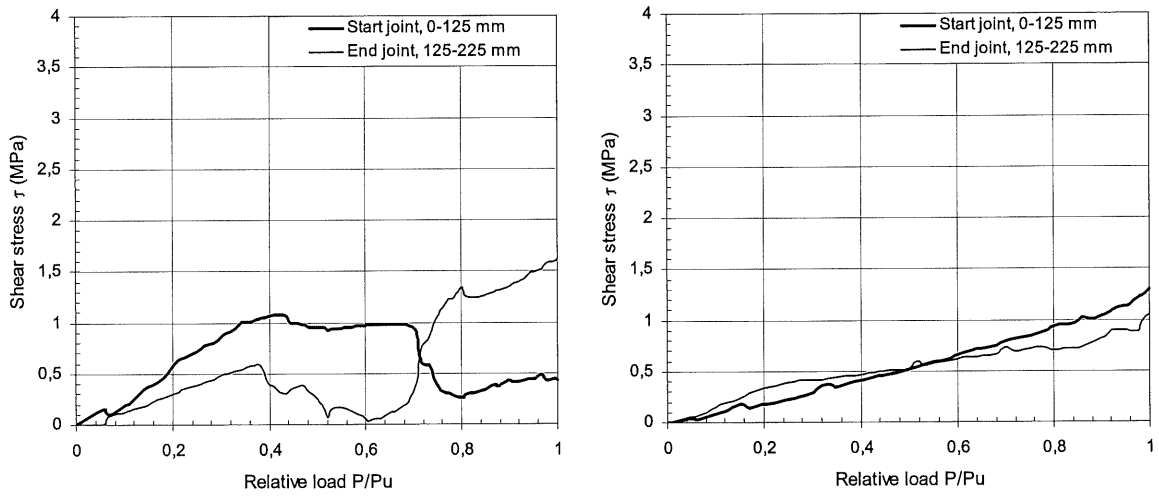

Figure 4.14 Shear stress as a function of relative load during static test for beams L2000B (a) and H2000B (b)

5 DURABILITY OF FOS

5. DURABILITY OF FABRY-PEROT FOS SENSORS

The beams presented in chapter 3 were instrumented with conventional gauges and FOS. Chapter 4 presented results given by the conventional gauges. In this chapter, these results are compared with strain readings obtained by means of FOS.

The content of this chapter is as follows. Section 5.2 presents FOS results obtained from two reference beams that were loaded directly to failure in quasi-static loading conditions. Load-strain curves and compiled tabular data will be used for a detailed discussion on the behaviour of these specimens. In section 5.3, the FOS results recorded during the fatigue testing of all 25 beams are introduced. The sensors are strained for a number of up to two million cycles with two different load amplitudes; the low-level cycling results for seven of these beams are given first, then the high-level cycling results for six beams are presented. Section 5.3 concludes with a discussion on the water exposure effects on the FOS readings of the twelve remaining beams. Section 5.4 presents FOS results obtained from the final quasi-static failure tests that were performed on all the beams that were first tested cyclically. For instance, the same FOS was thus tried in both fatigue and static loading tests, with or without water immersion. A summary of the most important findings in this chapter is presented in the concluding section.

5.1 Introduction

This chapter investigates the reliability of fibre optic sensor systems submitted to a variety of exposures, cyclic and post-cyclic loading conditions. The fibre optic sensors installed on the 27 CarboDur- and six Replark-strengthened beams presented in the previous chapter have therefore been submitted to the same loading and water exposure conditions as the beam specimens. This comprises fatigue tests with two cyclic ranges having three different numbers of cycles to a maximum of two million. Two sensors were installed on each of the beams immersed in water. The first one was installed before water exposure and the other one afterwards, in order to study the influence of the immersion on the sensor system. All the strains that are discussed in this chapter are recorded on the CFRP plate at midspan. Strain measurements from the fibre optic sensors (FOS) are compared with those obtained by electrical strain gauges (ESG) collocated. Since ESG instrumentation is a well established

technique, their readings will be used as a reliable basis for comparison with the strains given by FOS. The ESG strain will therefore be used as the reference value. Theoretical values for ultimate strains cannot be used as a reference because the assumed failure mode used in the ISIS equations do not correspond to the failure mode for which the beams were designed. Since the emphasis was placed on the CFRP-concrete interface, the specimens were designed to fail by delamination.

5.2 Reference specimens

Two specimens are herein referred to as reference beams, identified as NA and NB. They are both instrumented with one fibre optic sensor in addition to the conventional gauges. These two beams were tested under only quasi-static loading to failure. In 5.2.1, the FOS results from these tests are presented as load-deformation curves. Following a presentation of typical curves, some characteristic data from these curves will be compiled in table format for the purpose of discussion and interpretation of the strain measurements. In addition, some aspects of the stress transfer at the FOS-CFRP interface will be discussed in 5.2.2.

5.2.1 Static failure strains

Figure 5.1 presents the load-deformation responses of the beams NA and NB, as recorded by a FOS and an ESG. Thus, each figure shows two curves corresponding to the two systems used simultaneously for measuring strains. It can be observed that the load-strain measurements obtained by the two systems are very similar on each figure. As the applied load increases, its relationship to the strain remains linear until about 10 kN. At this point a short load plateau is observed, after which the load-strain curve exhibits a new linear relationship, with reduced stiffness until failure. The FOS recorded the behaviour of the CFRP-strengthened RC beam to be exactly as that measured with ESG.

For instance, for the beam NA shown in Figure 5.1(a), the first slope to a load of about 8 kN is constant. At this point the CFRP-strengthened beam cracks and there is a plateau that reaches almost 600 με. Following the plateau there is a second slope where strains continue to increase linearly up to failure at about 4600 με. The small drop in the applied load at about 27 kN that was measured by the ESG was also captured by the FOS. This corresponds to the

situation when a large vertical crack appeared above the joint, initiating some slipping of the plate at the CFRP-concrete interface. Actually, a similar RC beam without external CFRP reinforcement would have failed at about that load, and it was not unexpected to observe a discontinuity at this point. It is important to point out that Figure 5.1(a) clearly shows that the FOS strain readings agree very well with those measured by the ESG.

The specimen NB, shown in Figure 5.1(b), gives results similar to those obtained for NA. Starting from 1500 με, the slope of the FOS curve differs slightly from that of the ESG. This slight difference was observed in previous studies and did not exceed the 15% limit for static strains of about 1000 με (Rochette, 2001). This error differs from case to case. For instance, in the case of NA, almost perfect correlation is observed. This is not the case for specimen NB, where a slightly different slope is observed for FOS. When this beam is approaching failure, at about 48.7 kN there is a sudden decrease in the FOS strain readings. This drop indicates an abrupt decrease of strains by about 220 με. One can advance several hypotheses to explain this peculiar behaviour. Among them are: the possible degradation of the FOS-CFRP bond and subsequent slipping of the fibre sensor, or various damages that can be located at the optical fibre, capillary tube and fusion spots.

Twice during the NB test, the FOS readings gave some strain values out of range. These values are withdrawn from the graph. Consequently, the FOS curve has two gaps at load values of 27 and 35 kN. These abnormal values were seldom observed during other tests and each time the erroneous values are withdrawn from the curves. As the FOS continues to give reliable results afterwards, it can be assumed that the abnormal values are a result of noise in the system.

The strain data as recorded by the FOS and the ESG are listed in columns 6 and 7 of Table 5.1. Column 6 represents the strain values recorded at the moment when the FOS failed, rather than the strains at the end of the quasi-static test. In column 7, the corresponding strains measured by the ESG are listed. Column 9 in the table lists the load P measured at failure of the FOS sensor. For instance, for the reference beam NA, the FOS gave reliable readings to the very end of the test and the strains presented in Table 5.1 are those corresponding to the

ultimate load of the beam. When a drop or sudden change is observed in the FOS readings, as is indicated in Figure 5.1(b) for the beam NB, the last strain value before this event is presented. Though the beam NB failed at a load of 56.7 kN, its fibre optic sensor could measure precisely strain up to a load of 48.7 kN, when there was a sudden change in FOS measurements, as discussed above and illustrated in Figure 5.1(b). Theoretical values for the ultimate strains cannot be calculated according to the ISIS Canada (2001b) manual. The assumed failure mode in these equations is concrete crushing, whereas the specimens were designed to fail by delamination of the plate. This failure mode was selected in order to monitor the CFRP-concrete interface.

Statistical data in the form of the error between the ESG and FOS readings are given in column 8 of Table 5.1. They represent the percent by which the FOS strain value differs from the ESG measurement. Thus, one assumes that the ESG gives a reference strain signal. For instance, the difference between the two readings given by the ESG and FOS for the case of NA is 55 με. This translates into a 1.17 deviation from the reference ESG value of 4700 με. In the case of NB this value is 3.28%. Taking into account the experimental errors and the fact that the sensor and the gauge were not placed at exactly the same location, these errors are negligible.

5.2.2 Bond between FOS and CFRP plate

As discussed above, the FOS strain curve for specimen NB in Figure 5.1(b) presents a drop of about 220 με at the strain of 4000 με. It will be shown later that a similar behaviour was observed for several other sensors presented in the chapter, mainly during the quasi-static tests. It is hypothesized that a main factor leading to this unexpected change in strain readings of the sensor is the degradation of the bond between the FOS extremity and the CFRP plate. This in turn can be caused by either a degradation of the adhesive or by an insufficient FOS anchorage length at its extremity. In order to explain this, the geometry and specification of the FOS are first recalled.

The extrinsic Fabry-Perot sensor for measuring strains is portrayed in Figure 2.4. The sensor itself consists of two mirrors placed on the tips of two optical fibres spot fused into a capillary.

The air gap between the mirrors and the distance separating the fuse spots dictate the gauge operating range and sensitivity (Choquet et al. 2000). For this study, sensors having two operating ranges have been used. Sensors installed on beams NA and NB in Series II were supposed to give reliable strain readings from -1000 με to +5000 με.

There are some other factors that can affect the performance of the sensor such as precision and the operating range, the installation of the sensor, and the geometry and mechanical properties of the capillary. For instance, a bad choice of adhesive could compromise the readings as slippage may prematurely occur. The adhesive used to install most of the sensors on NA and NB is the M-Bond AE-10 and exhibits an elongation capability of up to 10%.

M-Bond AE-10 is an epoxy resin adhesive available in a two-component package including the epoxy resin and the hardener. It purportedly offers outstanding fatigue behaviour. The same epoxy-based adhesive has been used to install the conventional gauges that performed outstandingly in both static and dynamic load conditions with strain values up to 10 000 με (Gheorghiu et al. 2003). Consequently, the adhesive used for the installation of the fibre optic sensors can be eliminated as a likely cause for the potential malfunctioning of the FOS.

The insufficient anchorage or bond length of the sensor could also unexpectedly influence the readings. For instance, it is known that conventional strain gauges with a length less than 3 mm tend to exhibit reduced performance in terms of the maximum allowable elongation, stability under static strain and endurance when subjected to cyclic changing strain (ISIS Canada, 2001a). One main reason for this would be the insufficient bond surface between the gauge and the host material. It is expected that these past experiences with conventional gauges would help in clarifying some of the limitations and practical aspects of FOS.

A good bonding between the sensor and the host material is assured by a sufficient bond surface. It would be useful to illustrate this by comparing the bonding surface of the gauge and fibre optic sensor. The bonding surface of an ordinary electrical gauge 14*6 mm used in this study is plane and measures 84 mm^2. If we consider that half of this surface is tensioned in one direction and the other half in the opposite direction, then one obtains 42 mm^2 that can be

considered as the strain transfer surface. The capillary of a Fabry-Perot sensor used in these tests is 8.5 mm in length and has a diameter of 0.2 mm. If one considers as for the ESG, half of the capillary, an equivalent surface of about 4 mm^2 is found, that is ten times smaller than that of the ESG.

The small bond surface of the FOS together with its morphology may seriously affect performance such as operating range. In order to improve this, the extremity of the fibre, from the Fabry-Perot cavity to the end of the fibre, should be much larger than it currently is. Thus, the actual 8.5 mm capillary length should be increased to about 85 mm, to give an equivalent contact surface as for the conventional gauge. This length may be prohibited by many applications, in that case the morphology of the capillary surface may be improved to increase bond. Alternatively, special bonding substances and techniques may be employed to improve the strain transfer from the structure to the sensor.

This presumed insufficient FOS anchorage length did not affect the performance of the sensors, for the above-discussed NA and NB beams, when static strains were below 4000 με. It will be shown in the following sections that this limit is lowered for the case of beams tested in fatigue prior to the quasi-static testing.

5.3 Fatigue tests

This section contains a discussion and an analysis of the results obtained for the 25 beams tested in fatigue with different water exposure and loading conditions. In 5.3.1 are presented the specimens that were tested with low-level cycling, that is 15-35 % of the yielding moment, and different number of cycles. In 5.3.2, the beams loaded with three different number of cycles at high-level fatigue load, having amplitudes between 35 and 75% of the yielding moment, are discussed. Some beams were exposed to water prior to the fatigue tests and their results are presented in subsection 5.3.3.

5.3.1 Low-level cyclic load

In this subsection, results obtained on seven L-beams in Series II, externally strengthened by CarboDur plates and listed in the first column of Table 5.1, are discussed. These beams were

loaded with cycles of same low-level amplitude, given in Table 3.6 for three different number of cycles: 400 000, 800 000 and 2 000 000 cycles. To illustrate the discussion, the beam L2000B submitted to two millions cycles, that gave representative results for the tests in this subsection, is selected.

Initially, all the specimens were loaded quasi-statically up to the minimum level of the fatigue loading before starting the application of the fatigue cycling. The initial strain data for the beam L2000B, showing the ramp loading followed by the first cycle, is presented in Figure 5.2. This figure shows two curves corresponding to the readings given by the collocated ESG and FOS. It can be observed that the FOS-measured strains followed closely the ESG measurements through this sequence of initial loading, although there is a slight time lag between the two curves. This time lag was found to be caused by the sampling rate of the reading unit that was not adequately set to read dynamic strain data. These settings have been corrected during this test and the next graphical results presented show no time lag between the two strain curves.

Figure 5.3 shows the variation of strains with time for two additional cycles, one after one million and the other after two million, throughout the testing of L2000B. It must be noted that, for these cycles only, the frequency of the test was decreased from 2 to 0.05 Hz, to allow reading data for the entire cycle. A slow cycle of 50 readings took about 20 seconds whereas a regular cycle was of 0.5 seconds in duration. For the two cycles shown in the figure, a good correlation is once again observed between FOS and ESG readings. By taking the minimum and maximum strains for each cycle, such as the ones shown in Figures 5.2 and 5.3, and by plotting them against the number of cycles, an "envelope" of the strain, such as in Figure 5.4, can will be obtained.

Figure 5.4 shows two sets of curves indicating the measured strain range at midspan, as recorded by the FOS and ESG. Each sensor is represented by two curves corresponding to the minimum and maximum cyclic loads. For the ESG, the curve with white rectangles shows the minimum strains, and the one with black rectangles indicates the maximum strains through the two-million cycles. For the first cycle, the extreme values were 980 με and 1324 με. At the

same time, Figure 5.4 shows that the strains at the same location recorded by the FOS ranged from 1027 με to 1303 με. As the number of cycles increased, these extreme strains were found to change gradually. For the ESG, they increased to values comprised between 1107 με and 1596 με, while for the FOS they increased to 1121 and 1641 με. The good correlation between ESG and FOS readings proves that the FOS is able of recording the strains precisely through the two-million cycles.

A similar set of graphs was produced for the other L-beams and can be found in the Appendix D. These minimum and maximum strain values at the last cycle for all the L-beams are also listed in Table 5.1. The comparison of the minimum strain values measured by the FOS and ESG in columns 2 and 3 of the table shows a very good correlation. Likewise, the comparison of the maximum FOS and ESG strain values presented in columns 4 and 5 confirms this agreement. The difference between the minimum FOS and ESG strains varies from 0 με for L800C and 59 με for L800A. The maximum strains measured by the two systems for all the beams differ by 10 to 64 με. Taking into account the fact that strain values as high as 1600 με are measured, this difference of 64 με in FOS and ESG readings is 4%. For the same load amplitude, the number of fatigue cycles seems to have no influence on the FOS readings.

Strain calculations according to the ISIS Canada (2001b) equations indicate that the strain values varying between 500 με and 1250 με for the low-level cycling from 15 to 35% of the yielding moment should be obtained. They are clearly smaller than the measured values.

5.3.2 High-level cyclic load

The FOS system was tested to higher fatigue load levels than before on the specimens of Series II. The H-beams were strengthened with a CarboDur plate, as described in 5.3.1. Previous tests, presented in section 5.3.1, proved the capability of FOS to measure strains up to 1700 με under low-level cycling. The tests presented here consist of cycling that will cause deformations on FOS of about 3500 με.

From the six tested H-beams, three reached the end of the anticipated fatigue loading. These are the beam H400A submitted to 400 000 cycles, H800A to 800 000 cycles and H2000B that underwent two million cycles. The other three replica beams failed before reaching the end of the test. The beam H2000B, that was loaded for two-million cycles with cycling amplitudes of 35 to 75 % of M_y, was selected for the following discussion. This beam resisted the most severe cyclic loading in the present study; it gave results that are typical of the behaviour of the other two beams that successfully completed the high-level fatigue test.

For H2000B, a set of curves similar to the one presented in 5.3.1 was produced. The initial loading, comprising the ramp and the first cycle, are shown in Figure 5.5. In this case, the ramp loading was large enough to cause cracking of the beam. This happened at about 80 seconds, and a step in the initial strain slope can be observed in Figure 5.5. Then the beam exhibits a second slope up to about 160 seconds. It is followed by a plateau when the strain reached 1300 με, then the cycling began. It can be observed that the FOS strains are almost identical to the ESG ones for the entire ramp loading as well for the first fatigue cycle.

Two more cycles for the fatigue tests are portrayed in Figure 5.6. These results show again that FOS readings are in good agreement with ESG, after either one million or two million cycles. The evolution of minimum and maximum strains for the two-million cycles is presented in Figure 5.7. It is important to notice the perfect correlation between FOS and ESG measurements.

The minimum and maximum strains, as measured by the FOS and ESG for the last fatigue cycle, are listed in Table 5.1 for all H-beams that completed the proposed fatigue test. The comparison of the minimum and maximum strain values measured by the two systems shows a very good correlation. The three beams H400B, H800B, H2000A failed at 243 000, 203 000 and 709 000 cycles, respectively. The FOS readings given in the table are from the last recorded cycle and show a very good agreement with ESG readings. Although the support beam failed prematurely, the FOS system succeeded to measure strain precisely until the very last cycle. The additional results for the other H-beams, presented in Appendix D, confirm the excellent FOS ESG agreement. These results demonstrate that the FOS system could measure

strains precisely up to 3500 με under fatigue loading with high-level load amplitudes. Moreover, there was no adverse effect on FOS due to fatigue, provided that there were less than two-million cycles.

5.3.3 Water exposure

Twelve beams loaded for 400 000 cycles of low-level amplitude are presented in this section. Eight of these beams were immersed in water, while the four other beams were tested in fatigue without any water exposure. All the beams are listed in Table 5.2. The beams C1, C2, R1 and R2 were fatigue tested without any prior water exposure in order to have a reference response for the beams. The other eight specimens were immersed in water to further test the capability of these sensors to an aggressive environment. In order to do so, one FOS per beam, called FOS-A, was installed. The specimens thus instrumented underwent water exposures that consisted of wet-dry cycles or continuous immersion in either ordinary or saltwater. Another FOS, called FOS-B, was installed on the specimen following these ageing conditions in order to understand the water immersion effect on the FOS systems.

A comparison of the readings given by these FOS and by the strain gauges is presented here for all the beams. From the 12 specimens a detailed discussion is provided for four specimens, that is, for two beams for each type of external reinforcement. The results obtained for the reference beams C2 and R2 are presented first; this is followed by a discussion on the results obtained for the water-immersed beams CW-S and RW-S.

Minimum and maximum strains recorded by FOS and ESG during the fatigue test of beam C2 are illustrated in Figure 5.8. Since these reference beams were not immersed in water, only one FOS was installed on the beam, and is identified as FOS-A. The figure shows that from the first cycle the FOS failed to measure correctly the strains. Thus, instead of indicating the maximum strain of 906 με, as given by the ESG, FOS-A measured only 493 με. This small FOS strain continues to decrease with cycling until the end of the tests, as opposed to the ESG one that exhibits a slight increase.

The strain extremes for the R2 beam are presented in Figure 5.9. This beam exhibited an unexpected decrease in strain in the initial 1000 cycles, probably due to the stress distribution along the CFRP and the way the cracks propagated. At the beginning of the test both the FOS and ESG gave similar strain values. As cycling continues the strain increases as shown by ESG. However, the sensor could not follow the ESG, and FOS strains gradually diverge from those of the conventional gauge.

A comparison of the strain values obtained by means of the FOS and ESG in the last cycle is given in Table 5.2 for both the CarboDur and Replark beams. The difference between strains measured by the FOS and the ESG strains indicates that for both C1 and C2 specimens the FOS failed during the fatigue load. In contrast, FOS strains compare well with the ESG ones for beams R1 and R2. To make a distinction between FOS that failed and the ones that gave reliable readings, a star is added to identify the strain when failure happened.

Figure 5.10 shows the initial loading of the beam CW-S that underwent 13 wet-dry cycles in saltwater. A good agreement can be noticed between the FOS-A readings, that was submitted to the same conditions as the beam specimen, and the ESG strains. The unexposed FOS-B measured slightly higher strains for this initial ramp loading. This difference can be explained by the fact the FOS-B, being installed after the exposures, had different initial stress conditions than FOS-A. As the loading continues with the first cycle, as shown in Figure 5.10, the FOS-B follows closely the reference signal given by the ESG. At the maximum strain, the aged FOS-A records a 300 με drop. This sudden failure in strain can be explained by several possible factors as the loss of bond between the FOS from the CFRP host material, or the damage of the optical fibre sensor itself. The first hypothesis, degradation of the FOS-CFRP bond, can be caused by the adverse effects of the water exposure conditions on the quality of the adhesive.

Figure 5.11 presents two additional fatigue cycles for beam CW-S. The FOS-B shows almost the same strains as the ESG, but FOS-A measured smaller strains. By taking the minimum and maximum strains and plotting them against the number of cycles, Figure 5.12 will be obtained. This figure shows the evolution of strains throughout the fatigue test for beam CW-

S. It can be observed that a good correlation exists between ESG and FOS-B readings. The different strains recorded by the aged FOS-A can be explained by the failure of the bond between the FOS and CFRP. Indeed, in the first cycle there is a sudden drop, presented in Figure 5.11, but the strains continue to decrease gradually with cycling.

For the last cycle, the minimum and maximum strains in the CFRP at midspan, measured by ESG and FOS for all the beams are listed in columns 2 to 7 of Table 5.2. For all the C-specimens, the FOS installed before exposure failed to measure strains precisely. Usually, a sudden decrease in strain is exhibited by water-exposed sensors at the very beginning of the cyclic loading and at strains no larger than 1000 με. In the case of CW-S, this happens from the first cycle, as depicted in Figure 5.11. As this happens soon after the initiation of cyclic loading, one supposes that the water immersion had a damaging effect on the FOS systems mainly through altering the bond between the fibre and the CFRP plate. Of the four water exposed C-specimens listed in the table, three of them gave reliable FOS-B strain readings, that is, specimens CW-S, CI and CI-S. The specimen CI gave good FOS results for the maximum strain but a large difference is observed between minimum strains measured by the two systems. Both FOS installed on beam CW failed to give reasonable strains.

The second specimen immersed in water considered for a discussion is the Replark-strengthened beam RW-S, that was exposed in saltwater for 13 wet-dry cycles. Figure 5.13 shows the strain for the ramp and the first cycle of loading. It can be seen that the FOS readings follow the ESG ones for the ramp loading. It also captured well the drop in strain when the beam cracked, at about 65 seconds, though FOS-B exhibits higher strains than the FOS-A and ESG.

Figure 5.14 depicts two other cycles as recorded by the two sensors and the gauge. The good correlation between the FOS-B and ESG strains can be again observed, although FOS-A measures smaller strains than ESG. An interesting result is that the difference between FOS-A strains and ESG is larger for the 201 000 cycle than at the 401 000 cycles. Usually, this difference increases with cycling, or at most remains constant. The possible explanation for this fact is given below.

Strain evolutions for RW-S are presented in Figure 5.15. The strain as measured by the FOS and ESG varies a lot. Until about 40 000 cycles the two sensors FOS-B and FOS-A record larger strains than the ESG. From this point onward FOS-A failed to accurately measure strains, though at the last cycle strain values are similar to the readings obtained by the ESG. The FOS-B exhibits larger strains than ESG up to 200 000 cycles and then shows a good correlation with ESG strains until the end of the test.

The discrepancies in strain readings given by the two sensors and the gauge observed above are hard to explain. For instance, for the same loading condition, maximum deformations measured on the Replark CFRP varies from 114 με for R2 to 2916 με for RW. Because the Replark CFRP system gives highly variable strain responses from one specimen to another, it can be hypothesized that the strains change for a given section even in the case of the same specimen. The voids in the adhesive layer between the CFRP and concrete, and the flexibility of the Replark sheets are the possible reasons for this. As the collocated sensors are close to each other but not superimposed, this being usually impossible, there may be some strain difference due to this fact.

Table 5.2 shows the strain values in the last cycle for all these specimens. In the case of RW and RI two values are observed for strain values by ESG. These values represent strains at the central section given by two different electrical gauges. The bonding of a second ESG was necessary because the first FOS-B installation failed and the configuration in Figure 3.2(d) could not be respected. Instead, a second FOS-B was installed 50 mm away from midspan, and next to it was placed the second gauge. Thus, the first value given by the ESG corresponds to the gauge collocated with FOS-A, and the second value corresponds to the gauge placed aside FOS-B. Of the four Replark-strengthened beams submitted to water exposure two of them gave reliable FOS-A readings. The water exposed sensors installed on beams RW-S and RI-S show strains very similar to those of the ESG, as columns 2, 4 and 5, 7 of Table 5.2 indicate. The FOS-B, installed after the exposures, gave reliable readings for these two beams and the RW specimen.

For both CarboDur and Replark-strengthened beams in Series I, the installed sensors monitored strains through the fatigue tests. However, these results are less precise than those for the FOS installed on beams in Series II presented in Table 5.1. A possible cause for this is that the CFRP-FOS bond may have been affected by the water immersion.

5.4 Post-fatigue behaviour of FOS under static loads

The 25 beams instrumented by FOS sensors and tested in fatigue, with results presented in section 5.3, were finally tested quasi-statically to failure. The quasi-static test results are presented in 5.4.1 for the specimens that were submitted to low-level cycling, and different numbers of cycles. In 5.4.2, the failure test results for beams loaded with three different numbers of cycles at high-level fatigue load are discussed. Some beams were exposed to water prior to the fatigue tests and their static test results are presented in 5.4.3.

5.4.1 Post-low-level fatigue capability to measure strain

In this subsection, FOS and ESG readings from quasi-static obtained on seven L-beams in Series II, two Replark, R1, R2, and two CarboDur beams, C1, C2 of Series I are presented. Of the 11 low-level cycled beams in this subsection, results from five are presented graphically in the following. The results for the other beams can be found in Appendix E. One beam for each three final numbers of load cycles are presented. These are L400B, L800C and L2000B. In addition, results from FOS installed on the beams C1 and R2 are also discussed in detail.

Figure 5.16 presents the load-deformation responses for three L-beams L400B, L800C and L2000B, as recorded by a FOS and an ESG. Each figure shows two curves corresponding to the two systems used simultaneously for measuring strains. It can be observed that the load-strain measurements obtained by the two systems are very similar on each figure. As the applied load increases, its relationship to the strain remains linear until almost the end of the test. Unlike the reference beams presented in 5.2 and in Figure 5.1, the load-deformation curves do not exhibit a load plateau. This difference was expected and can be explained by the fact that prior to the quasi-static test, L-beams were submitted to fatigue cycling, and as a consequence they were cracked before failure the test. However, the slope of the load-

deformation curves in Figure 5.16 are similar to the ones observed in the second portion of the curves in Figure 5.1.

The FOS gave reliable readings up to about 44 kN for L400B, as shown in Figure 5.16(a). At this point a small drop in FOS strain readings occurs. It can be observed that for L 800C, presented in Figure 5.16(b), the FOS readings are almost coincident with the ESG ones. In the case of L2000B, again a significant drop in FOS strain values is observed at about 55kN. This drop, that also occurred in the case of L400B, is probably caused by the failure of the adhesive layer between the FOS and the CFRP, as discussed in subsection 5.2.2.

The strain data as recorded by the FOS and the ESG are listed in columns 6 and 7 of Table 5.1. Column 6 gives the strain values recorded at the moment when the FOS failed, rather than the strains at the end of the quasi-static test, as explained in section 5.2. In column 7, the corresponding strains measured by the ESG are listed. Column 9 in the table lists the load P measured at failure of the FOS sensor. It can be seen that for four beams out of eight, the FOS gave reliable readings until the failure of the specimen. For the other four cases, the FOS readings had unexpected drops, as in the case of L400B shown in Figure 5.16, and are identified with a star in the table.

The error between the ESG and FOS readings, given in column 8 of Table 5.1, ranges from less than 1% to about 5%. There is no correlation between the number of fatigue cycles and the magnitude of the error. This shows that for the same low-level fatigue load, the post-fatigue response is adequately captured by means of FOS, independently of the number of cycles.

These failure tests confirmed the capability of the FOS installed on CFRP-plated beams to measure precisely strains through fatigue and subsequent quasi-static test to failure, provided that the strain values are smaller than the 3200 με limit. This limit was set according to the minimum strain at which the FOS failed for the specimen L400B, that is 3163 με. It is worth mentioning that this limit was set initially to 4000 με following the static tests on reference

beams NA and NB in the beginning of the chapter, but as a result of fatigue loading, this limit was lowered to 3200 με.

The fibre optic sensors installed on CarboDur specimen C1 failed during the fatigue loading. Therefore, the load-deformation curve from a quasi-static test is unreliable, as shown in Figure 5.17. The FOS reading presents a steeper curve than the ESG one, and measures strains about five times smaller than the conventional ESG. In the case of Replark beam R2, the FOS readings followed the ESG ones as indicated in Figure 5.18. The first slope is captured very well by the ESG up to about 22 kN. There is a slight difference between the FOS and ESG readings at the top of this slope but the following plateau is very similar as recorded by the two systems. At the end of the plateau at 3697 με the FOS failed and from this point forward it measures different strains than the ESG.

The last reliable FOS strain value for specimen R2 is indicated in column 8 of Table 5.2. Similar results are obtained for specimen R1 and the last reliable FOS reading is presented in the same Table 5.2.

5.4.2 Post-high-level fatigue capability to measure strain

From the six H-beams presented here, three resisted the severe cyclic loading conditions to the end of the fatigue test. These are H400A, H800A and H200B and the results from the quasi-static failure test performed on them are presented in detail. The other three beams failed during the fatigue tests as described in 5.3.2.

Similar to L-beam tests, the quasi-static load-deformation curves for H-beams are presented in Figure 5.19. The load-deformation responses show that both the ESG and FOS measure accurately strains to the end of the test. For H400A, shown in Figure 5.19(a), an important strain drop is observed just before failure of the specimen. As explained above, this shows that there is some the FOS-CFRP bond degradation. However, for the other two beams the FOS followed very closely the ESG to the failure of the specimen.

The FOS and ESG strains at the end of the tests are presented in columns 6 and 7 of Table 5.1 The corresponding error and load, P, are listed in columns 8 and 9. Overall, the strain values read by the two systems are very similar. Negligible FOS error values are noticed for the three H-beams tested quasi-statically. Since these values compare with values obtained for L-beams, it can be concluded that there is no correlation between the error in the FOS reading and the load amplitude used in fatigue cycling.

5.4.3 Effect of water exposures

From the eight specimens immersed in water, two typical post-fatigue responses of water-exposed beams are portrayed through the results obtained on CW-S and RW-S. Both specimens were submitted to 13 wet-dry cycles in saltwater. Similar results were obtained for the other beams and are discussed here.

Figure 5.20 presents strain measurements taken by one ESG and two FOS on CW-S specimens during the quasi-static loading to failure. The ESG strain-load curve, represented by the thick line, shows a linear strain increase with load until failure at 69.2 kN and a maximum strain of 4030 με. Contrary to the ESG, the two FOS ceased to accurately measure the strain before reaching the ultimate capacity of the beam. The aged FOS-A failed during the fatigue loading and its readings are no longer reliable. However, the FOS-B sensor that was installed after the water exposure gave reliable readings up to 2220 με. Here, the initial drop observed is followed by three successive drops to complete failure at 2377 με. However, the FOS-B follows very well the ESG until the first drop occurs. The two FOS were supposed to record similar values, yet due to the FOS-CFRP bond degradation as a result of immersion to water, they failed to do so.

Post-fatigue strain results for the specimen RW-S are presented in Figure 5.21. Compared to the results obtained on the previous CarboDur-specimens, these strain measurements change a lot with respect to load. The strains given by the two FOS closely follow the slope exhibited by the ESG up to about 13 kN. Then, they show sudden deviations from the reference ESG strain signal. The FOS-A from this point forward records smaller strains than the ESG. The FOS-B measures smaller strains than the ESG but larger than FOS-A. At 2042 με, FOS-B

shows a sudden drop that was considered to be failure. Then, a few fluctuations in FOS-B strains around the ESG curve are observed and the final failure at about 3800 με, this being also the strain at which FOS-A exhibits its failure. The differences in strain readings by the two systems can again be attributed to the fact that Replark reinforcement is more flexible and is applied manually by a wet lay-up procedure. When used as external reinforcement, due to its nature, it is difficult to correctly predict the strain distribution along the bond, as well as along one cross-section.

The FOS failure and the corresponding ESG strains are compiled in Table 5.2, in columns 8 through 11. For CW-S, it can be observed that the FOS-B, installed after the water immersion, failed at a load of 38.3 kN with the last reliable reading of 2220 με. At the same instant the aged FOS-A recorded 1364 με, whereas the ESG measured 2138 με. One can see the good correlation between the values measured by both the FOS-B and ESG. The discrepancy between aged FOS-A and ESG is explained by the fact that the sensor had failed during the initial fatigue loading. Similar results are presented in Table 5.2 for the rest of the beams. Overall, the FOS readings compare well with the ESG ones, and a very good correlation was found especially between FOS-B and ESG.

The FOS sensors in Series I were supposed to have an operating range large enough to measure strains up to failure, that is –1000 με to +10 000 με. However, only a few beams were properly monitored by means of FOS, and those not to the end of the test, but to the maximum strain value of about 3700 με. As explained in section 5.2.2, the insufficient FOS capillary length is thought to be one reason for this. Another reason would be the water immersion that could damage the FOS-CFRP interface and thus compromise readings. For the beams in Series II, that were not immersed in water, the FOS operating range was –1000 με to +5 000 με, and the maximum strain that could be measured was 4645 με. This value is very close to the maximum strain-range specified by the manufacturer.

5.5 Summary

The chapter presented the quasi-static, fatigue and post-fatigue static behaviour of FOS-instrumented beams submitted to water exposures. The capabilities of the Fabry-Perot FOS bonded on two types of CFRP products were tried through a sequence of testing to study several parameters. They include the influence of: fatigue cycling, cycle load amplitude, number of cycles, and ordinary or saltwater immersion.

For the FOS system and specimens used in this study, and for strains up to 3300 με, there was no noticeable influence of the amplitude of the load cycle and the number of cycles on the readings. Thus, the FOS tested for zero cycles and for two million cycles with load amplitudes producing strains from 1000 to 3300 με, were both capable of accurately measuring strains. However, sudden drops in strain readings are observed in the quasi-static tests starting from about 3200 με. They cannot be correlated to previous fatigue loading because control tests with no cycling also showed this drop. They could be attributed to the degradation of the bond between the FOS and the CFRP due to presumptive insufficient anchorage length of the FOS capillary. Consequently the FOS would slip, and the strain drops would be observed in several cases.

The influence of the water immersions seems to seriously affect the strain readings. Thus, the FOS sensor completely immersed in water was not sufficiently protected against the aggressive environment and most of the time, it failed to read the exact strains at the initiation of the cyclic loading. Degradation of the adhesive was most probably the cause of this failure. The actual protection procedure may have not been adequate for these severe water exposure conditions. However, in the real life of a structural element, such as a beam, one can hardly find this hostile water and saltwater environment.

Generally, for immersed specimens small strains measured during static loading such as ramp loading, FOS readings are in good agreement with those of ESG. Dynamic loads causing low strains give a gradual failure of the sensor, but if the load causes high strains a sudden failure of the FOS is observed.

The first FOS purchased before 2000, for the Series I, exhibited some errors that are, anyhow, smaller than the 15 % limit cited in the literature. The other sensors installed on beams in Series II purchased in 2002 showed a maximum error as low as 5%, and a mean of 2%. The results obtained with sensors fabricated before 2000 were not satisfactory, but those obtained after 2002 were very good. This is mainly due to the fact that their quality improved in time, as well as the skills needed for their installation. Overall, these results confirm that the FOS is capable of measuring strains precisely for a variety of loading conditions, load ranges, and number of fatigue cycles.

Table 5.1 FOS test results for low- and high-level fatigue loaded CarboDur specimens

Specimen	Fatigue strain in the last cycle				Static test			
	Minimum		Maximum		Strain			Load
	FOS (με)	ESG (με)	FOS (με)	ESG (με)	FOS (με)	ESG (με)	Error (%)	P (kN)
Reference								
NA	-	-	-	-	4645	4700	1.17	55.6
NB	-	-	-	-	4037*	4174	3.28	48.7
15-35% of M_y								
L400A	994	965	1413	1401	4083	4018	1.62	56.6
L400B	1159	1167	1650	1678	3163*	3332	5.07	44.6
L800A	1085	1026	1546	1492	4372	4306	1.53	56.3
L800B	1033	1002	1520	1504	3929	3910	0.49	54.8
L800C	1114	1114	1649	1639	4043	4070	0.66	57.2
L2000A	1180	1082	1646	1669	3870*	3956	2.17	55.0
L2000B	1121	1107	1641	1596	3984*	3818	4.35	54.6
35-75% of M_y								
H400A	2387	2355	3343	3346	3734*	3772	1.01	56.8
H400B	2187	2173	3029	3034	-	-		-
H800A	2316	2275	3280	3258	3522	3576	1.51	59.0
H800B	2106	2193	3025	3149	-	-		-
H2000A	2337	2300	3268	3260	-	-		-
H2000B	2210	2257	3246	3294	4102	4220	2.80	62.1
*FOS failed before the beam reached the ultimate load								

Table 5.2 FOS test results for water exposed specimens; 401 000 cycles at 15-35% of M_y

Specimen	Fatigue strain in the last cycle						Static test			
	Minimum			Maximum			Strain			Load
	FOS-A (με)	FOS-B (με)	ESG (με)	FOS-A (με)	FOS-B (με)	ESG (με)	FOS-A (με)	FOS-B (με)	ESG (με)	P (kN)
CarboDur-strengthened										
C1	73*	-	1698	116	-	2306	-	-	-	-
C2	172*	-	405	436	-	959	-	-	-	-
CW	154*	114*	917	454	478	1467	-	-	-	-
CW-S	441*	811	861	840	1392	1410	1364	2220*	2138	38.3
CI	408*	655	941	768	1226	1483	1209	1853*	2218	41.1
CI-S	-7*	1010	1024	416	1596	1585	-	2375*	2280	37.2
Replark-strengthened										
R1	85	-	69	155	-	154	2906*	-	3029	21.8
R2	72	-	114	131	-	194	3697*	-	3490	25.4
RW	1199*	37	2158/40	1705	104	2916/96	-	1046*	1002	23.6
RW-S	624	662	665	778	822	827	1938	2042*	2428	24.7
RI	825*	463*	888/676	1034	601	892/1075	-	-	-	-
RI-S	329	254	358	402	330	472	2328*	1533	2600	23.2
*FOS failed										

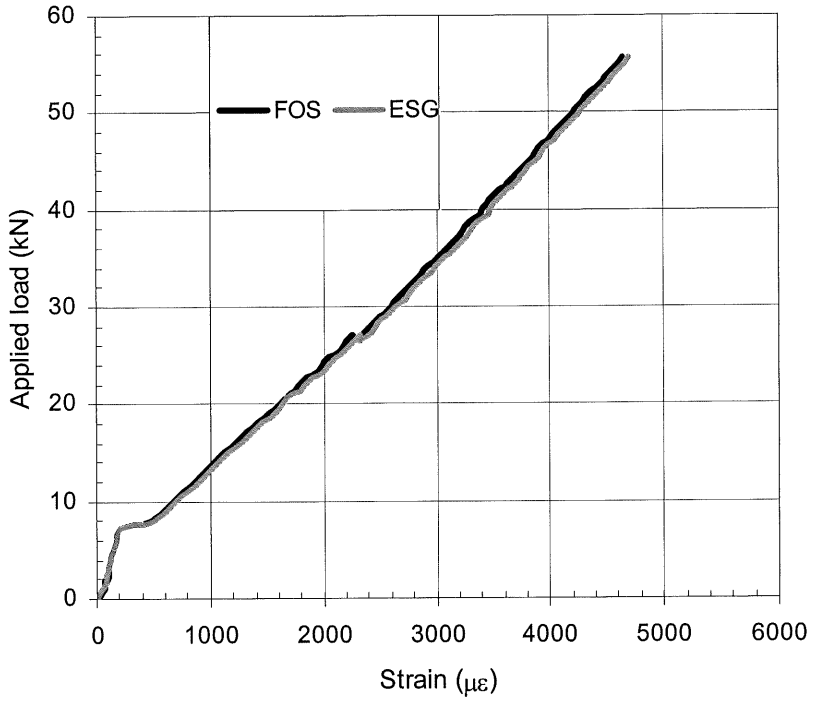

(a)

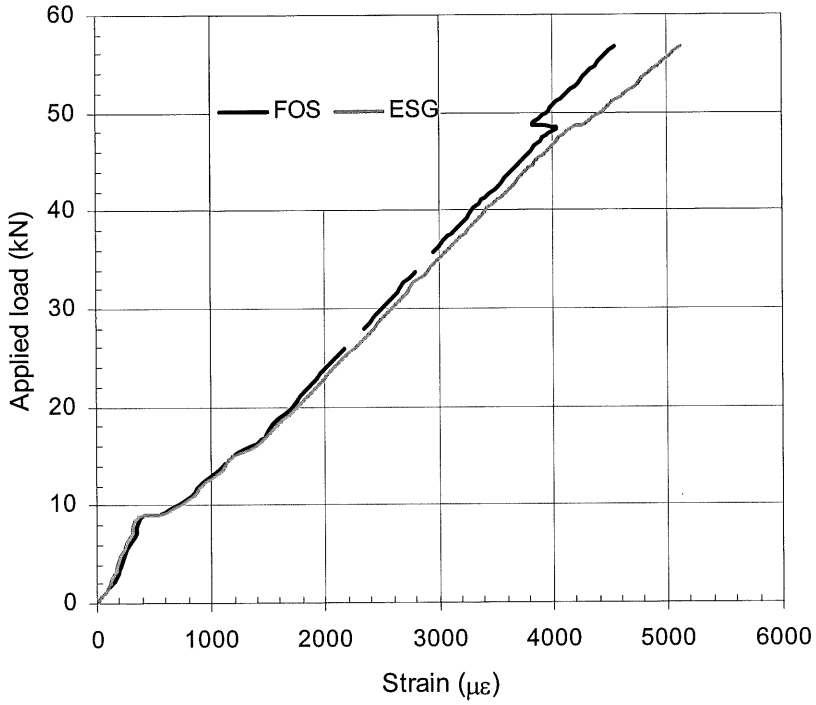

(b)

Figure 5.1 Load versus deformation curves for reference beams NA (a) and NB (b)

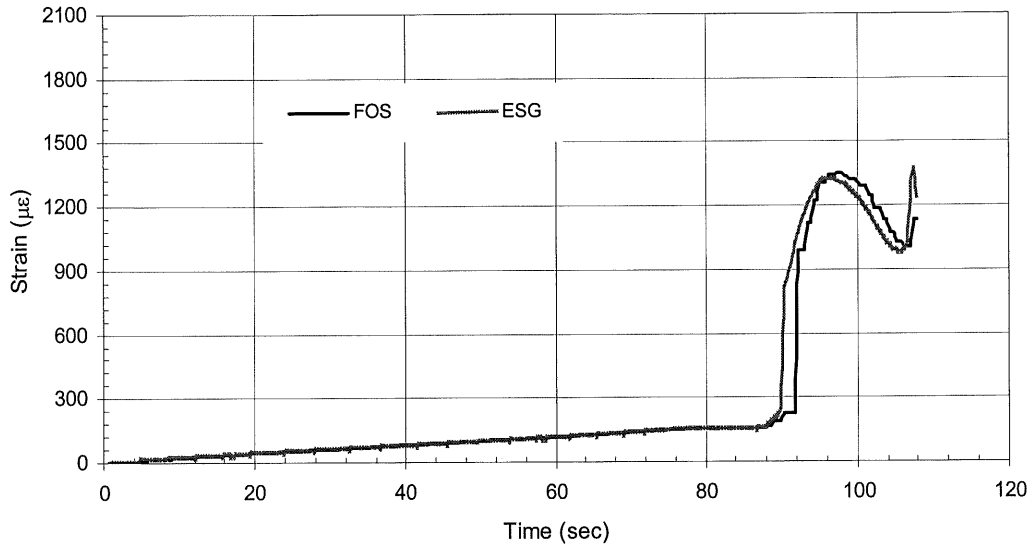

Figure 5.2 Strain measurements for the initial loading by means of FOS and ESG beam L2000B; ramp and first cycle

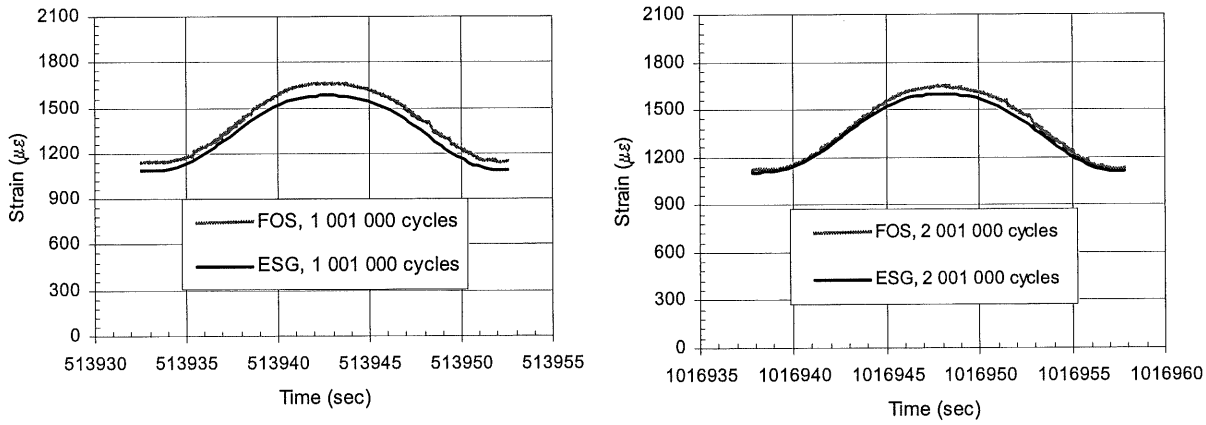

(a) (b)

Figure 5.3 Strain measurements by FOS and ESG beam L2000B; (a) cycle one million and (b) two million

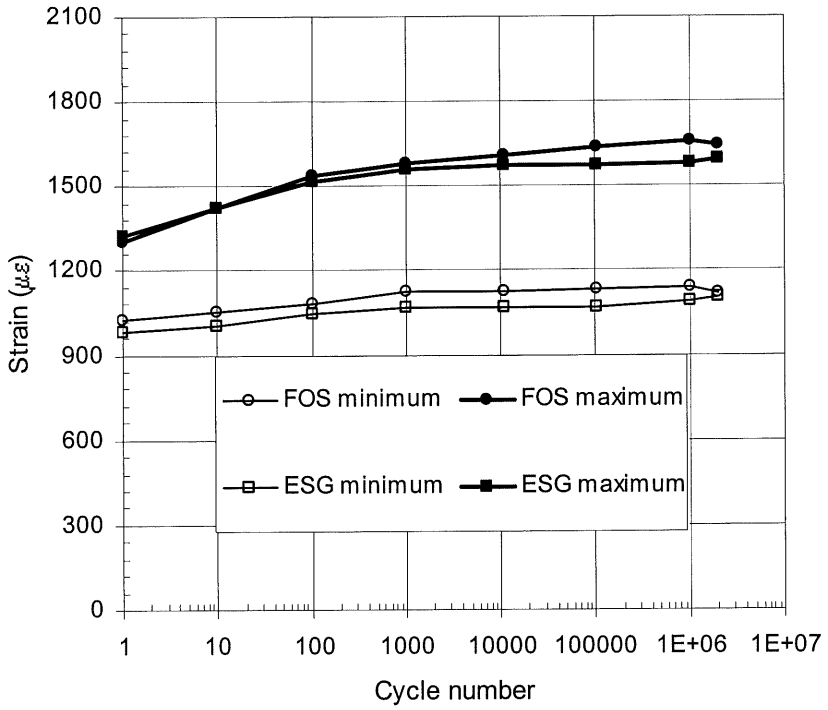

Figure 5.4 Strain extremes during the 2 000 000 fatigue cycles for beam L2000B

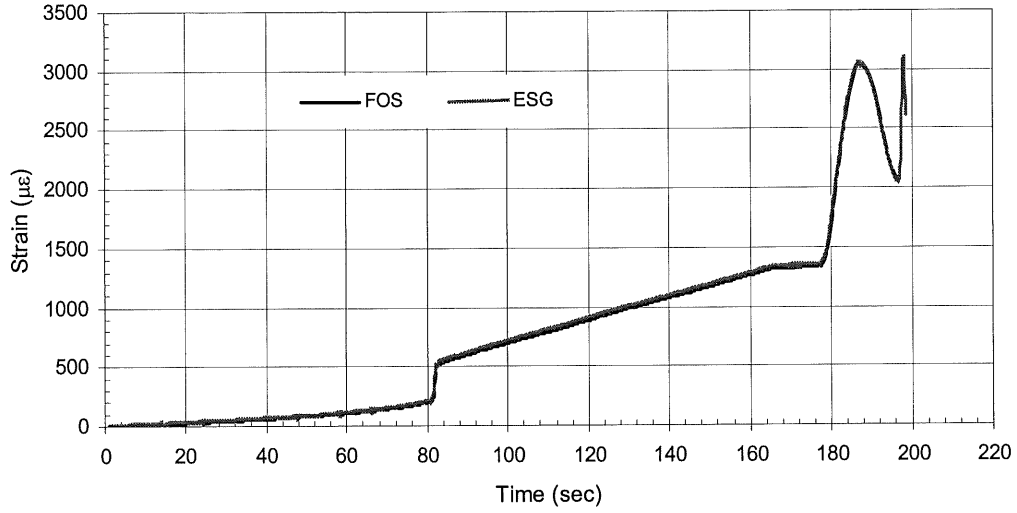

Figure 5.5 Strain measurements for the initial loading by means of FOS and ESG beam H2000B; ramp and first cycle

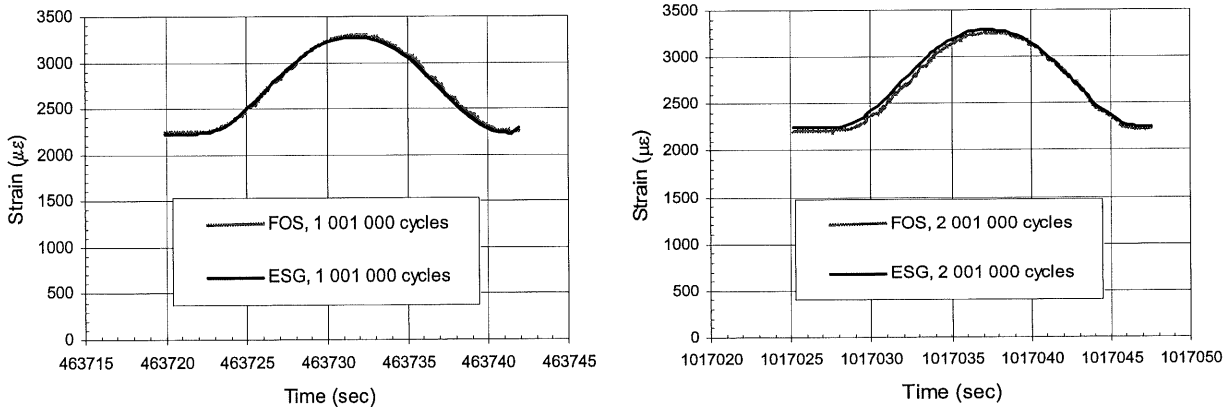

(a) (b)

Figure 5.6 Strain measurements by FOS and ESG beam H2000B; cycle one million (a) and two million (b)

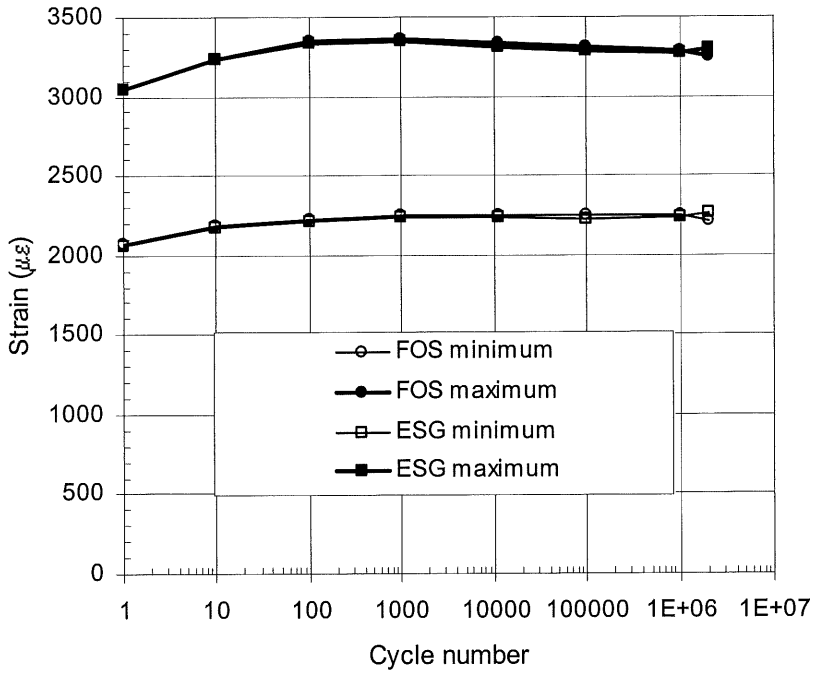

Figure 5.7 Strain extremes during the 2 000 000 fatigue cycles for beam H2000B

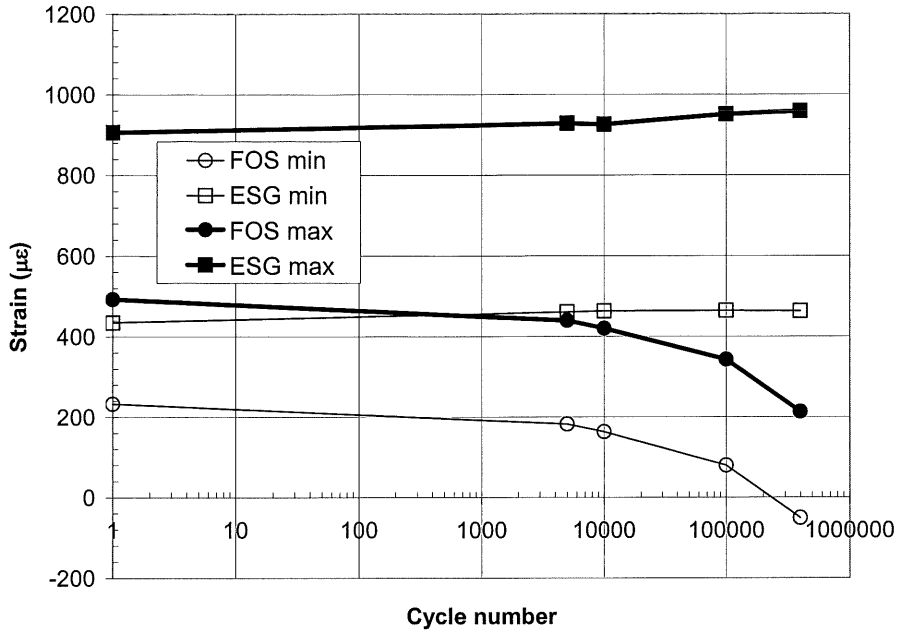

Figure 5.8 Strain extremes during the 400 000 fatigue cycles for beam C2

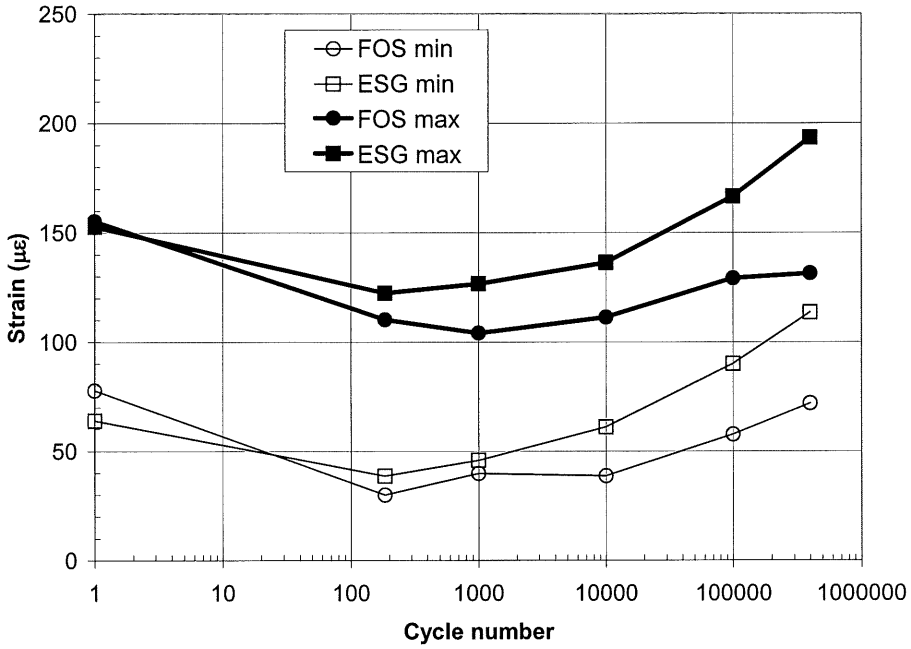

Figure 5.9 Strain extremes during the 400 000 fatigue cycles for beam R2

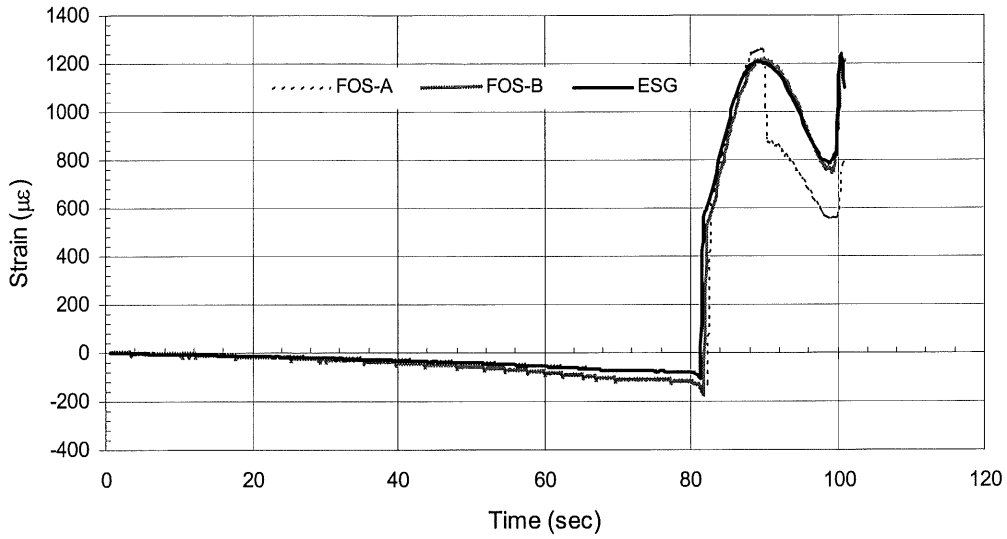

Figure 5.10 Strain measurements for the initial loading by means of FOS and ESG beam CW-S; ramp and first cycle

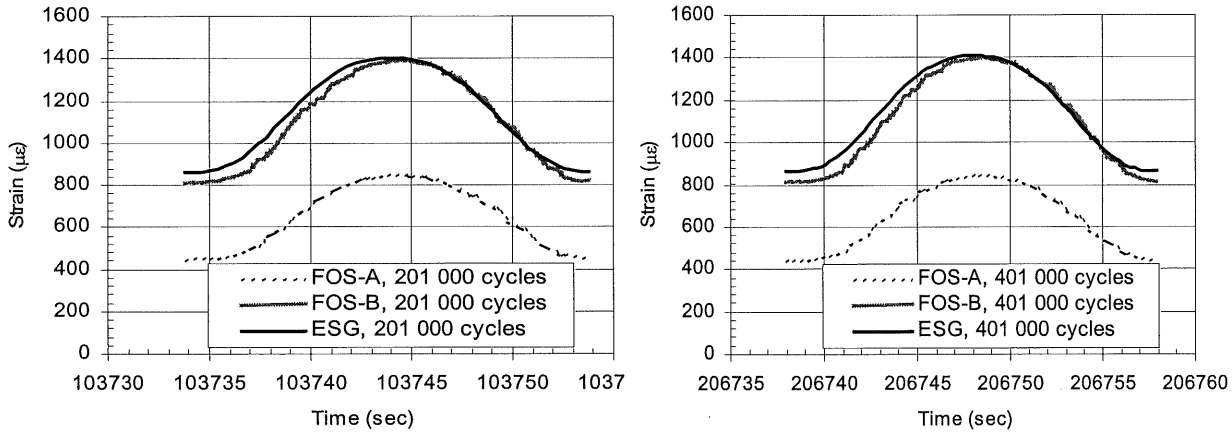

(a) (b)

Figure 5.11 Strain measurements by FOS and ESG beam CW-S; cycle 201 000 (a) and 401 000 (b)

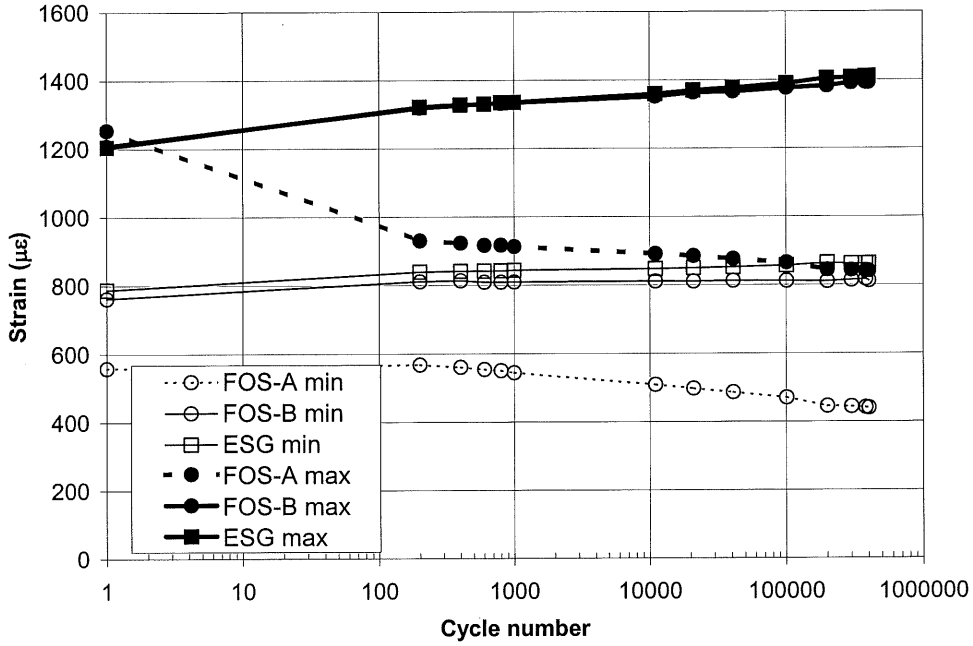

Figure 5.12 Strain extremes during the 400 000 fatigue cycles for beam CW-S

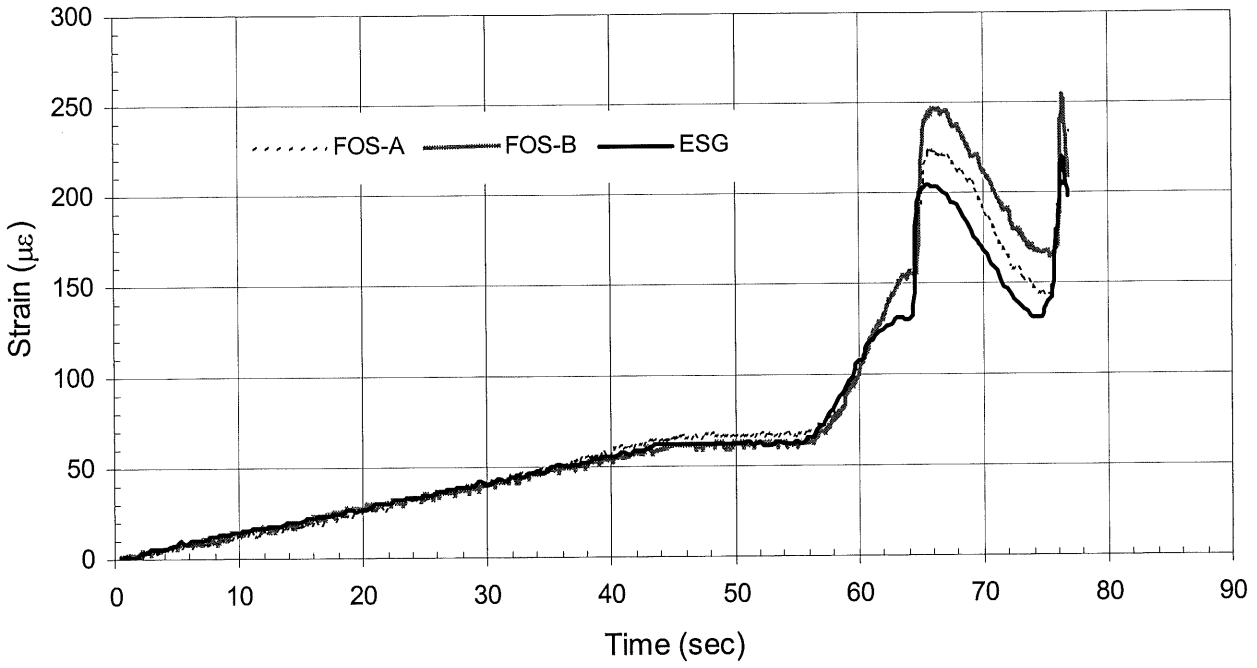

Figure 5.13 Strain measurements for the initial loading by means of FOS and ESG beam RW-S; ramp and first cycle

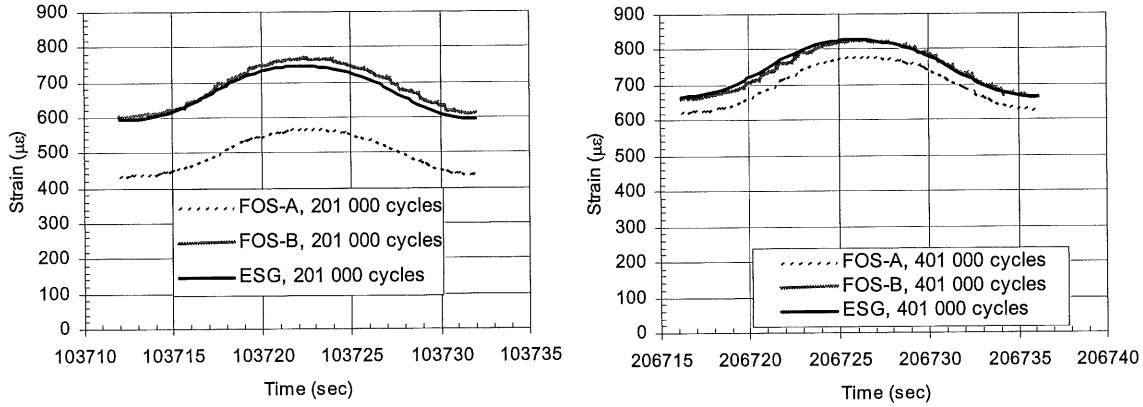

(a) (b)

Figure 5.14 Strain measurements by FOS and ESG beam RW-S; cycle 201 000 (a) and 401 000 (b)

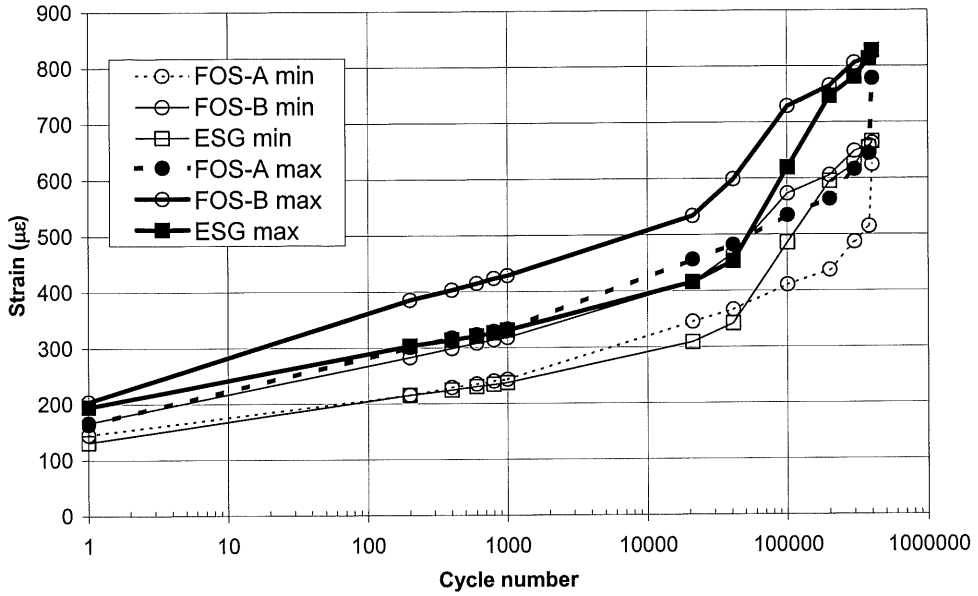

Figure 5.15 Strain extremes during the 400 000 fatigue cycles for beam RW-S

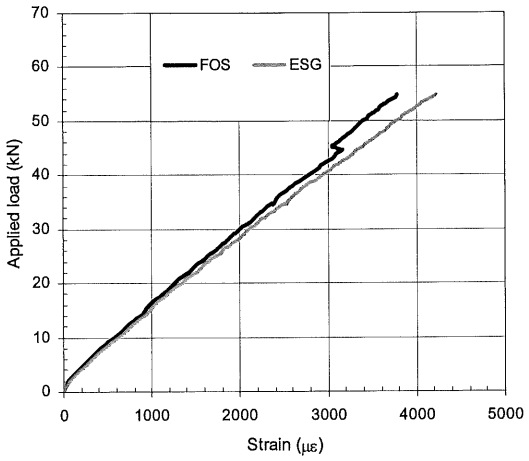

(a)

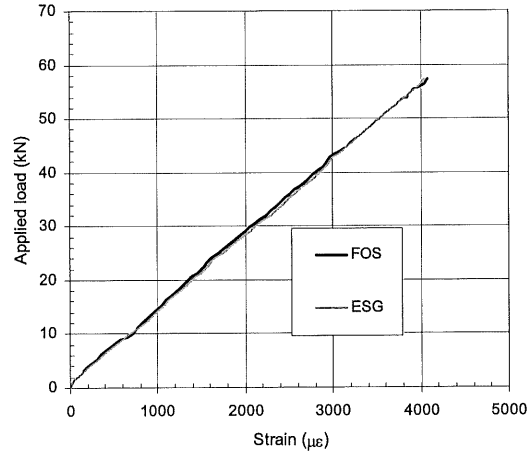

(b)

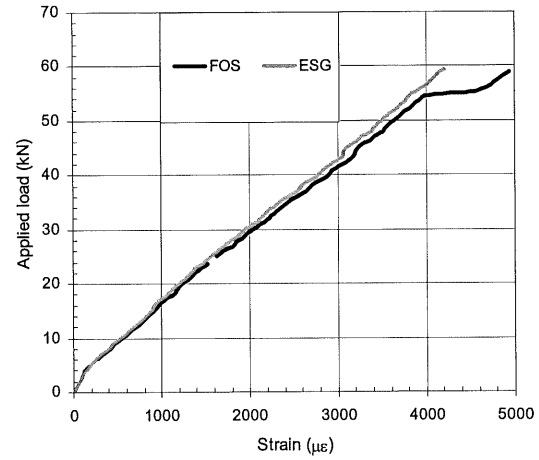

(c)

Figure 5.16 Load versus deformation curves for low-level cycling for L400B (a), L800C (b), L2000B (c)

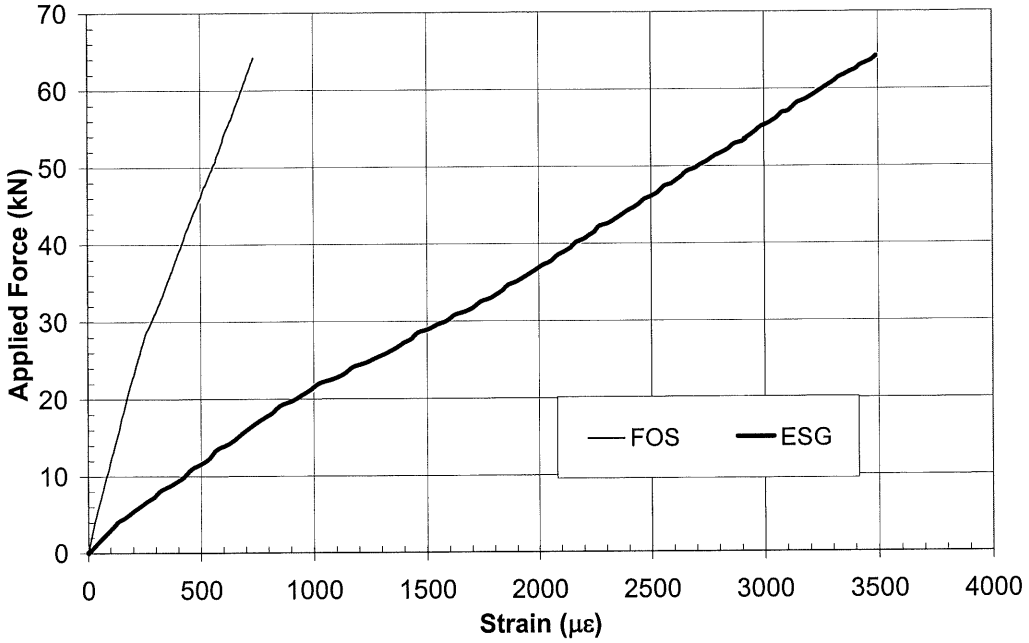

Figure 5.17 Quasi-static load-deformation curves after low-level cycling and water exposure for beam C1

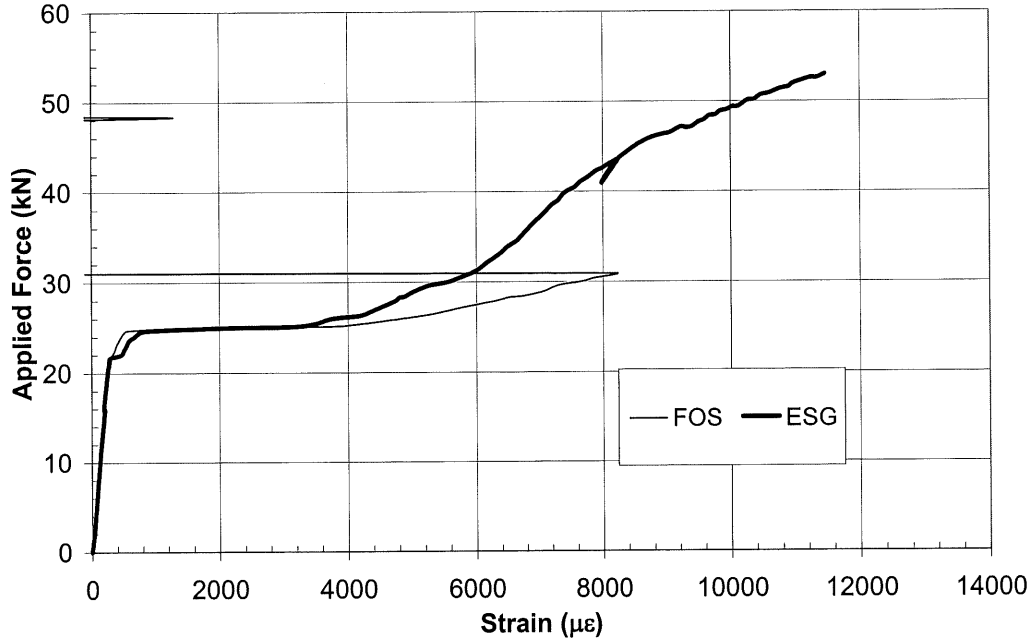

Figure 5.18 Quasi-static load-deformation curves after low-level cycling and water exposure for beam R2

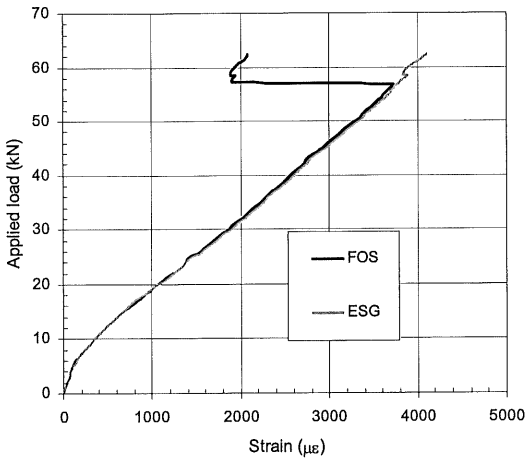

(a)

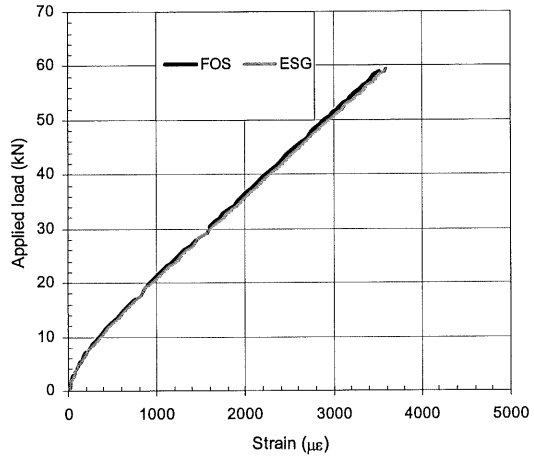

(b)

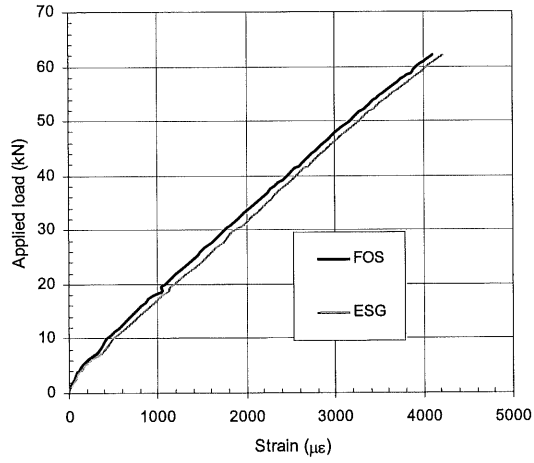

(c)

Figure 5.19 Load versus deformation curves for high-level cycling for (a) H400A, (b) H800A, (c) H2000B

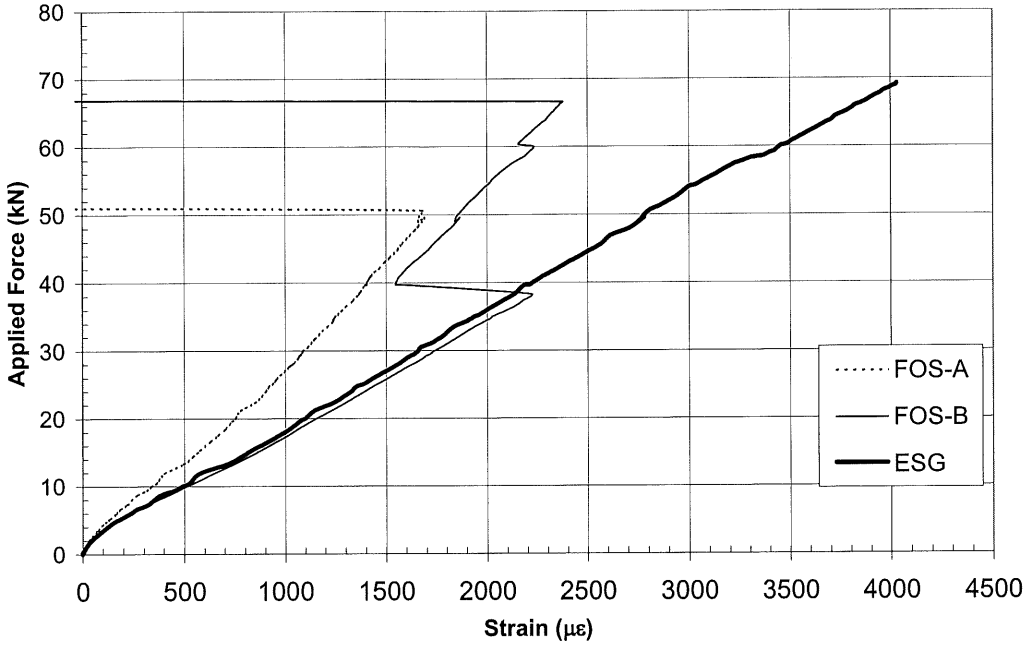

Figure 5.20 Load versus deformation curves for low-level cycling and water exposure CW-S

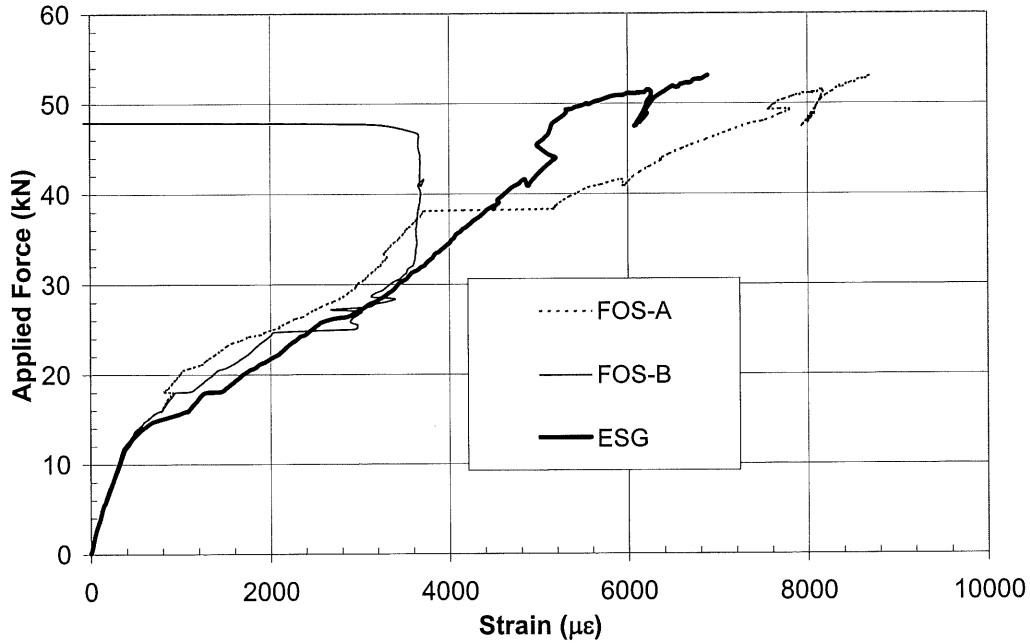

Figure 5.21 Load versus deformation curves for low-level cycling and water exposure RW-S

6 NON-DESTRUCTIVE EVALUATION

6. IMPACT RESONANCE METHOD FOR NON-DESTRUCTIVE TESTING

In this chapter, a non-destructive testing technique is applied for monitoring the changes in dynamic features of the CFRP-strengthened beams already presented in previous chapters. This impact resonance method (IRM), or impact-echo as it also known, is complementary to the FOS monitoring investigated in the previous chapter. It gives information on the resonance frequencies of the specimen, wave velocity, as well as the modal damping ratios. The IRM technique is applied to the Series II specimens of the experimental study. Since the decision to study this method was taken late in the FOS testing program only a few beams were IRM-tested before the initiation of the fatigue loading. For these undamaged beams, a reference vibration signature was obtained. All the beams in L series and H series went through the IRM-testing procedure at the end of the fatigue testing. A single specimen was IRM-tested at regular intervals during the fatigue test. The purpose of this was to monitor changes in vibration characteristics throughout the cycling. The background for the post-processing of IRM test results is presented in section 6.1. It includes the transformation of an acceleration time-history into a frequency response function, as well as the equations to calculate the modal damping and wave velocity from the frequency response function. Section 6.2 presents results obtained through the IRM technique for this single specimen. In section 6.3, changes in vibration characteristics for all the beams of Series II are discussed.

6.1 Background

The IRM technique consists of introducing a transient stress or sound wave into a structure, through a point impact at its surface. This pulse travels into the structure as dilatational (P) and distortional (S) waves, and along the surface as Rayleigh waves. The primary P-wave and the secondary S-wave propagate into the structure along spherical wave fronts. They are both reflected by internal cracks, voids or interfaces, and by the external boundaries of the structure. An accelerometer is used to monitor the surface accelerations caused by the arrival of these reflected waves. The P-wave is of primary importance because it travels at the highest velocity: this wave is also the most easily generated and detected.

In order to show the IRM principle explained in 3.3.2, and to illustrate the concept, the response acceleration measured by a lightweight accelerometer and stored by an acquisition system is considered. Figure 6.1(a) shows the time history of the acceleration caused by an ordinary-hammer impact in the longitudinal direction on a typical CFRP-strengthened beam specimen. The total length of the record is 1024 points and the sampling rate is 20 kHz.

The translation of this time signal into the frequency domain by means of the Fast Fourier Transform (FFT), leads to the evaluated frequency response function shown in Figure 6.1(b). The result can be presented as a graph where the frequency is on the abscissa and the FFT amplitude is the ordinate. In this case, the FFT amplitude is normalized to facilitate the comparison between different tests for which the amplitude was not exactly the same, due to the nature of the manual impact with an ordinary hammer. To counteract this variability in the spectrum amplitude, three impact traces are recorded for each IRM test. Thus, the spectra having similar amplitudes of the impact load were chosen for all the tests. For this case, the Fourier spectrum shows one resonance frequency, this being also the only peak observed in the figure.

One parameter that can be found from the frequency response function is the wave velocity, C_p. Having the length of the specimen, l, and the resonance frequency from the Fourier spectrum, f, the P-wave velocity is then given by (Sansalone, 1997):

$$C_p = 2lf \tag{6.1}$$

This value is important: it characterizes the soundness of the concrete. For instance, for a normal-strength concrete a value larger than 3500 m/s usually indicates that the studied concrete is sound (Cheng and Sansalone, 1995; Jin and Li, 2001). Values shown to be under this limit indicate that there is some degradation in the concrete, such as stiffness degradation due to cracking.

Another parameter that can be found from the Fourier spectrum is the modal damping ratio, ξ. The method used to evaluate this damping ratio is the Half Power Method. This consists of

measuring two frequencies, f_1 and f_2, corresponding to 50% of the maximum power, or 70.7% of the maximum amplitude on the Fourier spectrum. This is shown graphically in Figure 6.1(b). The formula used to calculate the damping ratio is then (Clough and Penzien, 1993):

$$\xi=(f_2-f_1)/(f_2+f_1) \qquad 6.2$$

The damping ratio for concrete elements free from cracks is usually below 1%; for a cracked structural concrete, it is usually larger than 1% but lower than 3% (Laura et al. 1998). Larger values are sometimes encountered for specific applications, as will be seen in the following.

6.2 Resonant frequency and modal damping ratio through fatigue tests

For the purpose of the IRM evaluation, one undamaged CFRP-strengthened beam was tested in fatigue for two million cycles at 3Hz, with a load amplitude of 15 to 35% of the yielding moment. At regular intervals throughout the fatigue loading, the specimen, instrumented with accelerometers as shown in Figure 3.4, was tested by IRM in order to monitor changes in its longitudinal, transverse and torsion resonance frequencies. In addition, the modal damping ratios and the wave velocity through the concrete beam were determined from IRM test results.

All the parameters listed in section 6.1 were evaluated for each of the three vibration modes that made up a resonance test. The IRM tests were conducted initially, before the fatigue loading, and then the three resonance resonant frequencies were measured after the first, tenth, 50^{th}, 100^{th}, 200^{th}, 1000^{th}, 9000^{th}, 50 000^{th}, and 100 000^{th} cycles. From the 280 000^{th} cycle onward, measures were taken at approximately every 250 000^{th} cycle until the end of the two million cycles. At the same time, a set of three Fourier spectra was produced for each vibration mode, giving a result similar to the spectrum in Figure 6.1(b). Four such sets are presented graphically here.

Figure 6.2 shows a set of three curves representing the Fourier spectra for the three vibration modes of the studied specimen. It illustrates the longitudinal, transverse, and torsional frequency response of the CFRP-strengthened beam at the initial undamaged stage. The

longitudinal resonance frequency, f_{lon}, corresponds to the only peak in Figure 6.2(a), and has a value of 1602 Hz. The transverse, f_{tran}, and torsional, f_{tor}, resonance frequencies can also be found to be 1270 Hz and 840 Hz, in Figures 6.2(b) and (c), respectively. In addition to the peaks observed at these frequencies in the spectra, a few secondary peaks with low amplitudes can also be noticed. They represent boundary reflections of the P-wave through the specimen. These reflections were not seen in the longitudinal mode because the impact was applied collinear to the accelerometer direction whereas for the other two modes the hammer hits the specimen parallel to the accelerometer, as shown in Figure 3.4.

In addition, the P-wave velocity, C_p, can be calculated according to Equation 6.1. At 3845 m/s value it is over the 3500 m/s boundary, showing that the concrete is sound and free from cracks or other damage. The damping ratios, ξ, can also be calculated with Equation 6.2. For the longitudinal mode, its value of 0.65% is smaller than the 1% limit above, showing again the soundness of the concrete. However, the two other values of 1.35% and 1.01%, for the transverse and torsion modes, are slightly larger than the 1% limit value. A visual inspection of the beam confirmed that the beam was free from cracks or other damage.

Figure 6.3 illustrates the Fourier spectra for the three vibration modes at the end of one cycle. Overall, the spectra are similar to those in Figure 6.2, but smaller frequencies than at the initial stage are already observed for the three vibration modes. The longitudinal spectrum in Figure 6.3(a) indicates that the frequency decreased to 1406 Hz, a 12% decrease from the initial longitudinal frequency. As for the transverse and torsion frequencies, they both decreased by 5% to 1211 Hz and 801 Hz, respectively. The calculated damping ratios for the longitudinal and torsion modes increased by 58% and 23%, to values of 1.03% and 1.25%. For the transverse vibration mode, the calculated damping ratio is lower than in the case of the undamaged specimen. This unexpected result is discussed later on. The decrease in resonance frequency and the P-wave velocity decrease to 3374 m/s, combined with the increase in damping ratio indicate that there is some damage in the beam. Indeed, visual observations confirmed the existence of one crack of 12 cm in length located at the central span near the beginning of a joint.

The Fourier spectra after one million cycles are presented in Figure 6.4. The first graph in this figure represents the longitudinal spectrum and, apart from the predominant peak, shows two secondary peaks with low amplitudes. Several secondary peaks are observed in the case of the transverse frequency response, in Figure 6.4(b). For the torsion mode, many new peaks appeared, as shown in Figure 6.4(c); they are densely distributed along the frequency axis. The peaks are clear indices of the increasing extent of the damage. Indeed, a second, 10-cm-long crack was observed starting with the cycle 9000. Both existing cracks extended their length, to 13 cm for the first one, and to 11 cm for the second one. Most probably, new microcracking occurred and is reflected in the form of secondary peaks observed in Figure 6.4(c). As a result of the increasing damage level, the values of the wave velocity and damping ratio also changed. The former decreased to 2906 m/s and the latter increased by a significant percentage.

Figure 6.5 shows the spectra at the end of the two million cycle test. The longitudinal frequency response in Figure 6.5(a) remained almost unchanged with the only exception that the resonance frequency shifted to lower values. Figure 6.5(b) shows a new high-amplitude peak at about 2400 Hz that is probably just a second reflection of the boundary of the beam, the first being at 1133 Hz. Clearly visible are an increasing number of secondary peaks, due to damage, especially in the case of the torsion mode, as illustrated in Figure 6.5(c). For the same vibration mode an increase of 223% is observed, the most significant increase in modal damping for the present test. A visual inspection of the specimen revealed a 0.5-cm increase in the length of the two main cracks. The amplitude of the secondary peaks is larger than in the case of the spectra for one million cycles indicating a higher level of damage, mostly through microcracking.

Table 6.1 compiles all the significant data obtained for this beam through all the IRM tests. For the three vibration modes, the resonance frequencies at the initial stage, f_{lon}, f_{tran}, and f_{tor}, are listed. The decrease in frequencies, Δf_{lon}, Δf_{tran} and Δf_{tor}, are also indicated. They represent the change in frequencies with cycling from the baseline values at 0 cycle. The longitudinal frequency decreased from its initial value of 1602 Hz to 1133 Hz, which is a 29% drop. The other two frequencies show decreases smaller than in the longitudinal case, that is 11% for the

transverse mode and 14% for the torsion one. Based on the longitudinal frequencies, the calculated wave velocity C_p is presented also in the table.

If one plots the normalized frequency values versus the number of cycles, Figure 6.6 would be obtained. The figure presents the evolution in the three resonance frequencies of vibration for the beam tested in fatigue. It shows the normalized frequencies versus the number of cycles for two million cycles of loading. The normalized frequencies are calculated by dividing the values in Table 6.1 by the values obtained on the undamaged specimen, that is with zero cycles. In Figure 6.6, it can be observed that the longitudinal frequency decreases the most. This was expected, since the flexural cyclic loading of the beam caused most of the damage to this vibration mode. The decrease in the transverse and torsion frequencies is small due to the fact that cracking occurs in a vertical plane and it is consistent with the fact that no shear or torsion cracks have been observed for the entire duration of the test.

Figure 6.7 shows the evolution of the calculated wave velocity C_p with the number of cycles. It can be observed that this value continuously decreases from the initial value of 3845 m/s, for the undamaged beam, to 2719 m/s at the end of the two million cycles. As was to be expected, the evolution trend of the wave velocity is similar to that of the longitudinal frequency.

Figure 6.8 illustrates the variation of the modal damping ratios, ξ, calculated with Equation 6.2, during the fatigue test. It can be seen that for the three vibration modes, the damping increases with the number of cycles. The damping ratio of the torsion mode is the one that seems to increase the most. This increase in damping ratio is a result of cracking and microcracking. It shows that more energy is dissipating in the beam when it is cracked than in the initial condition. This damping is one of the means to dissipate energy and might be correlated to the area of the hysteresis loop in load-deflection curves.

These damping ratios are also listed in Table 6.2. The longitudinal modal damping increased from the initial damping ratio of 0.66% to the final one of 1.81%, that is, by 177%. For the torsion mode, this increase is 223% to reach the value of 3.28%. The transverse mode

increased by only 34%. The significant increase in damping is mainly caused by the two large cracks observed at the end of the test. They exhibited a gradual increase in length from 10 and 12 cm, to 11.5 and 13 cm.

The damping ratios calculated for the intermediate cycles, and listed in Table 6.2, were expected to show values continuously increasing during the test. For instance, the initial value of 0.65% for the longitudinal mode increases to 1.03% after the first cycle. The damping ratio for the 10^{th} cycle is 0.97% and it was supposed to be larger than 1.03%. Further on this value increases to 1.47% for the cycle 100 and the next one again decreases to 0.89%. Though the damping tendency is an increasing slope, as in Figure 6.8, there are some values that oscillate as indicated in Table 6.2.

Two possible factors can explain these peculiar variations in the damping ratio values. The first is the fact that the distance between two consecutive points in the Fourier spectra is of 19.53 Hz. This resolution may not be sufficient for measuring with enough precision the two frequencies, f_1 and f_2, used in calculating the damping ratio. Diminishing the sampling rate of 20 kHz and/or increasing the 1024-point-length of the record could solve this problem. The manual impacting with a hammer may be the second cause that affects the damping values. One way to eliminate this second factor is to replace the ordinary hammer with a calibrated one, thus controlling the impact parameters. Another solution is to use a shaker, whose excitation is very well defined, instead of the hammer. However, the use of a shaker for the present case is not feasible due to the large dimensions of this device. Finally, the logarithmic decrement may be a better measure for damping characterization for the present structural members. This parameter is calculated directly from the time-history of the acceleration signals. Since in this study the Fourier spectra were the only data saved, the logarithmic decrement could not be calculated.

6.3 Influence of fatigue load range, rate and number of cycles on vibration characteristics

To further discuss the application of this technique for damage detection through vibration characteristic changes, the IRM results obtained on all the beams in Series II are presented. They include seven beams in L-series tested for a varying number of cycles, with a low-level fatigue load from 15% to 35% of the yielding moment. They also include three beams in H-series that completed the fatigue test with cycle amplitude from 35% to 75% of M_y.

Table 6.3 lists the three frequencies for seven L-beams that were low-level fatigued for 400 000, 800 000, and 2 000 000 cycles. The first line lists the frequencies obtained for an undamaged specimen. For the longitudinal mode this value is 1621 Hz, for the transverse and torsion modes they are 1289 Hz and 840 Hz, respectively. The IRM tests performed on another undamaged specimen revealed exactly the same values for the three resonance frequencies. The next lines present these values for the L-beams measured at the end of their fatigue test.

For the specimen L400A, that was tested to 400 000 cycles, the longitudinal frequency decreased to a value of 1270 Hz. This means a 22% decrease from the 1621 Hz value was obtained on the undamaged specimen. In the case of the transverse and torsion modes, these values both decreased by 9%. For the beam L400B, the decrease in resonance frequencies is less significant than for L400A. The longitudinal frequency shows a 16% decrease while the transverse and torsion ones exhibit a 6 to 7% decrease. This discrepancy can be caused by the fact that L400A was tested at a frequency of 3 Hz, whereas L400B was cycled at 2 Hz. It appears the faster is the cycling, the larger is the resonance frequency decrease. Therefore, a higher rate of cyclic loading may cause more damage to the tested specimen.

The next specimens discussed are those submitted to 800 000 fatigue cycles. They are L800A, L800B and L800C and are listed in Table 6.3. The resonance frequencies obtained for these beams range from 1309 Hz to 1406 Hz for the longitudinal mode. Beams L800A and L800B, that were cycled at 3 Hz, exhibit a frequency decrease of 19%, whereas a frequency decrease of 13% is observed for beam L800C tested at 2 Hz. The transverse and torsion frequencies

decreased by 8-9% for beams tested at the higher loading rate as compared to 5-6% for beam L800C cycled at a lower loading rate. This shows that L800A and L800B suffered more damage than L800C. This reconfirms the fact that the extent of damage is dependent on the cycling rate.

The fact that beam L800C cycled with 800 000 cycles had frequencies larger than the beams tested for 400 000 cycles can be explained as follows. The beams presented above exhibited two vertical cracks at the end of the tests. These cracks were usually located in the central portion of the beam, eccentrically about the vertical symmetry plane. Thus, the first crack initiated around one of the two midspan stirrups, as indicated in Figure 3.2(a). The second crack appeared at the second stirrup from the midspan, on the opposite half of the beam, located under the point of load application. In the case of L800C these cracks appeared around the two central stirrups, symmetrically about the midspan of the beam. It seems that when the cracks are symmetric the frequencies are larger. It can be hypothesized that beams with eccentric cracks show smaller frequencies than the ones with symmetrically-distributed cracks.

The beams tested for two million cycles usually showed similar decreases in frequency as the other beams. No major difference among the final vibration frequencies for beams tested with different number of cycles could be observed. Consequently, for the parameters used in these tests, the decrease in frequencies at the end of the tests could not be correlated to the number of cycles.

The calculated damping ratios for the L-beams are listed in Table 6.4. For the undamaged specimen, the longitudinal damping ratio is 0.65% while for both the transverse and torsion modes it is 1.25%. For the fatigue-cycled specimen L400A, the longitudinal damping increased to 1.47% as a result of cracking. For the L400B, fatigued at 3 Hz, these values increased, but to a smaller extent than in the case of L400A, cycled at 2 Hz, indicating a lower level of damage. This fact is consistent with the conclusion that a higher loading rate causes more damage.

The damping ratios for the beams tested for 800 000 and two million cycles are usually dependent on the extent of damage suffered; that is, the larger the extent of damage the higher the damping ratio. However, some values are not consistent with the general trend due to the low resolution in the Fourier spectrum, as discussed in section 6.2.

The resonance frequencies for the three H-beams loaded at 35-75% of M_y and for 400 000, 800 000, and 2 000 000 cycles are presented in Table 6.3. Usually, these frequencies decrease about 18-24% for the longitudinal mode, and 9-16% for the transverse and torsion modes. For all the vibration modes the frequency decrease is 5 to 10% more significant for the H-beams than for the L-beams. The increase in cyclic load amplitude resulted in more damage in the beams. Thus, specimens fatigued at 35-75% of M_y had a larger extent of damage than the beams cycled with 15-35% of M_y.

The damping ratios for H-beams are presented in Table 6.4. For the longitudinal mode these values show that they increase with the number of cycles. Thus, for H400A the damping ratio is 0.79%, and for the beam H2000B it is 1.43%. This trend is not respected for the transverse and torsion modes, as the damping values listed in the table indicate.

6.4 Conclusion

The modal frequencies for the CFRP-strengthened beams can be identified with very good accuracy during fatigue testing using the IRM technique. The three resonance frequencies can be well correlated with the severity of damage; that is, the larger the extent of damage the smaller the vibration frequency. When loaded in bending, a maximum decrease in frequency of 29% is observed for the longitudinal mode. The torsion mode frequency decreased by 14%, and the transverse one by only 11%. Usually, this sequence of decreases is observed for all the beams.

For the same loading conditions the damping ratios seem to increase with the number of cycles. The damping ratios are larger for the transverse and torsion modes than for the longitudinal one. Their values range from 0.6-1.3% in the undamaged state, to up to 3.2% at

the end of cycling. However, the exactness of the damping values needs to be further improved to confirm this.

The FFT curves show that the number of secondary peaks increases with cycling. This is especially evident in the case of the torsion vibration mode. They are the clear indication of progressive damage in the form of cracking and microcracking. Further studies should be conducted to identify the kind of damage and eventually locate it and quantify it.

The results obtained on the specimen IRM-tested throughout the two million cycling indicate that the severity of damage increases with the number of cycles. Naturally, the vibration frequencies decrease continuously during the fatigue test. It can be hypothesized that the same behaviour would have been observed for any other specimens. The decrease in natural frequencies, from the undamaged state to the damage state at the end of the fatigue test, is observed for all the specimens. However, no general correlation could be established between the natural frequencies and the different number of cycles for all the tested beams.

The increasing load range used in the fatigue tests caused an increase in the extent of damage. Thus, the number of cracks increased for specimens tested with high-level cycling as compared to those tested with low-level cycling. Accordingly, the natural frequencies decreased more in H-beams than in L-beams; this decrease is usually 5-10% more significant for the H- than for L-specimens.

In conclusion, the IRM technique can be used for monitoring dynamic characteristic changes in structural members such as RC beams. Both FOS measurements and IRM give information on the state of the structure. A sudden change in strain values could be a warning for an overloading of the structure or a decrease in its performance. The change in dynamic features of a structure could be related to a modification in its environmental and boundary conditions, as well as a damage indicator. FOS continuous monitoring could be used in conjunction with IRM periodical testing to better define the health of any structural element.

Table 6.1 Frequencies and P-wave changes throughout the two million cycle fatigue test with load amplitude 15-35% of M_y

Cycle #	f_{lon} (Hz)	f_{tran} (Hz)	f_{tor} (Hz)	C_p (m/s)	Δf_{lon} (%)	Δf_{tran} (%)	Δf_{tor} (%)
0	1602	1270	840	3845	-	-	-
1	1406	1211	801	3374	12	5	5
10	1387	1211	801	3329	13	5	5
100	1387	1211	781	3329	13	5	7
200	1387	1211	781	3329	13	5	7
1000	1387	1191	781	3329	13	6	7
9000	1367	1191	781	3281	15	6	7
101 000	1367	1191	781	3281	15	6	7
281 000	1348	1191	762	3235	16	6	9
533 000	1309	1172	762	3142	18	8	9
751 000	1289	1172	762	3094	20	8	9
1 011 000	1211	1152	742	2906	24	9	12
1 271 000	1191	1152	742	2858	26	9	12
1 761 000	1172	1133	723	2813	27	11	14
2 001 000	1133	1133	723	2719	29	11	14

Table 6.2 Damping ratios throughout the two million cycle fatigue test with load amplitude 15-35% of M_y

Cycle #	Damping ξ (%)			Increase in damping (%)		
	Longitudinal	Transverse	Torsion	Longitudinal	Transverse	Torsion
0	0.655	1.347	1.013	0	0	0
1	1.032	0.990	1.247	58	-26	23
10	0.975	0.993	0.630	49	-26	-38
100	1.470	1.076	1.781	124	-20	76
200	0.891	1.034	2.077	36	-23	105
1000	0.939	1.624	1.340	43	21	32
9000	1.279	1.090	1.279	95	-19	26
101 000	1.176	0.798	2.395	80	-41	137
281 000	1.194	0.964	1.438	82	-28	42
533 000	1.111	1.652	1.316	70	23	30
751 000	1.446	1.024	1.312	121	-24	30
1 011 000	1.646	0.998	1.477	151	-26	46
1 271 000	1.175	1.171	1.902	79	-13	88
1 761 000	1.402	2.016	2.378	114	50	135
2 001 000	1.813	1.799	3.275	177	34	223

Table 6.3 Change in frequency as a result of fatigue loading

Beam	Cycle #	Frequency (Hz)			Decrease versus 0 cycles (%)		
		Longitudinal	Transverse	Torsion	Longitudinal	Transverse	Torsion
	0	1621	1289	840	-	-	-
Load 15-35% of M_y							
L400A*	400 000	1270	1172	762	22	9	9
L400B	400 000	1367	1211	781	16	6	7
L800A*	800 000	1309	1191	762	19	8	9
L800B*	800 000	1328	1191	762	18	8	9
L800C	800 000	1406	1211	800	13	6	5
L2000A	2 000 000	1328	1191	762	18	8	9
L2000B	2 000 000	1367	1191	762	16	8	9
Load 35-75% of M_y							
H400A	400 000	1270	1152	703	22	11	16
H800A	800 000	1328	1172	761	18	9	9
H2000B	2 000 000	1230	1094	703	24	15	16
* Beams that were tested at a 3 Hz frequency							

Table 6.4 Damping ratios after the fatigue loading

Beam	Damping ξ (%)			Increase in damping (%)		
	Longitudinal	Transverse	Torsion	Longitudinal	Transverse	Torsion
0 cycle	0.647	1.248	1.246	-	-	-
Load 15-35% of M_y						
L400A*	1.469	1.026	1.183	127	-18	-5
L400B	1.382	0.826	1.282	114	-34	3
L800A*	0.842	1.264	1.183	30	1	-5
L800B*	1.386	1.563	1.956	114	25	57
L800C	1.738	0.867	2.144	169	-30	72
L2000A	0.830	0.881	1.116	28	-29	-10
L2000B	0.805	1.649	2.271	24	32	82
Load 35-75% of M_y						
H400A	0.789	1.000	1.490	22	-20	20
H800A	1.161	0.769	2.122	79	-38	70
H2000B	1.431	0.913	1.280	121	-27	3
* Beams that were tested at a 3 Hz frequency						

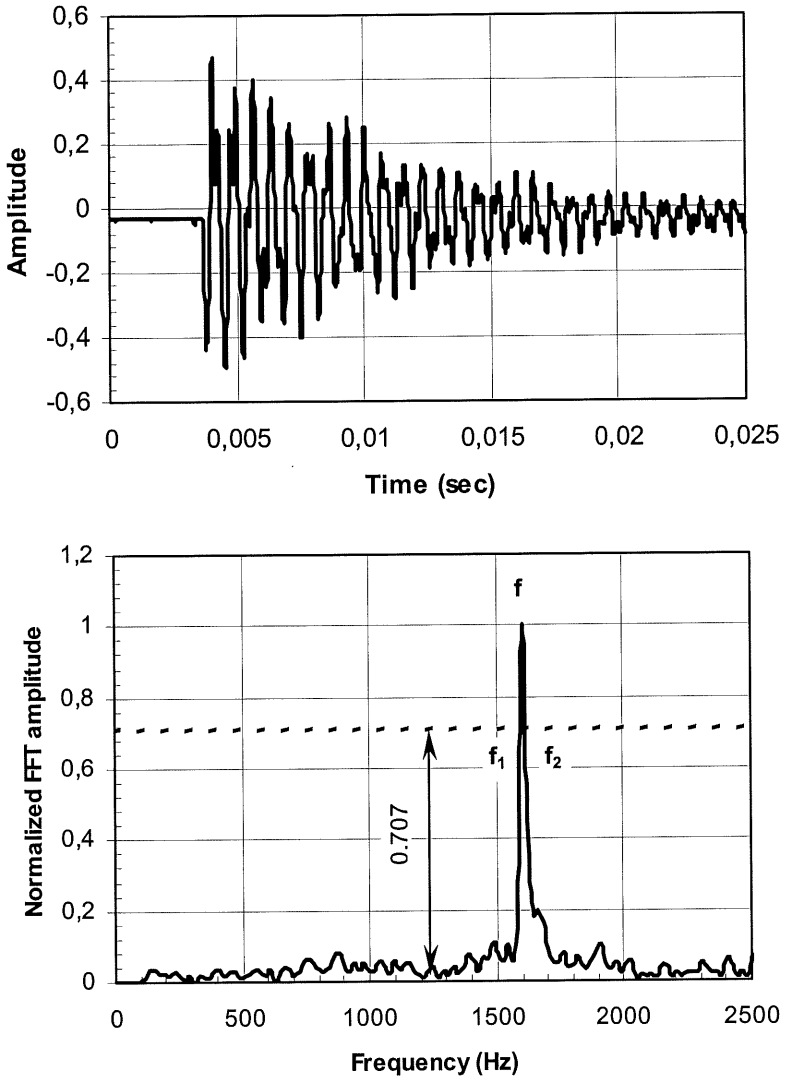

Figure 6.1 Impact resonance method: time history signal (a) for a hammer impact and (b) its Fast Fourier Transform

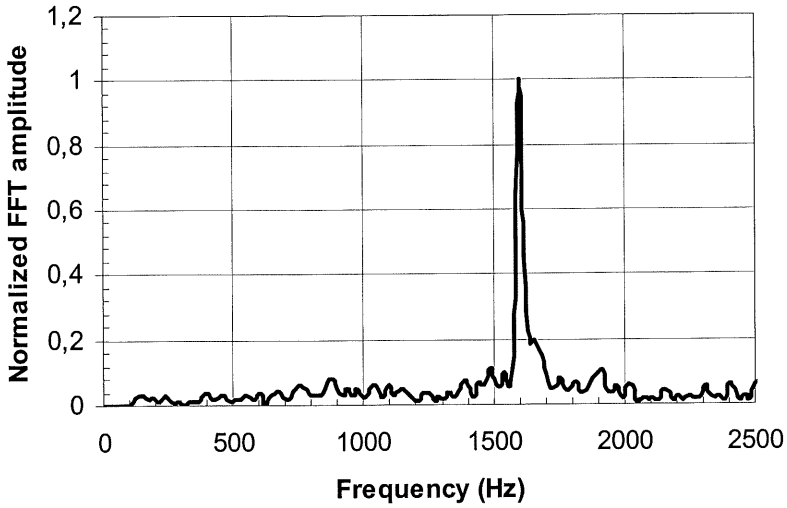

(a)

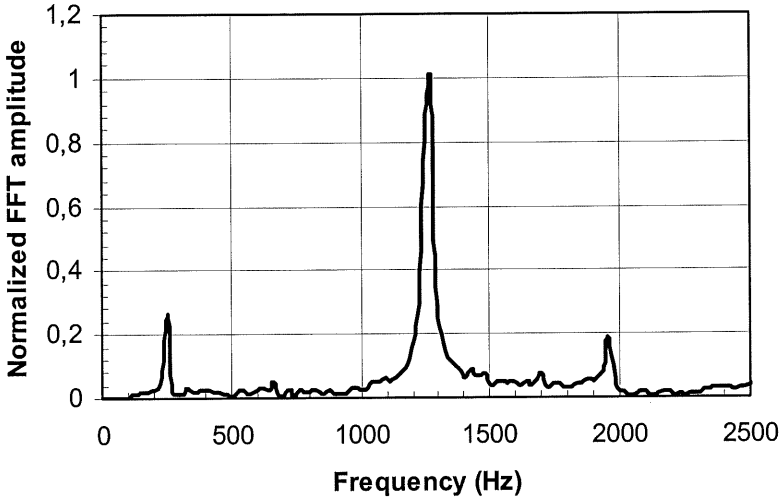

(b)

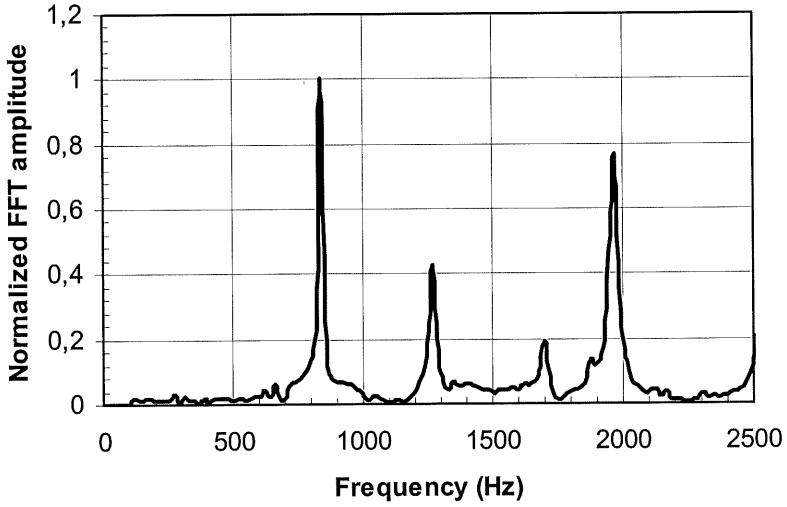

(c)

Figure 6.2 Resonant frequencies for the beam at the initial stage for three vibration modes: (a) longitudinal, (b) transverse and (c) torsion

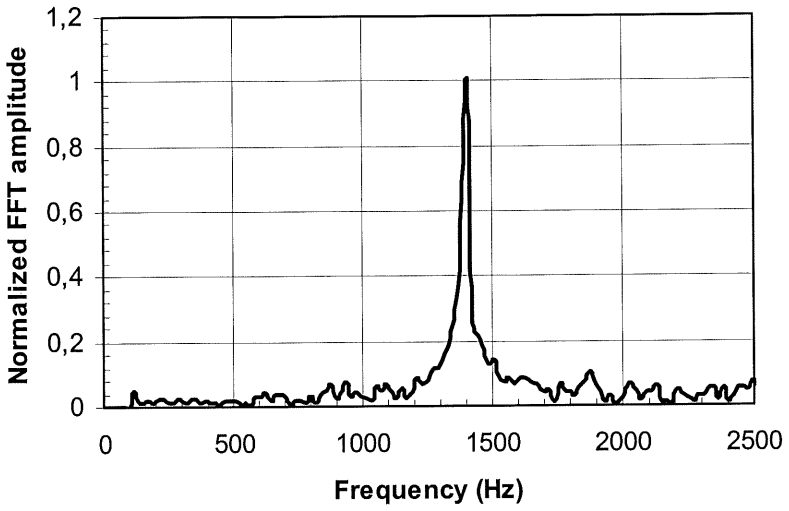

(a)

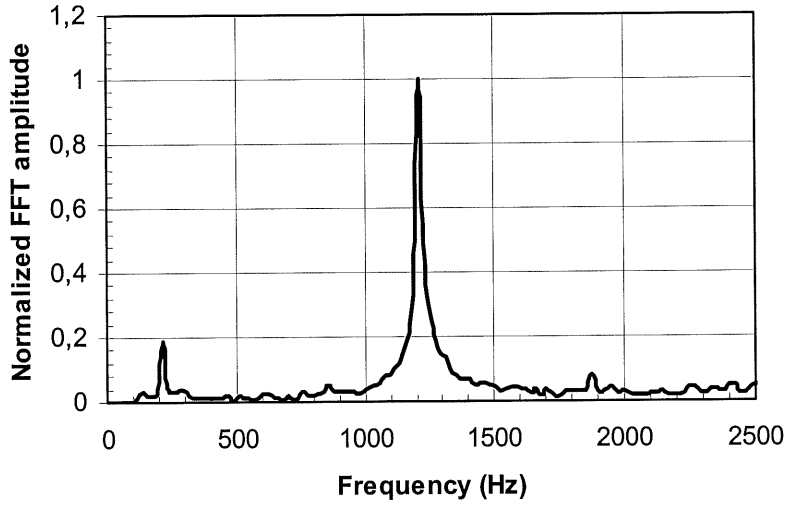

(b)

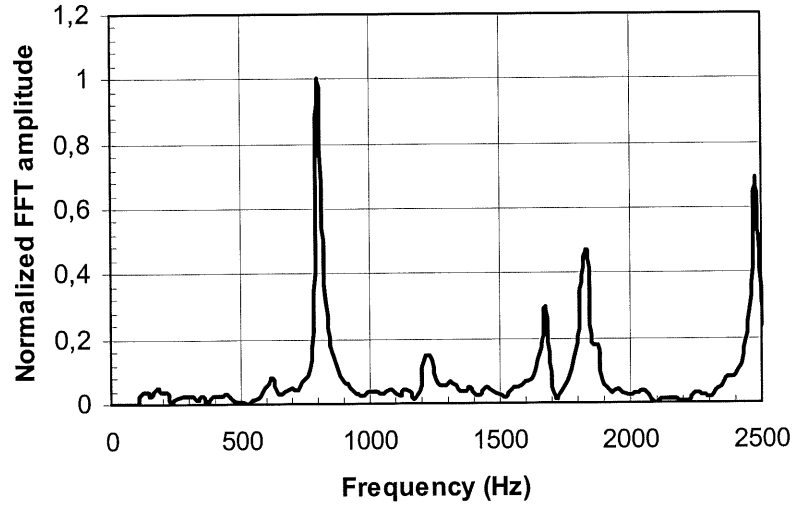

(c)

Figure 6.3 Change in resonant frequencies with fatigue cycles, after the first cycle; (a) longitudinal, (b) transverse and (c) torsion

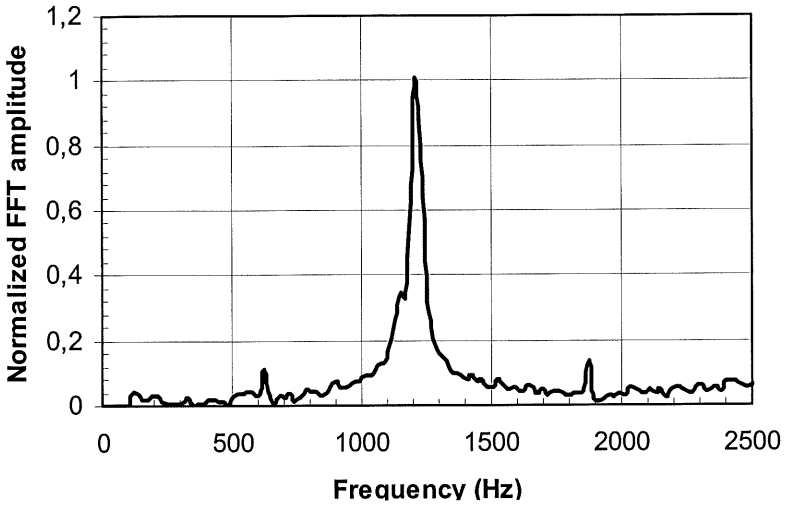

(a)

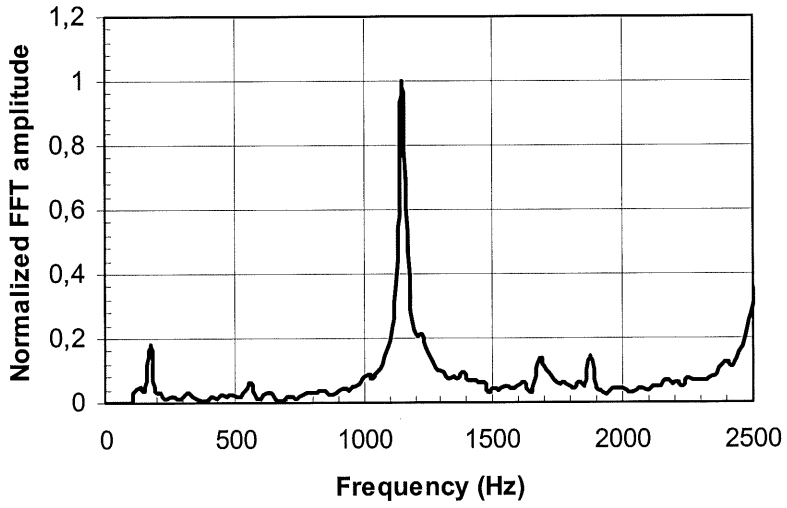

(b)

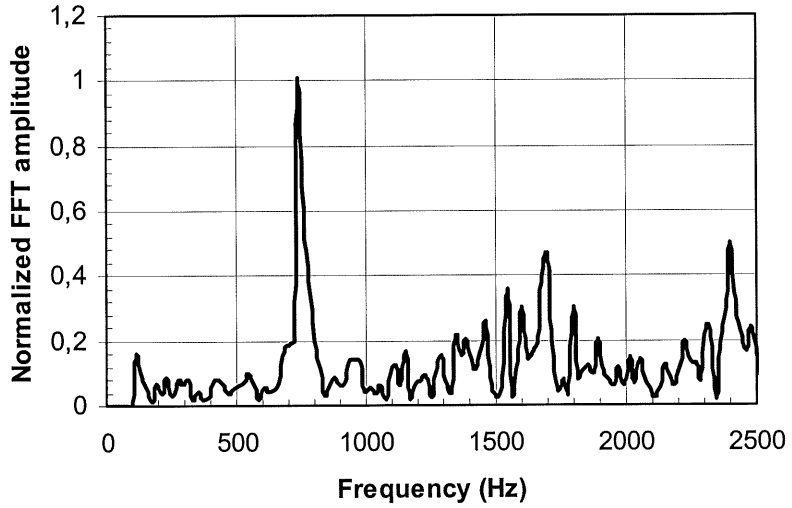

(c)

Figure 6.4 Change in resonant frequencies with fatigue cycles, after one million cycles; (a) longitudinal, (b) transverse and (c) torsion

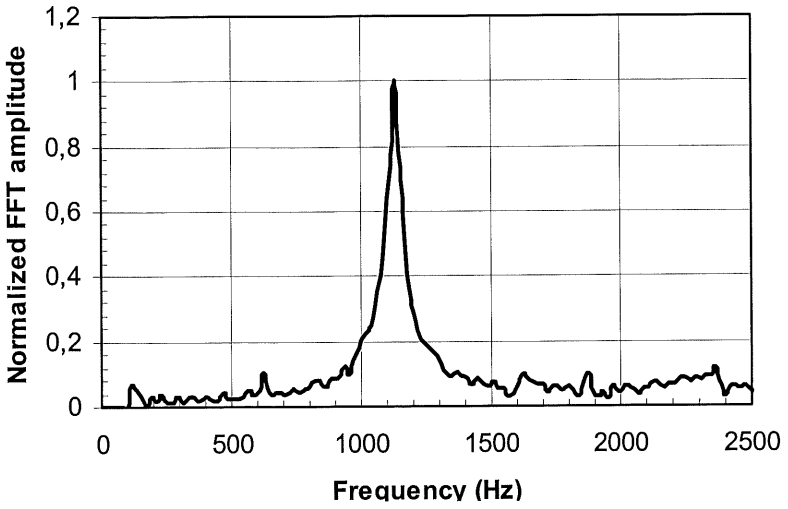

(a)

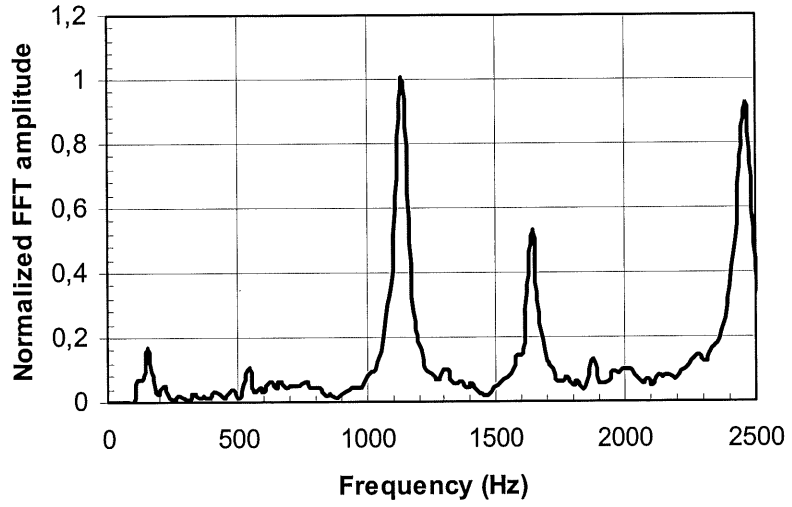

(b)

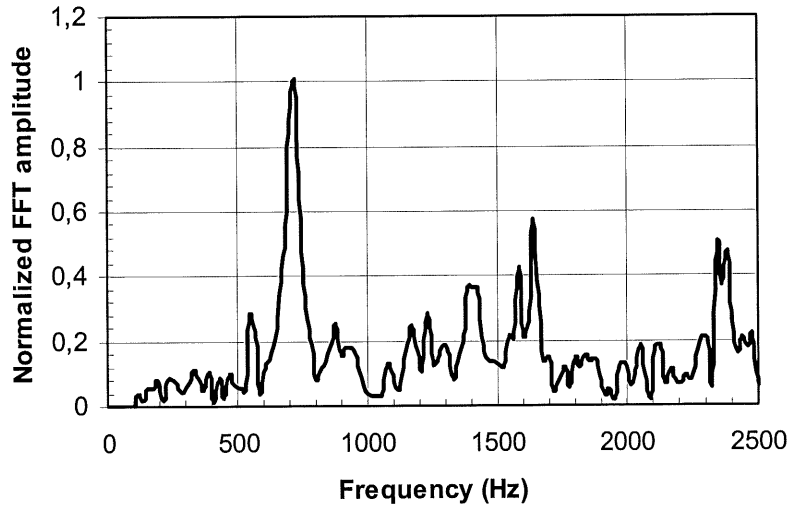

(c)

Figure 6.5 Change in resonant frequencies with fatigue cycles, at the end of the two million cycle test; (a) longitudinal, (b) transverse and (c) torsion

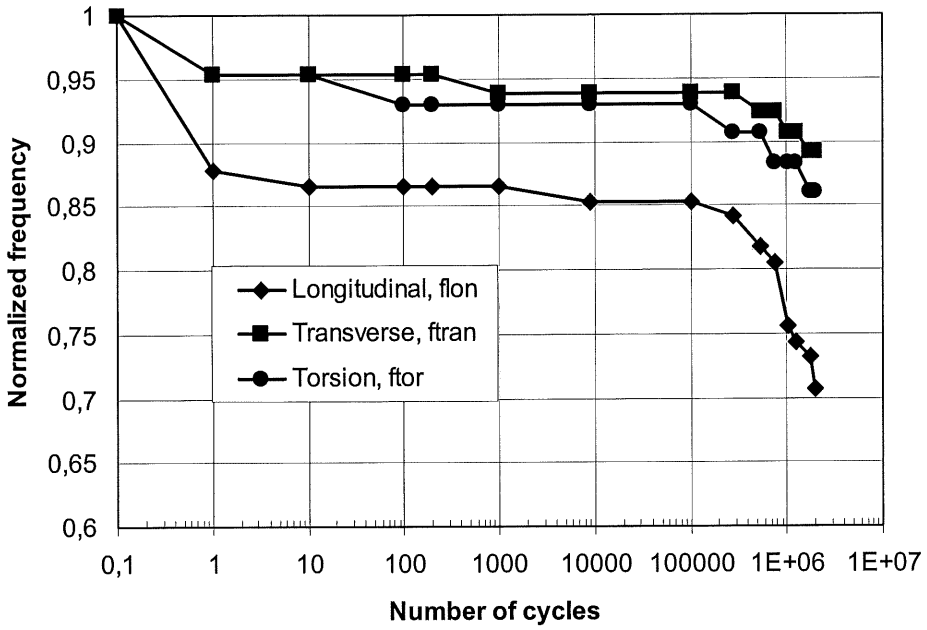

Figure 6.6 Normalized frequencies versus the number of cycles

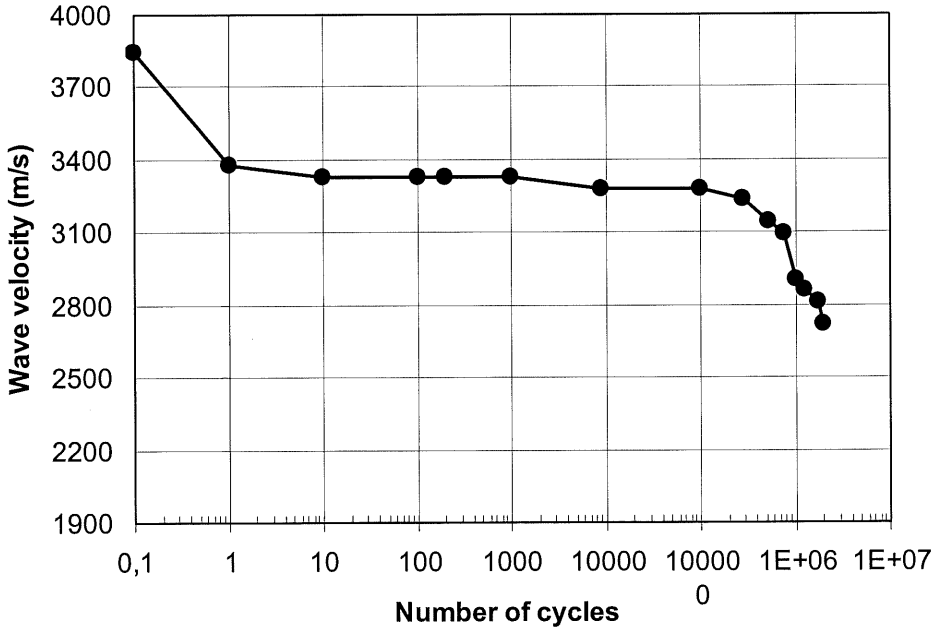

Figure 6.7 Wave velocity in concrete versus the number of cycles

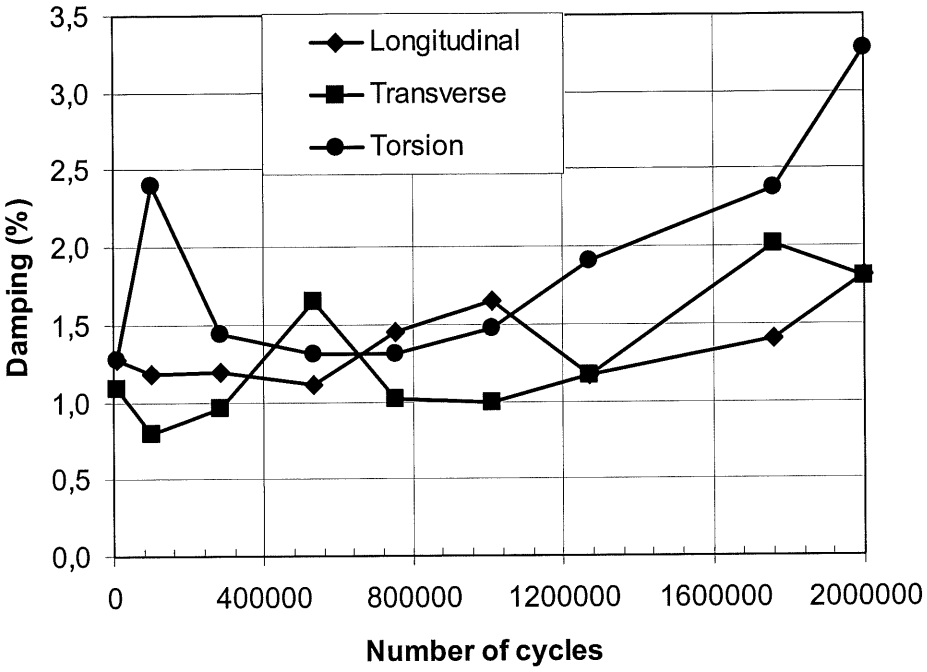

Figure 6.8 Modal damping ratio versus number of cycles

CONCLUSION

CONCLUSION

This thesis contributes to the evolving multidisciplinary field of intelligent sensing for innovative structures. It is a continuation of the work conducted by the ISIS Sherbrooke research group, in view of the integration of fibre optic sensors in the composite materials used to strengthen transportation infrastructure. These structures integrated with a sensing system would continuously be monitored for their structural health and safety. The use of an integrated sensing system in conjunction with non-destructive evaluation could reveal the performance of various structural components during construction, in service and under exceptional loading conditions, possibly leading to improved design, quality control and eventually mitigating disasters. The large amount of research conducted in the smart structures interdisciplinary field has intensified in the last decades to show the increasing interest in FOS monitoring and non-destructive evaluation techniques for civil engineering structures.

The originality of the work presented here stands in the fact that it is the first experimental program on the durability of FOS installed on a structural member submitted to various environmental and/or loading conditions. In addition, a non-destructive testing technique was employed for the first time to monitor fatigue damage for this type of specimen. From the research work conducted in this study, conclusions can be drawn regarding the following three aspects: the durability of the fibre optic sensors installed on the beam structure; the durability of two strengthening schemes used to externally strengthen concrete beams; and the applicability of the impact resonance method to detect fatigue damage in CFRP-strengthened beams.

Durability of the fibre optic sensors

The fatigue tests on the fibre optic sensors used to instrument RC beams were followed by a quasi-static test to failure. Some instrumented beams were also exposed to water prior to initiation of the fatigue load. These results have shown the following:

- throughout the duration of the study, there was a marked increase in reliability and accuracy of the FOS. For instance, the sensors purchased after 2000 performed better than those purchased previously;

- the maximum error observed for sensors purchased after 2000 is 5%;
- for the same sensors, the amplitude and the number of fatigue cycles had no influence on the readings provided that the strains were smaller than 3300 με;
- the water exposures seemed to seriously affect the FOS bond to the support structure;
- the strain readings showed drops during the quasi-static tests starting with 3200 με;
- the FOS purchased after 2000 accurately measured quasi-static strains to failure after the fatigue cycling.

The poor performance of the sensors when immersed in water does not necessarily mean that they should be rejected. It was mentioned that these sensors were purchased before 2000 and part of the errors may come from the sensor itself. Also, they were submitted to water exposure not frequent in actual structures. To alleviate the water sensitivity, measurements must be taken to improve their protection against moisture. Alternatively, an adhesive with good resistance to water may be used to improve the installation of the sensors.

Durability of beams strengthened with CFRP

The durability of the beams strengthened with two CFRP systems was tested through fatigue cycles and/or water exposures prior to the quasi-static test to failure. The two carbon fibre systems used to reinforce the beams were CarboDur and Replark. The former consists pultruded plates, and the latter is made of sheets. The water exposures consisted of wet-dry cycles or continuous immersion in either ordinary or saltwater. Some beams were tested in fatigue after the water exposures. The fatigue load was applied with two load ranges: low-level and high-level cycling. The numbers of cycles during the fatigue load were: 400 000, 800 000 and 2 000 000 cycles.

The results obtained on the beams in Series I strengthened with two CFRP systems, exposed to water tested with low-level cycling, and finally loaded to failure showed that:

- the plate system behaves very differently from the sheets system;
- a minimum damage was observed during fatigue loading;
- the CarboDur-plated beams showed a consistent response during fatigue cycling independent of the prior exposure conditions;

- the beams reinforced with Replark sheets showed a large variability in their strain fatigue responses;
- the wet-dry exposure and continuous immersion to water did not alter the fatigue response of the beams;
- the stress transfer at the CFRP-concrete interface seemed to be affected by the water exposures when the quasi-static load is applied after the combined effects of fatigue and water exposure;
- the ultimate load and deflection was not influenced by the water exposures;
- ISIS design equations are conservative for the Replark sheets system, but predict higher ultimate loads than measured for the CarboDur plate system;
- the Replark sheet system increased the deformability of the reinforced concrete beam whereas the CarboDur system decreased it;
- no adverse effects of saltwater versus ordinary water were found for this series of tests.

The results obtained for Series II beams strengthened with CarboDur plates and submitted to three numbers of fatigue cycles with two load ranges showed that:

- for both low-level and high-level cycling, the stiffness of the beams decreased with the increasing number of cycles;
- for low-level cycling, increasing number of cycles did not significantly deteriorate the CFRP-concrete interface;
- the CFRP-concrete interface was deteriorated more for high-level fatigued beams than for the low-level cycled ones;
- the fatigue cycles had no influence on the residual strength of the beams;

These observations show that the CFRP systems used increase the fatigue and post-fatigue performance of the reinforced concrete beams. The fact that the two systems have different behaviours is not an impediment to using them efficiently but rather an advantage. The plate system could be used in applications where high stiffness and low deformability are required. The sheet system could be used in applications where high deformability is a must. Although the ISIS design equations predicted higher ultimate capacities for the plate system, they can still be considered conservative for the following reason. The CarboDur-plated beams were on

purpose designed to fail by delamination, whereas the equations assumed the concrete crushing failure mode.

Impact resonance method for fatigue damage detection

The IRM technique can be used for monitoring dynamic characteristic changes in structural members such as RC beams. The tests on all the beams in Series II showed that:

- the modal frequencies for the CFRP-strengthened beams can be identified with very good accuracy throughout the fatigue test using the IRM technique;
- the three resonance frequencies can be well correlated with the severity of damage; that is, the larger the extent of damage the smaller the vibration frequency;
- when loaded in bending, the maximum decrease in frequency is observed for the longitudinal mode;
- the damping ratios seem to increase with the number of cycles for the same loading conditions;
- the damping ratios are higher for the transverse and torsion modes than for the longitudinal one, for this loading configuration;
- their values range from 0.6-1.3% for the undamaged beam, to up to 3.2% after the fatigue cycling;
- the number of secondary peaks in FFT curves increases with cycling;
- the increasing load range used caused an increase in the extent of damage that is reflected in a decrease in natural frequencies;

Future work

The tests conducted in this study with the FOS results presented in chapter 5 included a number of parameters such as: support CFRP material; water exposure, static loading, fatigue loading, and post-fatigue static loading. It would be interesting to study the influence on FOS readings of several other parameters, such as:

- exposure to freeze-thaw cycles;
- improvement of the environmental protection;
- trials with different adhesives to improve resistance at water exposures;

The IRM test results presented in chapter 6 showed the potential of this technique in the damage detection and evaluation of structures. However, a limited number of beams were IRM tested and only one specimen was dynamically monitored throughout the fatigue test. Another parameter that needs attention is the load range applied during the fatigue cycling. It would be also interesting to monitor the frequency changes during a static test. Additional tests would clarify several key aspects such as:

- how to improve the exactness of the damping ratios;
- how to identify the extent of damage and location from the secondary peaks in the FFT curves;
- how to correlate the change in natural frequencies with the number and the amplitude of fatigue cycles.

Both FOS measurements and IRM tests give information on the state of the structure. A sudden change in strain values could be a warning for an exceptional load on the structure or a decrease in its performance. The change in dynamic features of a structure could be related to a modification in its environmental and boundary conditions, as well as a damage indicator. FOS continuous monitoring could be consequently used in conjunction with IRM periodical testing to better define the health of any structural element.

REFERENCES

Aktan, A.E., Helmicki, A.J. and Hunt, V.J. (1998). Issues in health monitoring for intelligent infrastructure, *Smart Materials and Structures*, 7, 674–692.

Akhavan, F., Watkins, S.E. and Chandrashekhara, K. (1998). Measurement analysis of impact-induced strain using extrinsic Fabry-Perot fibre optic sensors, *Smart Materials and Structures*, 7, 745-751.

Allbright, K., Parekh, K.R., Miller, R. and Baseheart, T.M. (1994). Modal verification of a destructive test of damaged prestressed concrete beam, *Experimental Mechanics*, 389–396.

Ambrosini, D., Luccioni, B. and Danesi, R. (2000). Theoretical-experimental damage determination in prestressed concrete beams, *NDT.net*, 5(7), http://www.ndt.net/article/v05n07

ASTM C215-97, (1998). Standard test method for fundamental transverse, longitudinal, and torsion resonant frequencies of concrete specimens, *ASTM*, 119–124.

Bakis, C.E., Bank, L.C., Brown V.L., Cosenza, E., Davalos, J.F., Lesko, J.J., Machida, A. Riskalla, S.H. and Triantafillou, T.C. (2002). Fibre-reinforced polymer composites for construction-State-of-the-art review, *Journal of Composites for Construction*, ASCE, 6(2), 73–87.

Barnes, R.A. and Mays, G.C. (1999). Fatigue performance of concrete beams strengthened with CFRP plates, *Journal of Composites for Construction*, ASCE, 3(2), 63–72.

Beaudoin, Y., Labossière, P. and Neale, K.W. (1998). Wet-dry action on the bond between composite materials and reinforced concrete beams, *1st International Conference on Durability of Fibre Reinforced Polymer (FRP) Composites for Construction*, Benmokrane B. and Rahman H., eds., Sherbrooke, Canada, 537–546.

Benmokrane, B., Rahman, H., Muchopadhyaya, P., Masmoudi, R., Zhang, B., Lord, I. and Tadros, G. (2001). Fibre-optic sensors to monitor FRP-reinforced bridge, *ACI Concrete International*, 23(6), 33–38.

Bizindavyi, L. and Neale, K.W. (1999). Transfer lengths and bond strengths for composites bonded to concrete. *Journal of Composites for Construction*, ASCE, 3(4), 153–160.

Bizindavyi, L., Neale, K. W. and Erki, M. A. (2003). Experimental investigation of bonded fiber reinforced polymer-concrete joints under cyclic loading, *Journal of Composites for Construction*, ASCE, 7(4), 127–134.

Bonacci, J.F. and Maalej, M (2001). Behavioral trends of RC beams strengthened with externally bonded FRP, *Journal of Composites for Construction*, ASCE, 5(2), 102–113.

Brena, S.F., Wood, S.L. and Kreger, M.E. (2002). Fatigue tests of reinforced concrete beams strengthened using carbon fibre reinforced polymer composites, *Proceedings of the Second International Conference on Durability of Fibre Reinforced Polymer (FRP) Composites for Construction*, Benmokrane B. and El-Salakawy E., Editors, Montreal, Canada, 575–586.

Campbell, R. (3 March 1995), A True Tall Tale About the Hancock Tower, *Boston Globe*: 29 &34.

Chajes, M.J., Mertz, R., Thomson, T.A. and Farschman, C.A. (1994). Durability of composite material reinforcement. *Proceedings of the Third Materials Engineering Conference*, San-Diego, California, 598–605.

Cheng, C.C. and Sansalone, M. (1995). Determining the minimum crack width that can be detected using the impact-echo method. Part 1: Experimental study. *Materials and Structures*, RILEM, 28(176), 74–82.

Chong, K.P. (1998). Health monitoring of civil structures, *Journal of Intelligent Material Systems and Structures,* 6, 892–898.

Choquet, P., Juneau, F. and Bessette, J. (2000). New generation of Fabry-Perot fibre optic sensors for monitoring structures. *Proceedings of SPIE's 7th Annual International Symposium on Smart Structures and Materials*, Newport Beach, California.

Clough, R.W. and Penzien, J. (1993). Dynamics of structures, 2nd Edition, McGraw-Hill.

Cornwell, P.J., Farrar, C.R., Doebling, SW. and Sohn, H. (1999). Structural testing series: Part 4 - Environmental variability of modal properties, *Experimental Techniques*, 23(6), 45–48.

CSA-A23.3 (1994). Design of concrete structures. Canadian Standards Association, Rexdale, Ontario.

Darwish, M.N. and Darwish, A.N. (2002). Smart structures for the future, *IABSE Symposium,* Melbourne, Australia, CD-ROM.

DeMerchant M., Brown, A., Smith, J., Bao, X. and Bremer, T. (2000). Distributed strain sensing for structural monitoring applications, *Canadian Journal of Civil Engineering*, CSCE, 27, 873–879.

de Vries, M., Nasta, M., Bhatia, V., Tran, T., Greene, J., Claus, R.O. and Masri, S. (1995). Performance of embedded short-gage-length optical fibre sensors in a fatigue-loaded reinforced concrete specimen, *Smart Materials and Structures*, 4, A107–A113.

Doebling, S.W., Farrar, C.R. and Prime, M.B. (1998). A summary review of vibration-based damage identification methods. *Shock and Vibration Digest*, Sage Publications, 30(2), 91–105.

EMPA (1999). Sika CarboDur structural strengthening systems, Fatigue and failure test-beams B1 and B2, Report-No. 402'017E/2, Dubendorf, Switzerland.

Escobar J.A., Sosa J.J., and Gomez, R. (2001). Damage detection in framed buildings, *Canadian Journal of Civil Engineering*, 28, 35–47.

Farrar, C.R. and Doebling, S.W. (1999). Damage detection and evaluation II - Field applications to large structures. *NATO ASI Series E Applied Sciences*, Kluwer Academic Publishers, 363, 345–378.

FISO Technologies Inc. (2003). Fibre optic strain gauges: www.fiso.com

Feng, M.Q. and Bahng, E.Y., (1999). Damage assessment of jacketed RC columns using vibration tests, *Journal of Structural Engineering,* 125(3), 265–271.

Fritzen, C.P. and Bohle, K. (2001). Application of model-based identification to seismically loaded structure, *Smart Materials and Structures*, 10, 452–458.

Fuhr, P.L (August 1995). Fiber-optic sensors in smart civil structures, *Sensors,* 18–25.

Fujino, Y. and Abe, M. (2001). Structural health monitoring of civil infrastructures R&D of SHM of bridges at the University of Tokyo, *Proceedings of the 3rd International Workshop on Structural Health Monitoring: The Demands and Challenges*, Stanford, California.

Galea, S.C., Rajic, N., Powlesland, I.G., Moss, S., Konak, M.J., Van der Velden, S. and Baker, A.A. (2001). Overview of DSTO smart structures activities related to structural health monitoring, *International Conference on Health and Usage Monitoring*, DSTO, Melbourne, Australia.

Gheorghiu, C., Labossière, P. and Raîche, A. (2003). Environmental fatigue and static behaviour RC beams strengthened with CFRP, *Journal of Composites for Construction,* ASCE, (in print).

Green, M.F., Bisby, L.A., Beaudoin, Y., and Labossière, P. (2000). Effect of freeze-thaw cycles on the bond durability between fibre reinforced polymer plate reinforcement and concrete. *Canadian Journal of Civil Engineering*, 27(5), 949–959.

Halling, M.W., Muhammad, I. and Womack, K.C. (2001). Dynamic field testing for condition assessment of bridge bents, *Journal of Structural Engineering,* ASCE, 127(2), 161–167.

Heffernan, P.J. and Erki, M.A. (1996). Equivalent capacity and efficiency of reinforced concrete beams strengthened with carbon fibre reinforced plastic sheets, *Canadian Journal of Civil Engineering*, 23, 21–29.

Heffernan, P.J. (1997). Fatigue behaviour of reinforced concrete beams strengthened with CFRP laminates, Ph.D. Thesis, Royal Military College of Canada, Kingston, Ontario.

Huston, D.R., Fuhr, P.L., Ambrose, T.P. and Barker, D.A. (1994). Intelligent civil structures-activities in Vermont, *Smart Materials and Structures*, 3, 129–139.

Inaudi, D., Casanova, N. and Glisic, B. (2001). Long-term deformation monitoring of historical constructions with fiber optic sensors, *3rd International Seminar on Structural Analysis of historical Constructions,* Guimaraes, Portugal.

ISIS Canada (2001a). Guidelines for structural health monitoring (Design manual). *The Canadian Network of Centres of Excellence on Intelligent Sensing for Innovative Structures*, Winnipeg, Canada.

ISIS Canada (2001b). Strengthening reinforced concrete structures with externally-bonded fibre reinforced polymers (Design manual). *The Canadian Network of Centres of Excellence on Intelligent Sensing for Innovative Structures*, Winnipeg, Canada.

ISIS Canada (2001c). Installation, use and repair of fibre optic sensors (Design manual). *The Canadian Network of Centres of Excellence on Intelligent Sensing for Innovative Structures*, Winnipeg, Canada.

Jin, X. and Li, Z. (2001). Dynamic property determination for early-age concrete, *ACI Materials Journal* 98(5), 365-370.

Kalamkarov, A. L. (2000). Reliability assessment of pultruded FRP reinforcements with embedded fibre optic sensors, *Composite Structures*, 50(1), 69–78

Kharbari, V.M. and Sikorsky, C. (2002). Field validation and monitoring of bridge renewal using FRP composites, *IABSE Symposium,* Melbourne, Australia, CD-ROM.

Kitagawa, Y. and Midorikawa, M. (1998). Seismic isolation and passive response-control buildings in Japan, *Smart Materials and Structures*, 5, 196–208.

Kitamura, H., Tamura, Y. and Ohkuma, T. (1995). Wind Resistant Design & Response Control in Japan Part III: Structural Damping & Response Control, *Proceedings of 5th World Congress Council on Tall Buildings and Urban Habitat,* Amsterdam, Holland.

Kwok, K.C.S., and Samali, B. (1995). Performance of tuned mass dampers under wind loads, *Engineering Structures,* Elsevier, 17(9): 655-667.

Labossière, P., Neale, K. W., Rochette, P., Demers, M., Lamothe, P., Lapierre, P. and Desgagné, G. (2000). Fibre reinforced polymer strengthening of the Sainte-Émélie-de-l'Énergie bridge: design, instrumentation, and field testing, *Canadian Journal of Civil Engineering*, CSCE, 27, 916–927.

Laura, P.A.A., La Malfa, S. and Bambill, D.V. (1998). Monitoring structural health through changes in frequency, *Journal of Sound and Vibration*, 212(5), 909–911.

Lin, Y. and Lin, K.L. (1997). Transient impact response of bridge I-girders with and without flaws, *Journal of Bridge Engineering*, 2(4), 131–138.

Lin, Y. and Sansalone, M. (1992). Detecting flaws in concrete beams and columns using the impact-echo method, *ACI Materials Journal,* 89(4).

Lin, J.M. and Sansalone, M. (1993). The transient response of hollow cylindrical structures subjected to transverse elastic impact, *Journal of Nondestructive Evaluation,* 12(2).

Lopez, M.D.M., Naanan, A.E. and Till, R.D. (1999). Bending behaviour of reinforced concrete beams strengthened with carbon fibre reinforced polymer laminates and subjected to freeze-thaw cycles. *Proceedings of the Fourth International Symposium on Fiber Reinforced Polymer (FRP) for Reinforced Concrete Structures (FRPRCS-4)*, C.W. Dolan, S.H. Rizkalla and A. Nanni, Editors, American Concrete Institute, 559–576

Lopez, M.D.M., Naanan, A.E., Pikerton, L. and Till, R.D. (2001). Behavior of RC beams strengthened with laminates and tested under cyclic loading at low temperatures, *Proceedings of the International Conference on FRP Composites in Civil Engineering*, J.G. Teng, Editor, Elsevier, Hong Kong, 415–422.

McKinley, B., Aarnes, K.A. and Boswell, L. (2002). Bridge monitoring using an optical fibre sensor system, *IABSE Symposium,* Melbourne, Australia, CD-ROM.

Measures, R.M., Alavie, A.T., Maaskant, R., Ohn, M., Karr, S. and Huang, S. (1995). A structurally integrated Bragg grating laser sensing system for a carbon fibre prestressed concrete highway bridge, *Smart Materials and Structures*, 4, 20–30.

Measures, R.M. (1996). Fibre optic sensor instrumented bridges... 21st century information highways, *Proceedings of the Conference on Advanced Composite Materials in Bridges and Structures*, M.M. El-Badry, Editor, CSCE, Montreal, 31–40.

Meier, U., Deuring, M., Meier, H. and Schwegler, G. (1992). Strengthening of structures with CFRP laminates: research and applications in Switzerland, *Proceedings of the Conference on Advanced Composite Materials in Bridges and Structures*, K.W. Neale and Labossière P., Editors, CSCE, Sherbrooke, 243–251.

Merzbacher, C.I., Kersey, A.D. and Friebele, E.J. (1996). Fibre optic sensors in concrete structures : a review, *Smart Materials and Structures*, 5, 196–208.

Mufti, A.A., Tadros, G. and Jones, P.R. (1997). Field assessment of fibre optic Bragg grating sensors in the Confederation Bridge, *Canadian Journal of Civil Engineering*, CSCE, 24, 963–966.

Mufti, A.A., Bakht, B., Newhook, J. and Jones, P.R. (1998). Salmon river bridge field assessment, *Bridge Monitoring and Evaluation Workshop*, Halifax.

Ndambi, J.M., Peeters, B., Maeck, J., De Visscher, J., Wahab, M.A., Vantomme, J., De Roeck, G. and De Wilde, W.P. (2000). Comparison of techniques for modal analysis of concrete structures, *Engineering Structures*, Elsevier, 22(9), 1159–1166.

Pandey, A.K. and Biswas, M. (1994). Damage detection in structures using changes in flexibility, *Journal of Sound and Vibration*, 169(1), 3–17.

Papakonstantinou, C.G., Petrou, M.F. and Harries, K.A. (2001). Fatigue behavior of RC beams strengthened with GFRP sheets, *Journal of Composites for Construction*, ASCE, 5(4), 246–253.

Paultre, P. and Proulx, J. (1995). Dynamic testing procedures for highway bridges using traffic loads, *Journal of Structural Engineering,* 121(2), 362–376.

Paultre, P. and Proulx, J. (1997). Dynamic testing of large-scale structures, *Structural Engineering International,* 1, 29–34.

Paultre, P., Proulx, J., Mousseau, S., Prévost, T. and Savard, C. (2001). Forced-vibration tests of a two-story reinforced concrete building submitted to pseudo-dynamic testing, *Concrete International.*

Peeters, B., Maeck, J. and De Roeck, G. (2001). Vibration-based detection in civil engineering: excitation sources and temperature effects, *Smart Materials and Structures*, 10, 518–527.

Petersen, N.R. (1980). Design of large scale tuned mass damper, *Structural Control,* North Holland, 581–596.

Popovics, S., Bilgutay, N.M, Karaoguz, M. and Akgul, T. (2000). High-frequency ultrasound technique for testing concrete, *ACI Materials Journal,* 97(1), 58–64.

Proulx, J. and Paultre, P. (1997). Experimental and numerical investigation of dam-reservoir-foundation interaction for a large gravity dam, *Canadian Journal of Civil Engineering*, CSCE, 24, 90–105.

Quirion, M. and Ballivy, G. (2000). Application des capteurs à fibre optique Fabry-Pérot pour le suivi à long terme de structures en béton, *Bulletin des Laboratoires des Ponts et Chaussées,* 225, 75–88.

Raîche, A., Beaudoin, Y. and Labossière, P. (1999). Durability of composite materials used as external reinforcement for RC beams. *Proceedings of the Annual Conference of the Canadian Society for Civil Engineering*, Regina, Canada, 155–164.

Razak, H.A. and Choi, F.C. (2001). The effect of corrosion on the natural frequency and modal damping of reinforced concrete beams, *Engineering Structures*, Elsevier, 23, 1126–1133.

Read, I.J. and Foote, P.D. (2001). Sea and flight trials of optical fibre Bragg grating strain sensing systems, *Smart Materials and Structures*, 10, 1085–1094.

Reinhorn, A., Soong, T.T., Helgeson, R.J., Riley, M.A. and Cao, H. (1998). Analysis, design and implementation of an active mass damper for a communication tower, *Proceedings of the Second World Conference on Structural Control,* Kyoto, Japan, 1727–1736.

Richards, W.L., Piazza, A., Hudson, L.D., Parker, A.R., Carman, G.P., Mitrovic, M., Lee , D. and Steward, A. (2001). Fibre optic sensor development for the structural health management of reusable launch vehicles, *Proceedings of the 3rd International Workshop on Structural Health Monitoring: The Demands and Challenges,* F.K. Chang and J.G. Guemes, Editors, Stanford, California, 133–143.

Rochette P., (2001). Capteurs à fibre optique intégrés à des matériaux composites pour le génie civil : essais et simulations sur éprouvettes cruciformes", *Doctorat ès sciences appliquées*, Université de Sherbrooke, Québec, Canada.

Rochette, P., Neale, K.W., Labossière, P. and Demers, M. (2002). Monitoring FRP-strengthened structures: lessons from applications in Quebec, *Proceedings of the First International Workshop on Structural Health Monitoring of Innovative Civil Engineering Structures*, A.A. Mufti, Editor, ISIS Canada Research Network, Winnipeg, Manitoba.

Roctest Ltd. (2000). Capteurs à fibre optique sensoptic, Jauge de deformation Fabry-Perot, Série FOS, *Manual d'instructions*, Roctest Ltd., St-Lambert, Quebec.

Saadatmanesh, H. and Ehsani, M.R. (1991). RC beams strengthened with GFRP plates. I: Experimental study, *Journal of Structural Engineering*, ASCE, 117(11), 3417–3433.

Salawu, O. S. (1997). Detection of structural damage through changes in frequency: a review, *Engineering Structures*, Elsevier, 19(9), 718–723.

Sansalone, M. (1997). Impact-echo: the complete story, *ACI Structural Journal* 94(6), 777-786.

Sansalone, M. and Carino, N.J. (March-April 1989). Detecting delaminations in reinforced concrete slabs with and without asphalt concrete overlays using the impact-echo method, *ACI Materials Journal,* 175–184.

Shahawy, M. and Beitelman, T.E. (1999). Static and fatigue performance of RC beams strengthened with CFRP laminates, *Journal of Structural Engineering*, ASCE, 125(6), 613–621.

Spillman, W.B., Sirkis, J.S. and Gardiner, P.T. (1996). Smart materials and structures: what are they?, *Smart Materials and Structures*, 5, 247–254.

Tennyson, R.C., Coroy, T., Duck, J., Manuelpillai, G., Mulvihill, P., Cooper, D.J.F., Smith, P.W.E., Mufti, A.A. and Jalali, S.J. (2000). Fibre optic sensors in civil engineering structures, *Canadian Journal of Civil Engineering*, CSCE, 27, 916–927.

Tennyson, R.C., Mufti, A.A., Rizkalla, S., Tadros, G. and Benmokrane, B. (2001). Structural health monitoring of innovative bridges in Canada with fibre optic sensors, *Smart Materials and Structures*, 10(3), 560–573.

Triantafillou, T.C. and Plevris, N (1992). Strengthening of RC beams with epoxy-bonded fibre-composite materials, *Materials and Structures,* 25, 201–211.

Udd, E., Editor (1995). Fiber optic smart structures, *Wiley-Interscience Publication*, John Wiley and Sons.

Whitmoyer, S.L. and Kim, Y. R. (1994). Determining asphalt concrete properties via the impact resonant method, *Journal of Testing & Evaluation*, ASTM , 22(2), 139–148.

Xie, M., Hoa, S.V. and Xiao, X.R. (1995). Bonding steel reinforced concrete with composites, *Journal of Reinforced Plastics in Composites*, Technomic Publishing Co., 14, 949-965.

APPENDIXES

APPENDIX A: TYPICAL LOAD-DEFLECTION CURVES

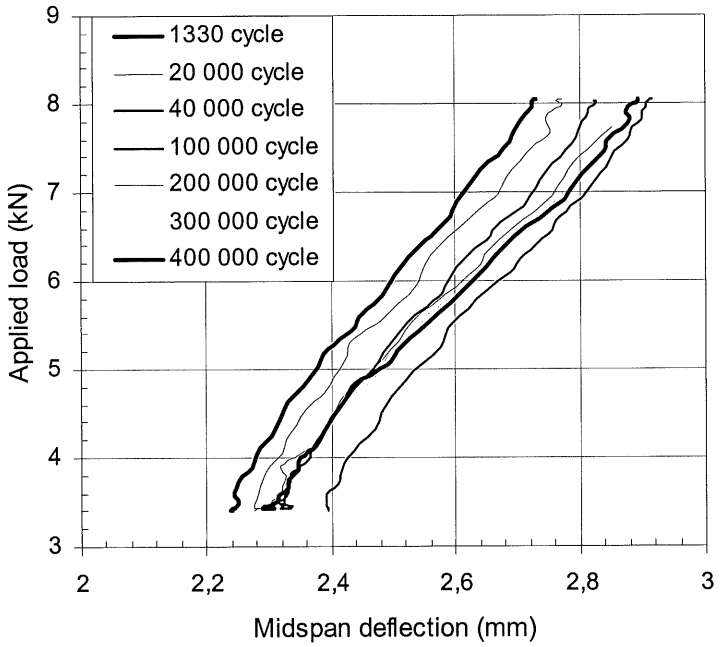

Figure A.1 Load-deflection curves for beam S0

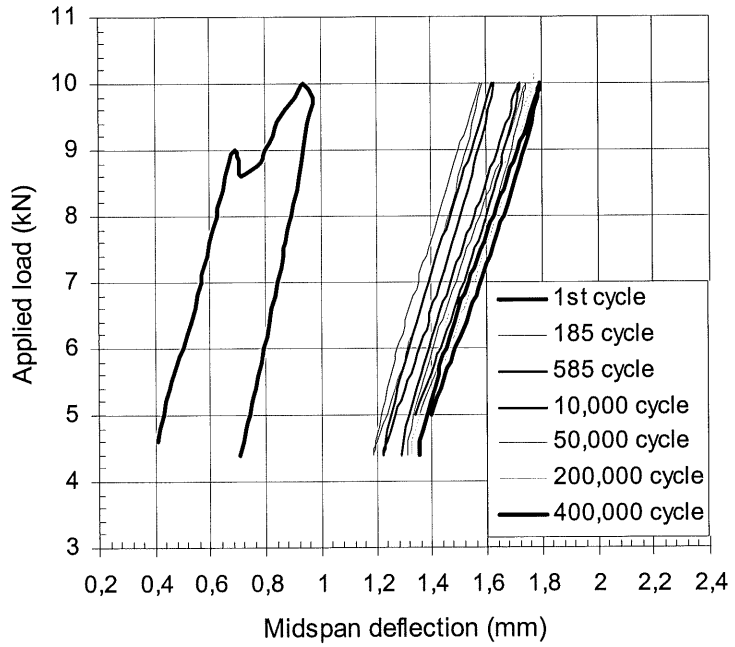

Figure A.2 Load-deflection curves for beam R2

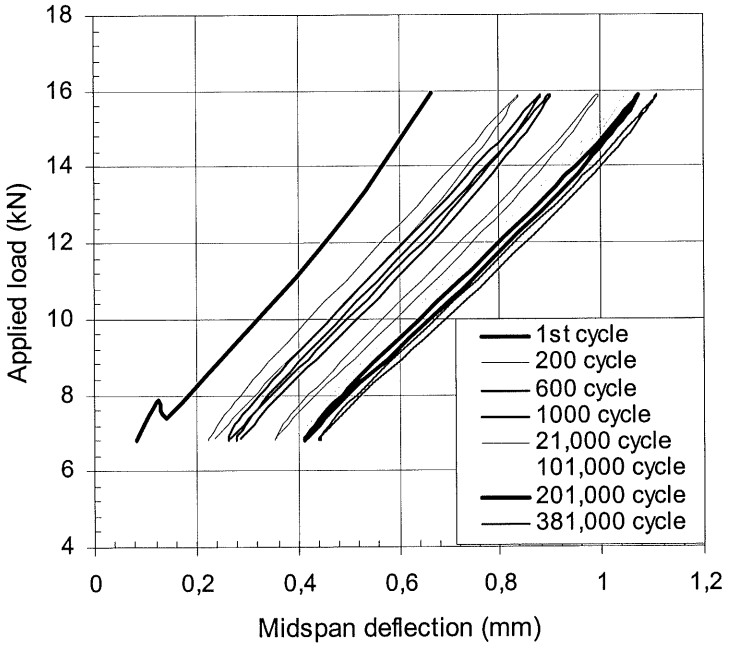

Figure A.3 Load-deflection curves for beam C1

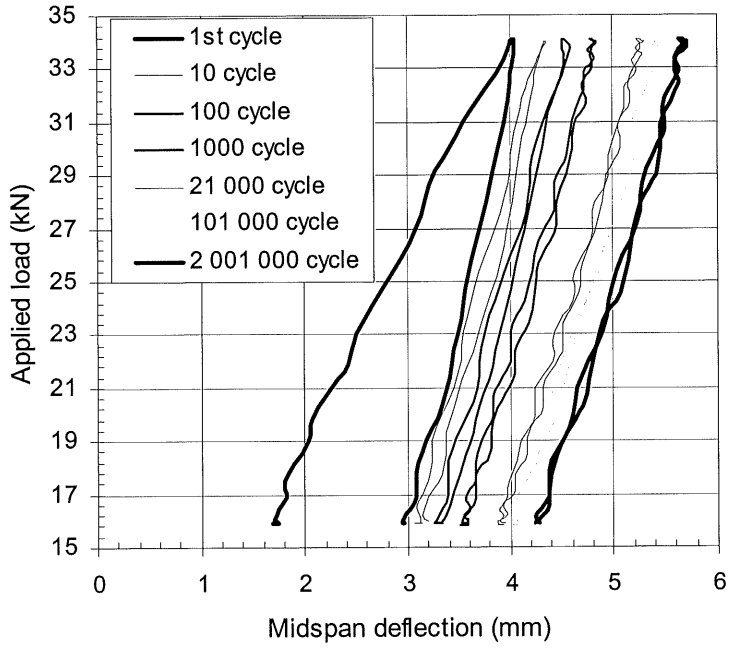

Figure A.4 Load-deflection curves for beam H2000B

APPENDIX B: EVOLUTION OF STRAIN CURVES, SERIES I

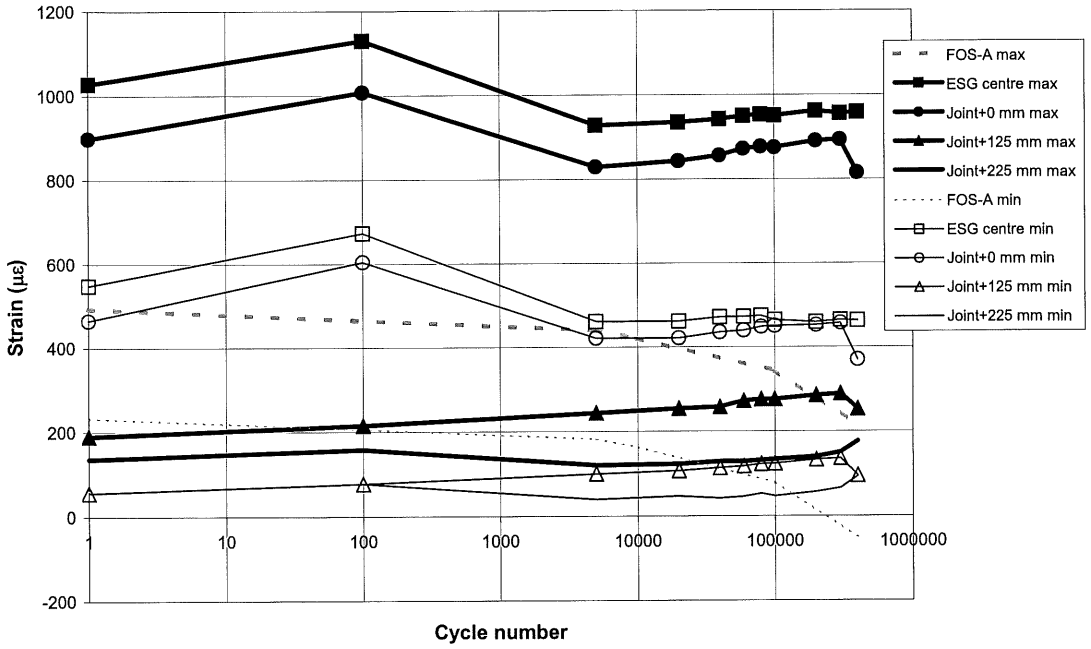

Figure B.1 Strain extreme curves for beam C2

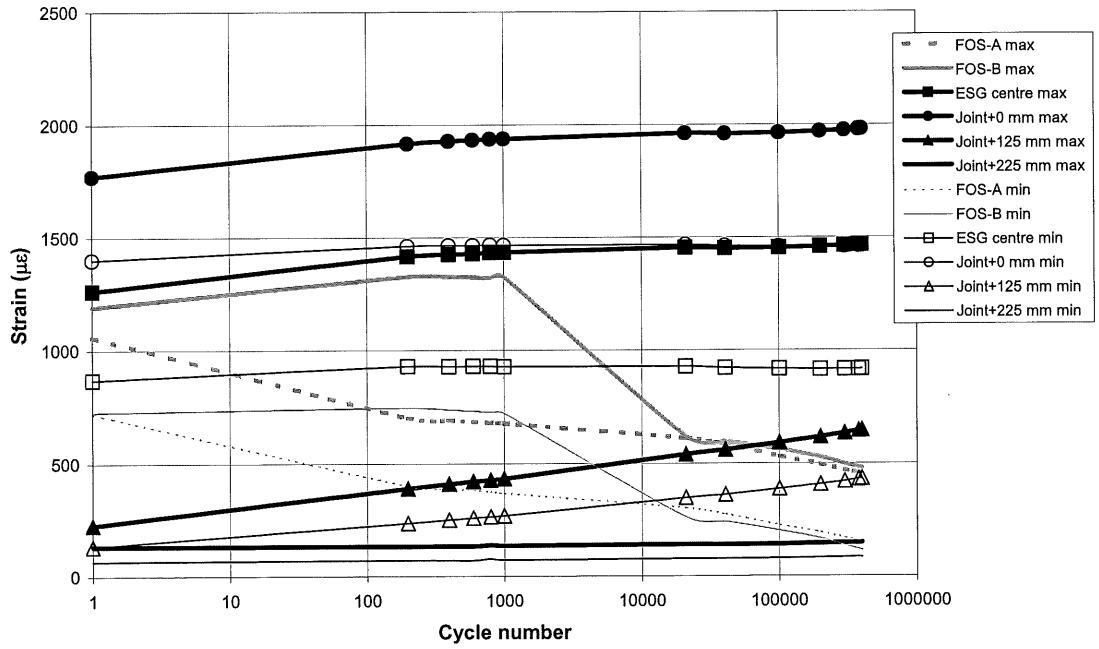

Figure B.2 Strain extreme curves for beam CW

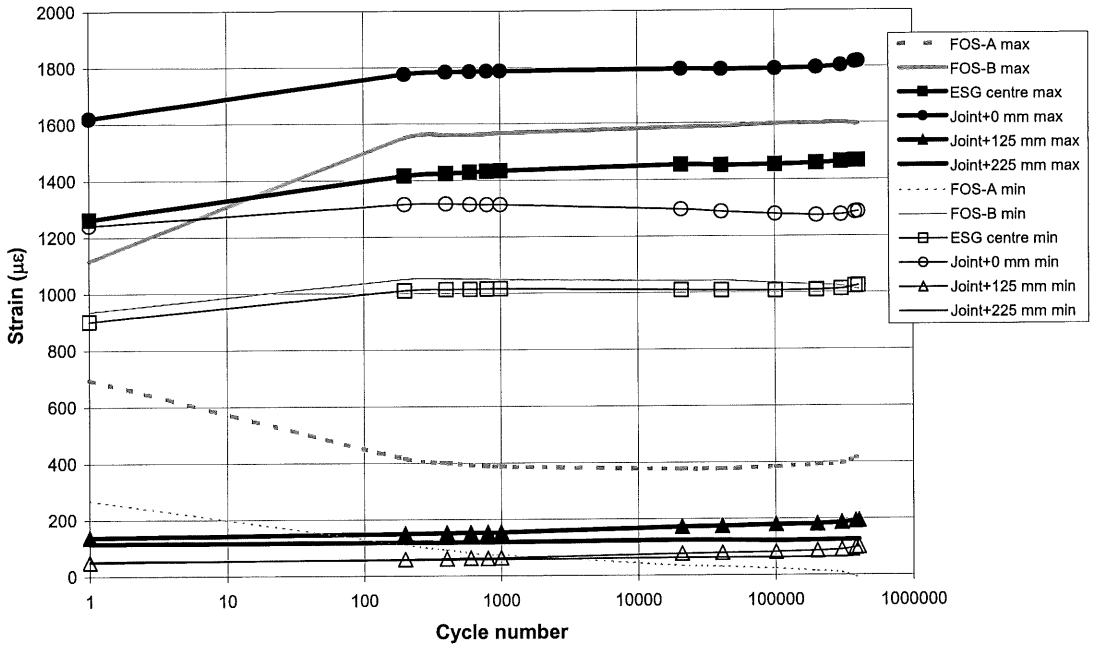

Figure B.3 Strain extreme curves for beam CI-S

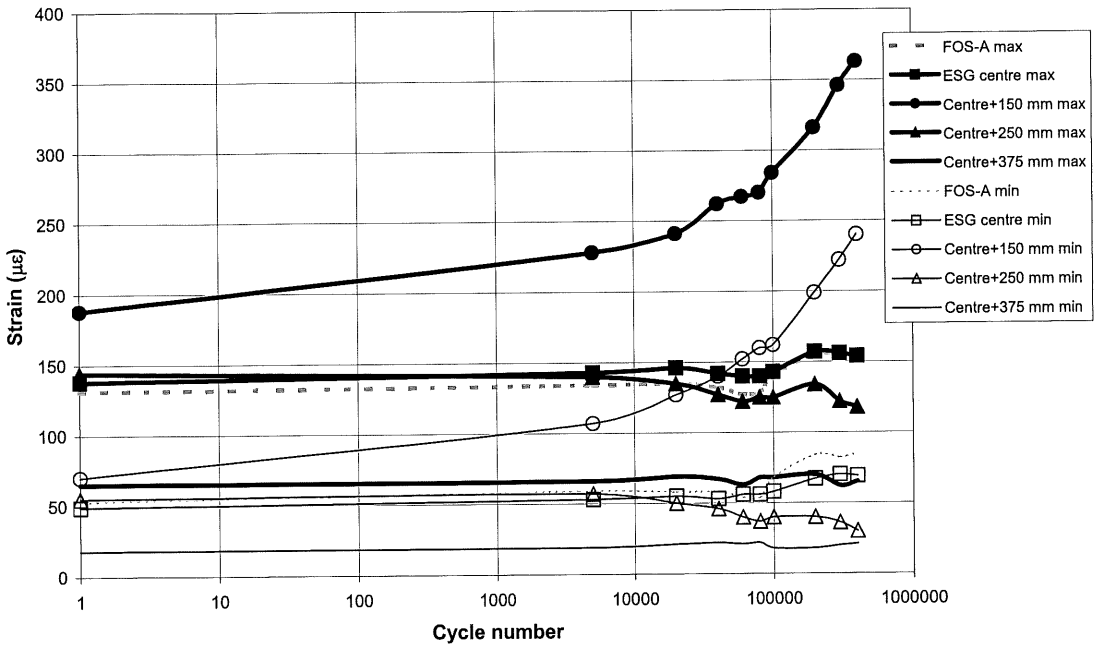

Figure B.4 Strain extreme curves for beam R1

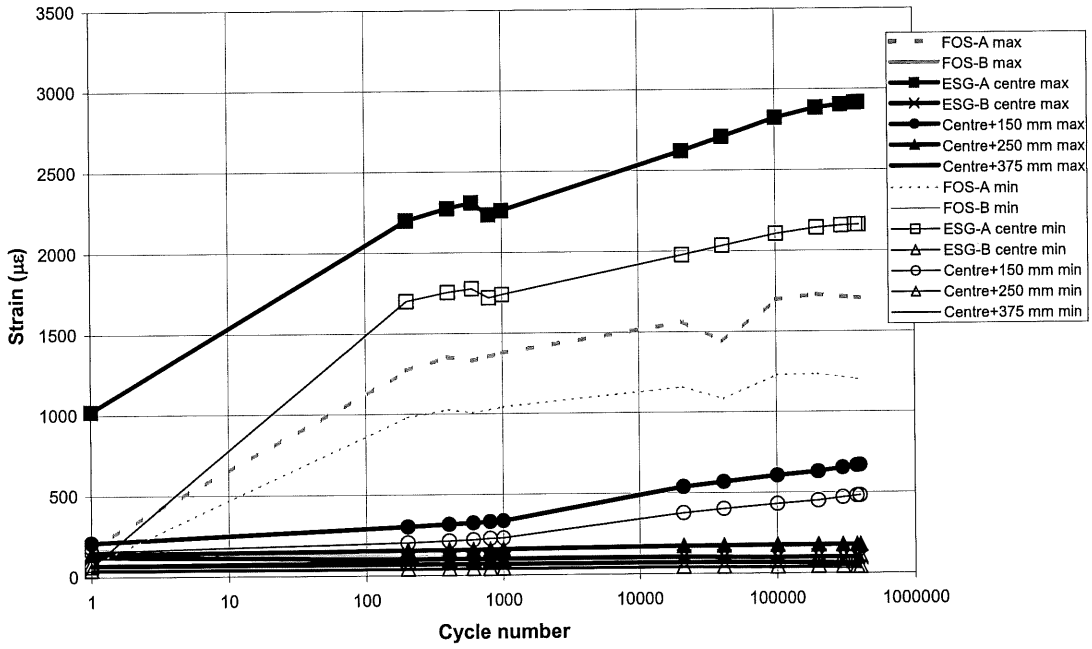

Figure B.5 Strain extreme curves for beam RW

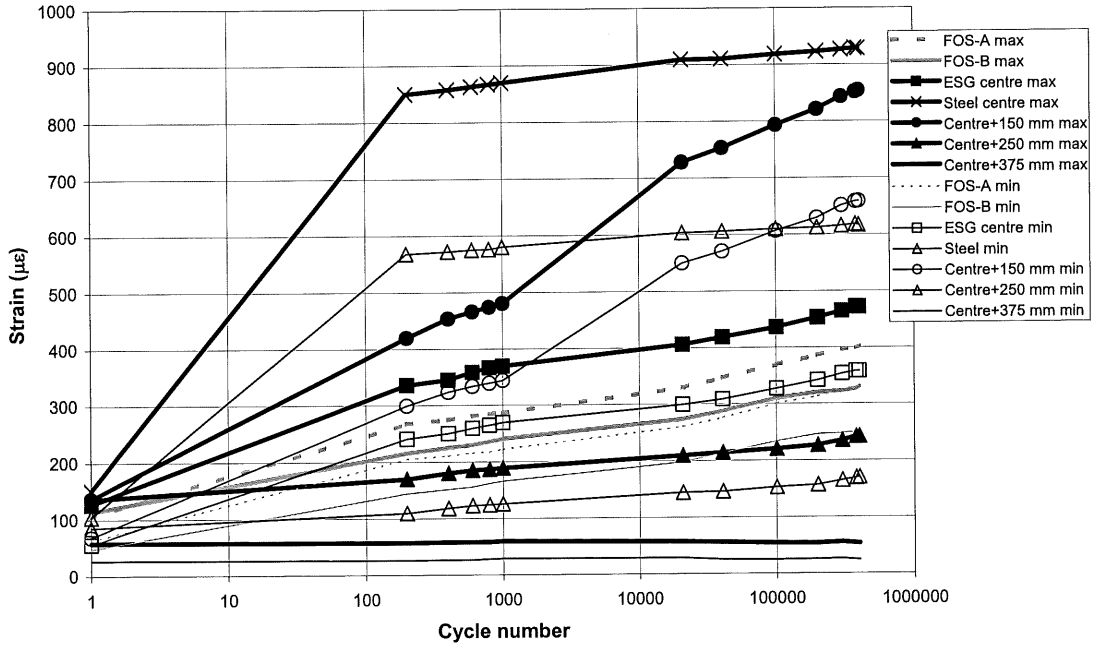

Figure B.6 Strain extreme curves for beam RI-S

APPENDIX C: INTERFACE SHEAR STRESS TRANSFER CURVES, SERIES I

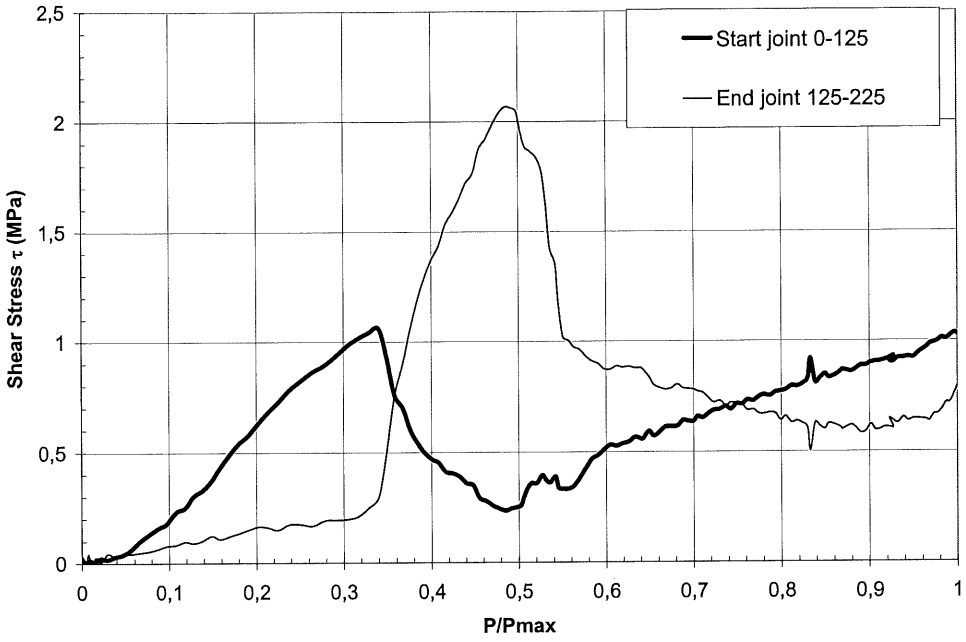

Figure C.1 Shear stress as a function of relative load for beam C2

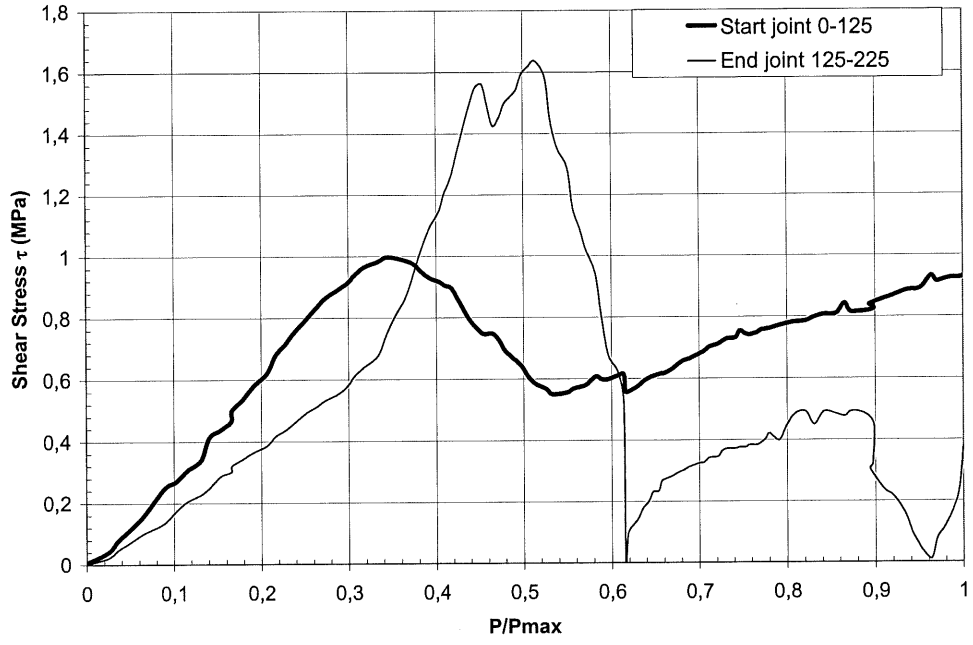

Figure C.2 Shear stress as a function of relative load for beam CW

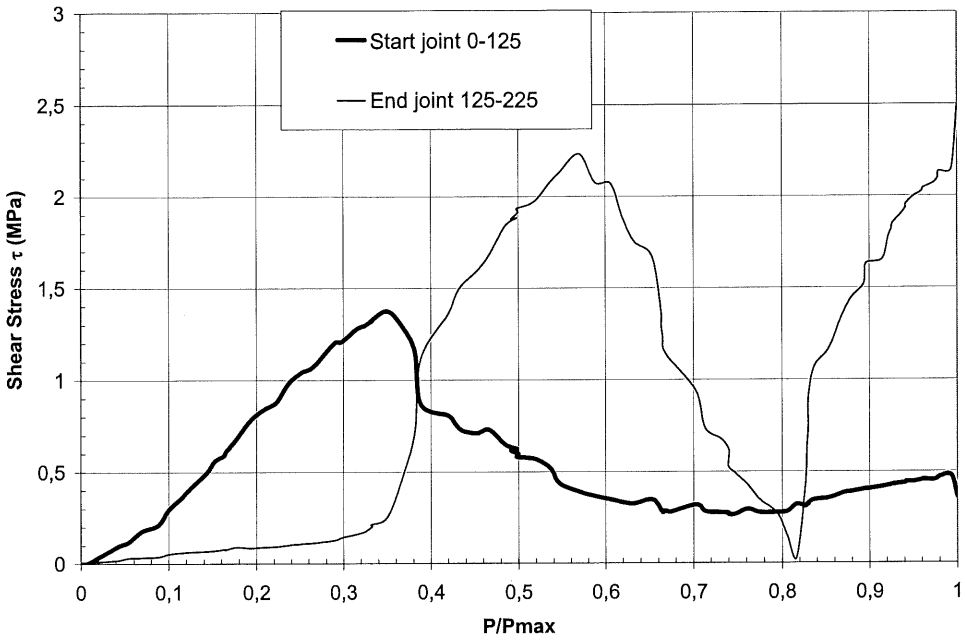

Figure C.3 Shear stress as a function of relative load for beam CI-S

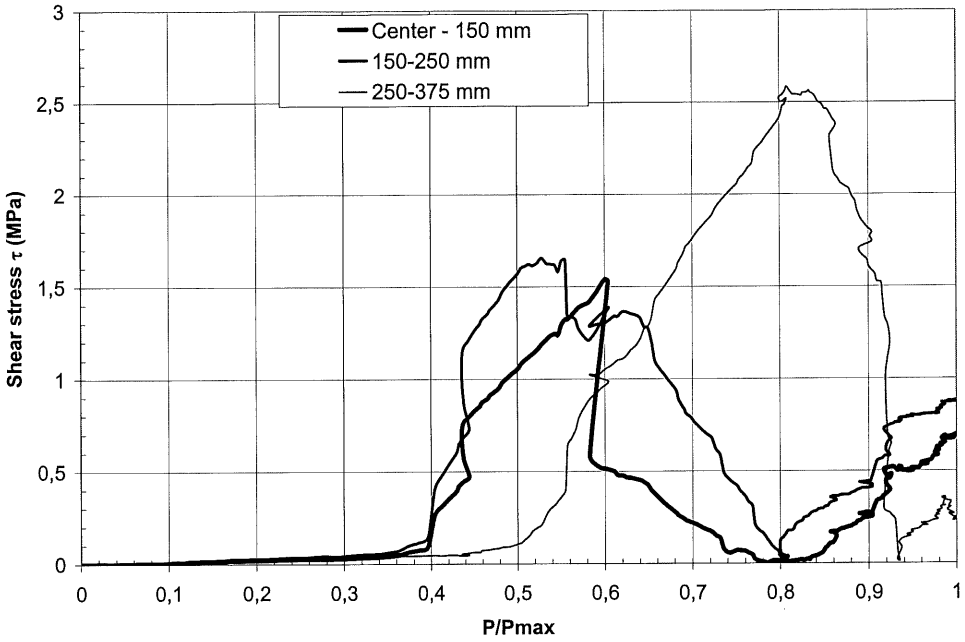

Figure C.4 Shear stress as a function of relative load for beam R1

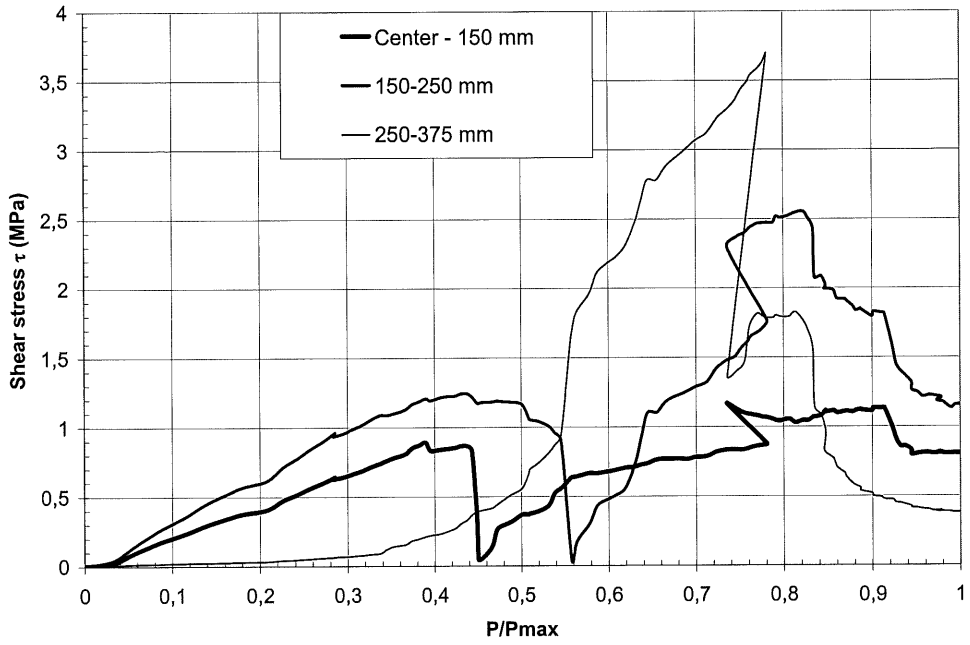

Figure C.5 Shear stress as a function of relative load for beam RW

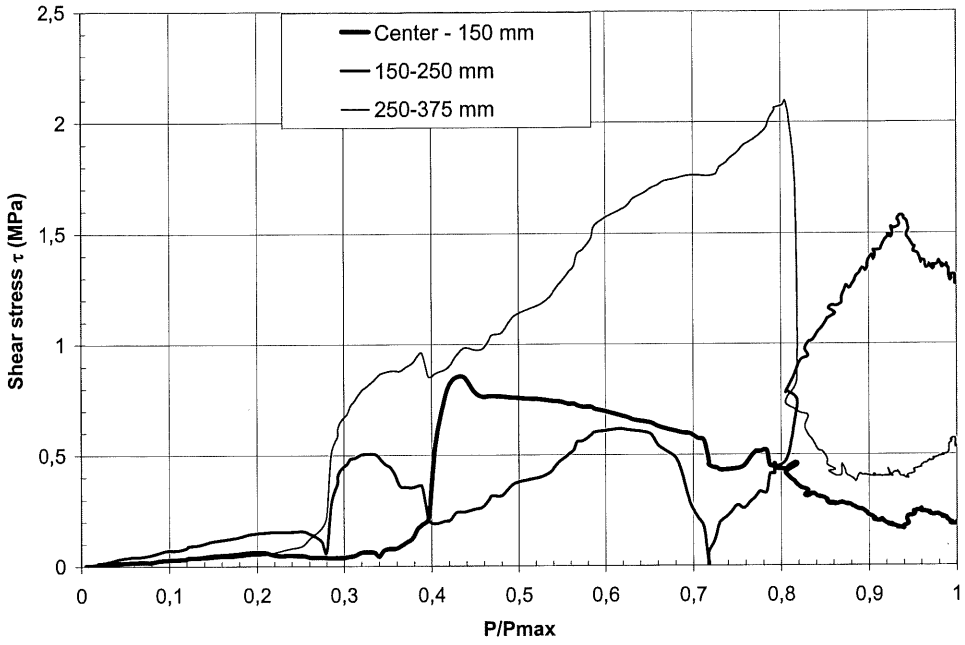

Figure C.6 Shear stress as a function of relative load for beam RI-S

APPENDIX D: EVOLUTION OF STRAIN CURVES, SERIES II

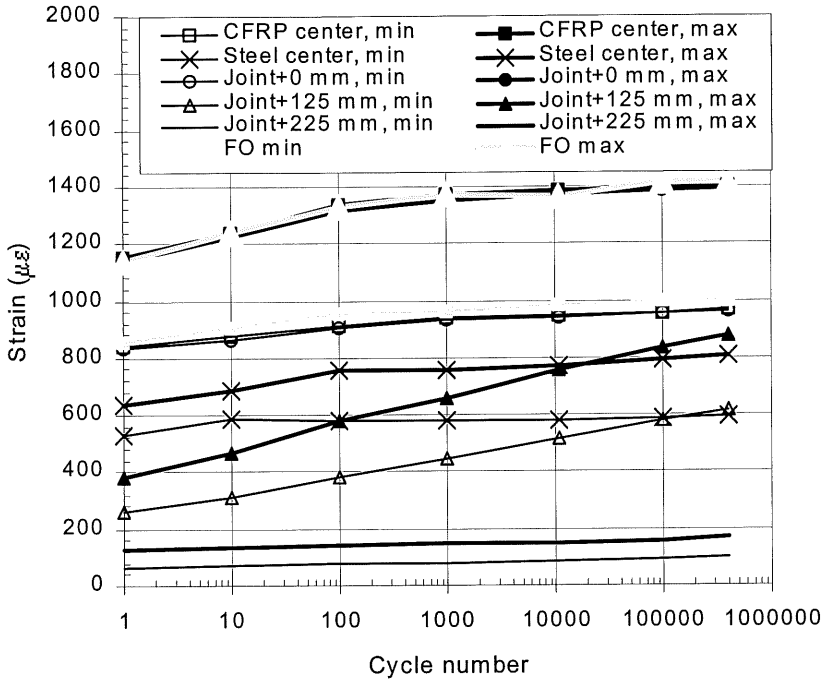

Figure D.1 Strain extremes curves for beam L400A

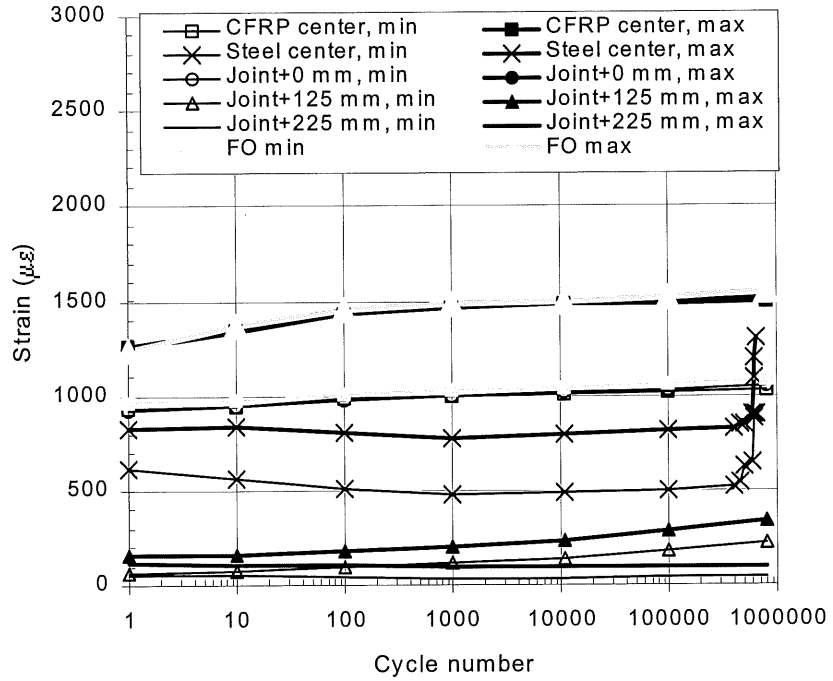

Figure D.2 Strain extreme curves for beam L800A

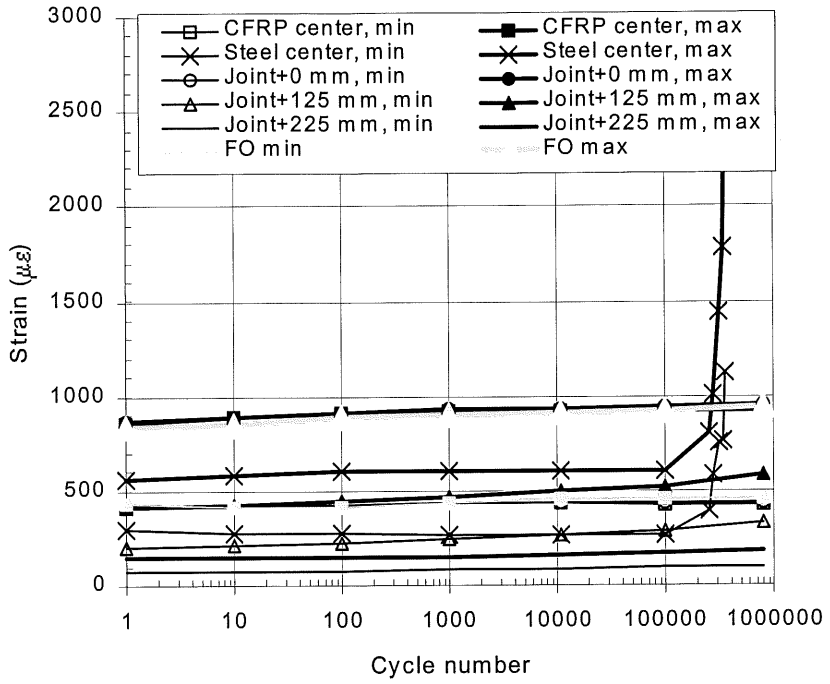

Figure D.3 Strain extreme curves for beam L800B

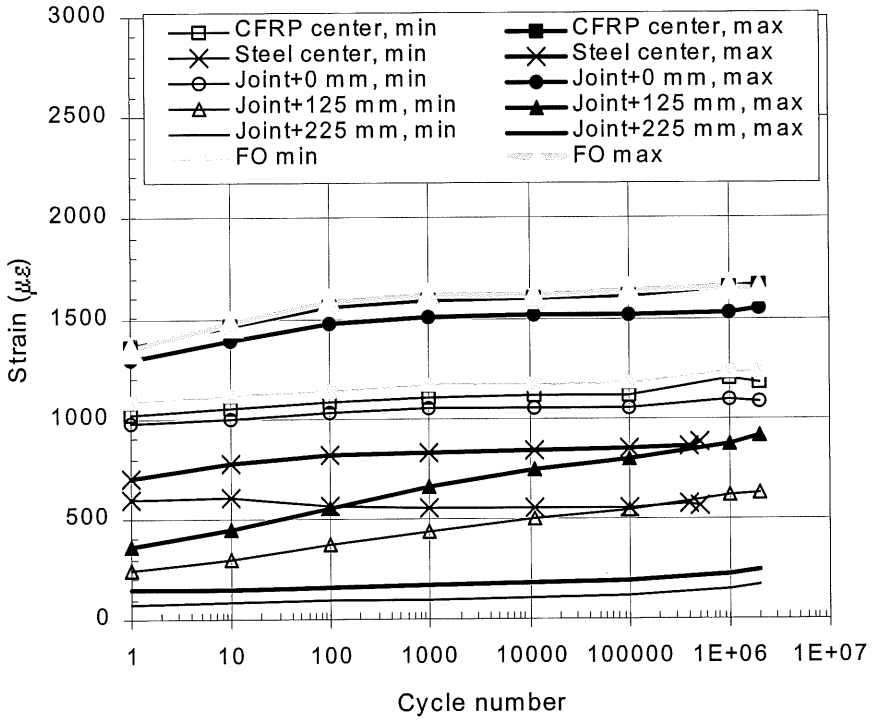

Figure D.4 Strain extreme curves for beam L2000A

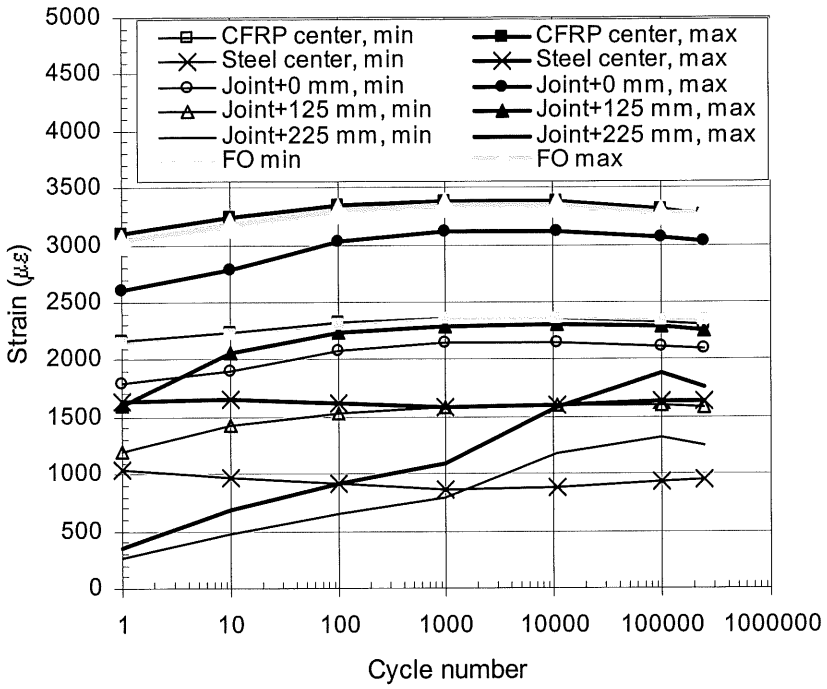

Figure D.5 Strain extreme curves for beam H400B

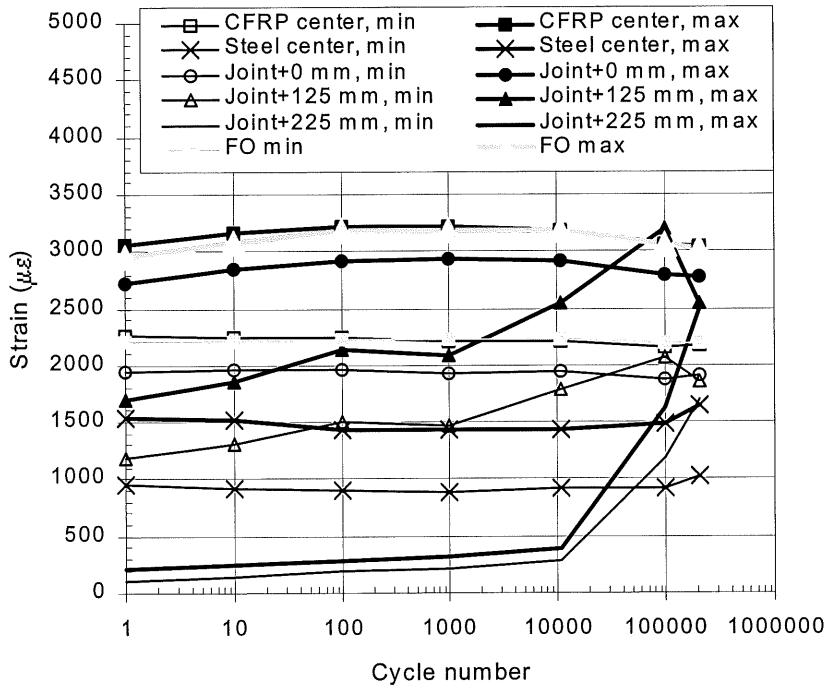

Figure D.6 Strain extreme curves for beam H800B

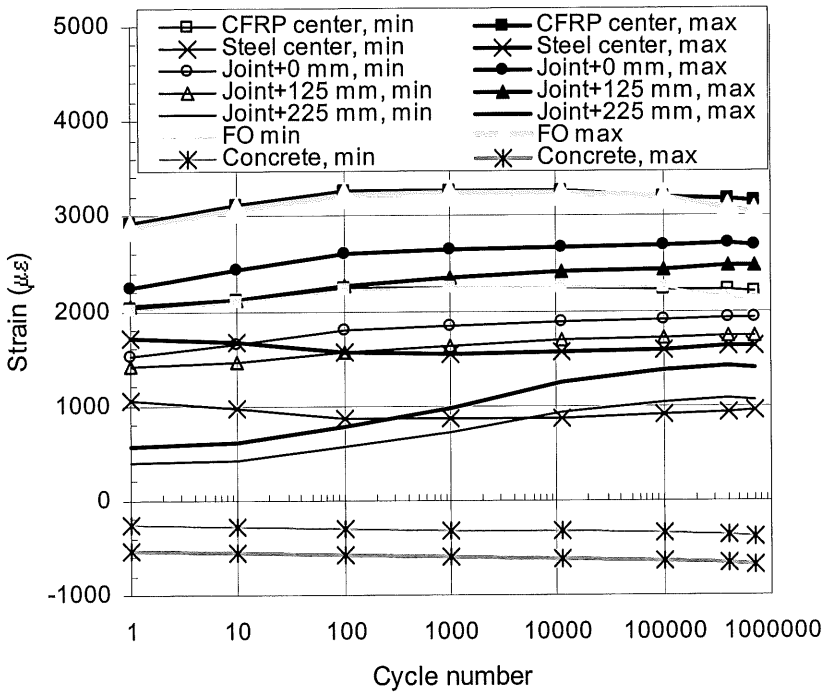

Figure D.7 Strain extreme curves for beam H2000A

APPENDIX E: INTERFACE SHEAR STRESS TRANSFER CURVES, SERIES II

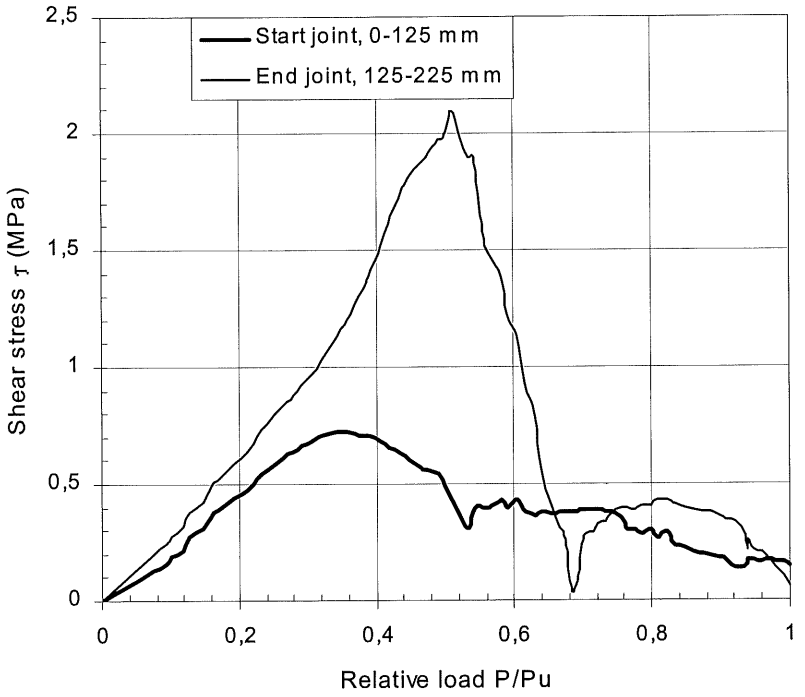

Figure E.1 Shear stress as a function of relative load for beam L400A

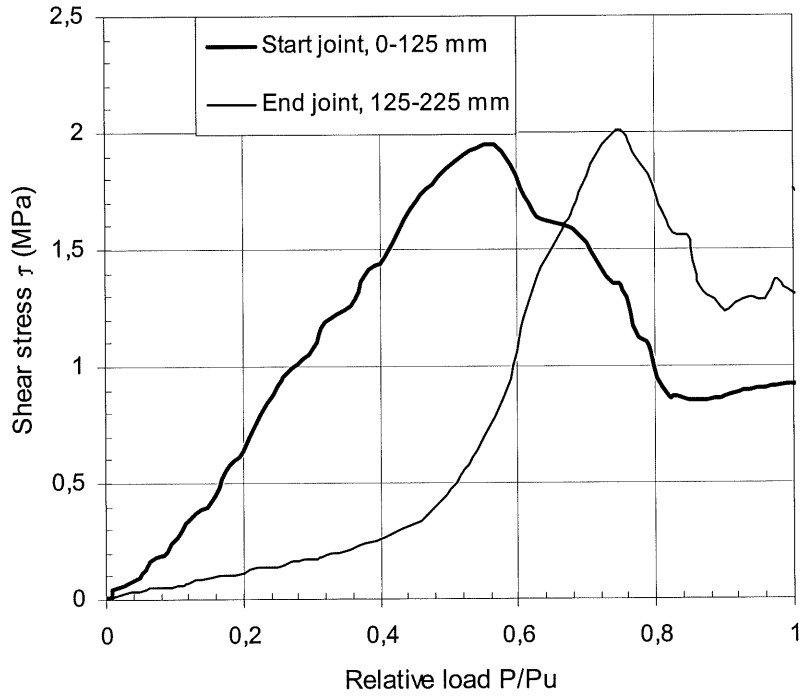

Figure E.2 Shear stress as a function of relative load for beam L800A

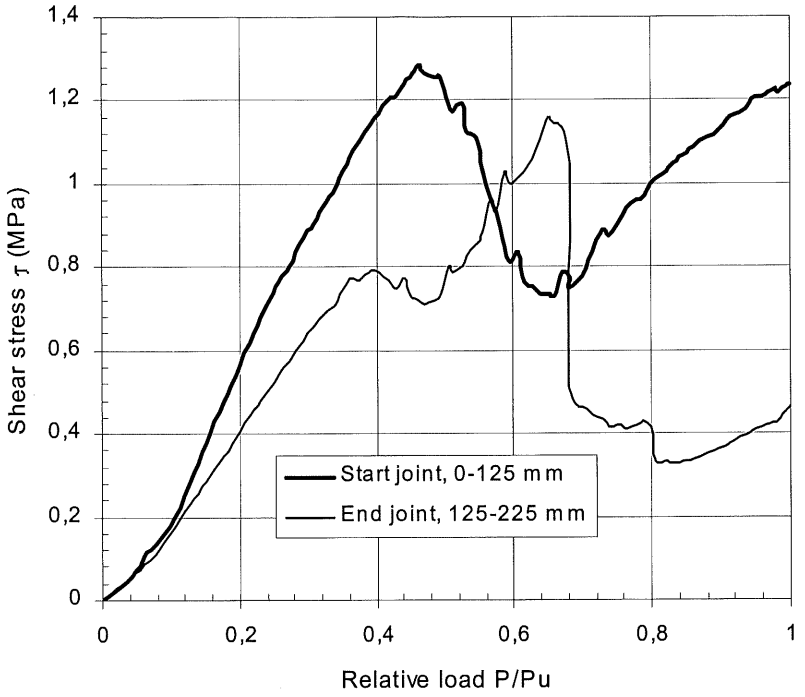

Figure E.3 Shear stress as a function of relative load for beam L800B

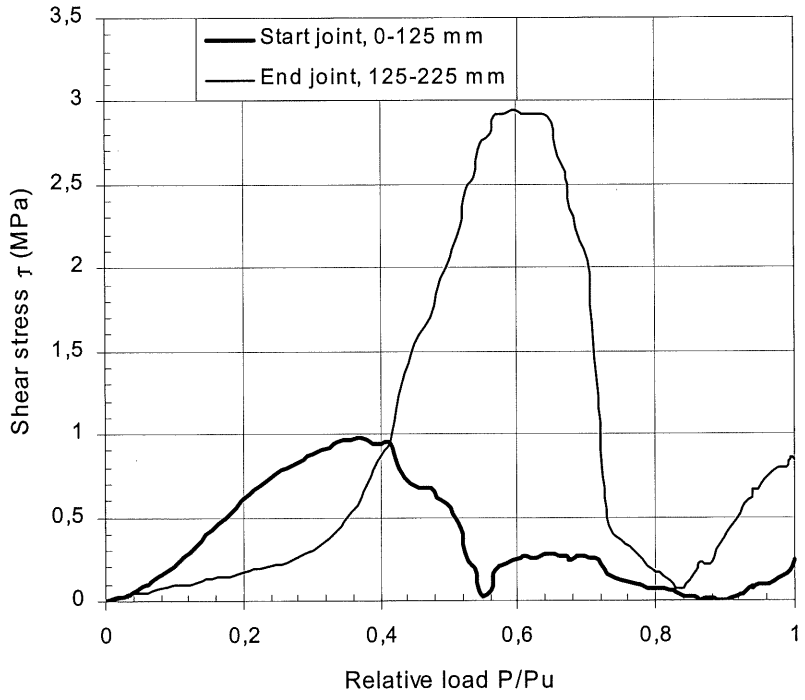

Figure E.4 Shear stress as a function of relative load for beam L2000A